Experiments on a strongly correlated material: photoresponse, phase diagram and hydrogen doping of VO_2

T. Serkan Kasırga

A dissertation
submitted in partial fulfillment of the
requirements for the degree of

Doctor of Philosophy

University of Washington
2013

Reading Committee:
David H. Cobden, Chair
Xiaodong Xu
Boris Spivak

Program Authorized to Offer Degree:
Department of Physics

University of Washington

Abstract

Experiments on a strongly correlated material: photoresponse, phase diagram and hydrogen doping of VO_2

T. Serkan Kasırga

Chair of the Supervisory Committee:
Prof. David H. Cobden
Department of Physics

The metal-insulator transition(MIT) in vanadium dioxide(VO_2) has attracted waves of attention after its first observation by Morin in 1959[1]. There are several reasons for the interest in this material. First, its metal-insulator transition is at an easily accessible temperature which allows investigators to study the effect of strong electronic correlations with little effort. Second reason is VO_2 offers many applications, although most of them are mundane, a few may have significant effects on different areas of technology. However, even after over half a century there is still a debate about the nature of the MIT and non of the applications proposed have been realized. The main culprit for this is the difficulties in studying the bulk crystals of VO_2. In bulk crystals, defects in the crystal, impurities and domain structure causes irreproducible results. This combined with the theoretical challenges made studying VO_2 and realization of applications impractical. However, recent discovery of the growth technique for growing the nano-scale crystals[2], revitalized the interest in VO_2.

In this dissertation I present the experimental studies that we performed on VO_2. I

discussed the findings from three major studies we performed; photoresponse, finding the strain-temperature phase diagram and hydrogen doping of VO_2. We used scanning photocurrent microscopy technique to reveal the light-matter interaction in VO_2. Suspended nanobeam devices* are used in the experiments and results revealed that photoresponse of VO_2 is dominated by the thermal effects and there is no photovoltaic contribution. Results are published in *Nature Nanotechnology* in 2012 [3]. In the second study, we determined the strain-temperature phase stability diagram of VO_2. This is the first ever determination of the phase diagram of a solid state phase transition. Also our studies revealed that the triple point coincides with the critical point, which has important implications for both theoretical studies of the MIT in VO_2 and for its applications. Results of this study is published in *Nature* in 2013. Last study presented here is the hydrogen doping of VO_2. There is not much known about hydrogenation of VO_2. However our initial studies revealed very high anisotropy of diffusion and mechanism other than diffusion effecting the hydrogen motion in the VO_2 crystal. There is also a chapter on previous studies and a general introduction to the MIT in VO_2. Appendices contain detailed information about the experiment setups, crystal growth techniques and device fabrication techniques. I believe studies presented here with the recent advances in the field had an important contribution to our understanding of the MIT in VO_2 and brought us closer to the realization of tantalizing applications.

*See chapter 2 and appendix B for further details.

Contents

List of Figures

Acknowledgements

"Yesterday, I was clever so I wanted to change the world. Today I am wise so I want to change myself."

— Rumi

I have arrived to the US just a little more than four years ago. It takes almost a day to get here, Seattle, from my home town. That far away from your home town, in a different culture, you need more support than you would normally need. I would like to thank my parents first since without their moral support and encouragement none of the things that I have done, including this Ph.D. would be possible. I also owe a huge thanks to my brother, without him, my life here would be much more difficult. Again, my family, thank you for your love and support.

I would like to express the deepest gratitudes to my fiancee. We could only see each other for three weeks at most, in 4-5 months since we met and I never felt far from her despite the thousands of miles between us. Her support and understanding is way beyond I could ask for. Without her I wouldn't have this much motivation to fight the challenges that life has brought to me.

I had a very relaxed and fun Ph.D. and undoubtedly this is directly related to Prof. Cobden's attitude. His eagerness to reveal the unknowns of nature tamed with his focus, provided me the motivation I needed whenever necessary. I have learned a

great deal of things from him in the past three and a half years under his supervision, not only in terms of physics but also about how to approach a problem and how to seek for answers. I feel very lucky and privileged to work with such a great scientist, and I would like to express my gratitudes to him for giving me the opportunity to work in his laboratory.

I would like to thank Prof. Xu for giving me the opportunity to collaborate with him and perform experiments in his lab. Yet, this would be an understatement of my thanks if I don't say I am really grateful for his guidance and his motivating supports. I am grateful to Jae Park for introducing me most of the equipment in the lab and I always valued his company and useful discussions we had. We have worked through many projects and collaborated. I also would like to thank Jim Coy for his amazing efforts in helping us. Without him everything would be much more difficult and time consuming.

Finally I would like to thank Chunming Huang, Zaiyao Fei, Boris Dzyubenko, Haochun Lee, Prof. Vilches and members of my advising committee Prof. Spivak and Prof. Karch. I had a very enjoyable 4 years in Seattle with the great people I met here. I would like to thank Ahmet Keles, Omer Yetemen, Onur Namli, Mustafa Gungormus, Enes Yildirim, Can Karaca, Ugur Karatay, Turgut Isik, Tunay Gur, Taha Eren, Yusuf Yigit, Onur Dagci, Emre Iliman, Anar Alimov, Ender Demirkaya and Ilker Yasin Kucuk(I almost forgot to add him, I wish it stayed that way :)). It is hard to find such sincerity in any friendship. Please accept my sincere apologies if I unintentionally forgot to mention any names here.

To my father Fahri Kasırga

my mom Aynur

my dear brother Serdar

and

tedicim Berna

Chapter 1

Introduction

"Measure what is measurable, and make measurable what is not so."

— Galileo Galilei

Many interesting phenomena like colossal magnetoresistance[4], high temperature superconductivity(HTSC), heavy fermion effects[5] and metal-insulator transition (MIT)[6] result from the strong physical interactions via spin, charge, lattice, and/or orbital degrees of freedoms(DoFs) between the electrons. The interplay between these degrees of freedoms of the d and f electrons makes strongly correlated materials extremely sensitive to small changes in external parameters such as pressure, temperature, or doping. In an ordinary material with interaction between electrons not much smaller compared to electrons' average kinetic energy, it is simpler to model the system. Since strength of the interactions between the electrons are weak, these interactions can be either ignored in the model or incorporated to model as small perturbations. For instance, classical model of metals such as Drude theory and it's quantum mechanical counterpart, Sommerfeld theory assumes that electrons flow freely inside the crystal. Free electron gas models can predict certain properties of the metals accurately but fails to capture many others such as magnetoresistance, temperature dependence of dc electrical

conductivity, cubic term in the specific heat and field strength dependence of the Hall coefficient. More advanced theories like the band structure model and associated Fermi liquid theory model can incorporate interactions between electrons with other electrons and/or lattice to predict most of the observed phenomena in a large class of materials. For strongly correlated systems, however, such models fail to provide satisfactory insight and fail to explain observed phenomena for most of the cases and even the simplest models of strongly correlated materials are difficult to solve theoretically.

Studying strongly correlated materials experimentally, turns out to be difficult as well. The difficulty arises from the fact that there are different competing orders in the materials both at microscopic(due to strong correlations) and macroscopic(classical interactions) scales. This often leads to domain structure which appear as inhomogeneities at nano-scales. Measurements on bulk samples fail to provide an understanding of intrinsic properties or behavior of the underlying homogeneous forms. Moreover, strongly correlated materials in interest are usually complicated oxides and some of them are chemically unstable, while some other are extremely sensitive to stoichiometric variations, impurities and crystal defects.

These theoretical and experimental challenges limits our understanding for most of the strongly correlated materials. The classical example is HTSC. Despite the fact that three decades past over it is discovery [7] there is only some elementary understanding about the nature of HTSC and a generally agreed microscopic model like BCS model for conventional superconductors is still missing[8]. Another common example is the metal-insulator transition in a simple binary metal-oxide, VO_2, reported by Morin in 1959[1]. While decreasing the temperature, the metallic rutile VO_2 turns to one of the insulating monoclinic phases at around 65 ℃. This phase transition is brings 4 orders of magnitude change in electrical conductivity as well as dramatic changes in thermal conductivity[9],

Seebeck coefficient[10], specific heat[11], dielectric coefficient[12] and, magnetic susceptibility[13]. After more than half a century over the first observation of the phenomena in VO_2, there is still a fierce debate on the exact nature of this solid state phase transition[14, 15, 16, 17]. There are several reasons for the lack of understanding of the true nature of the MIT in VO_2. Mechanical degradation of the bulk samples due to change in the crystal structure during the phase transition presented a serious challenge leading to sample to sample variations during the early studies of VO_2 [18]. In film samples, poly-crystalline nature of the film resulted in broadened and hysteric characteristics. These experimental difficulties combined with theoretical challenges[19] in highly polar strongly correlated VO_2 hindered our understanding of the true nature of the MIT in VO_2 and realization of the possible applications.

Exotic phenomena observed in strongly correlated materials offer many exciting applications, yet only few of these applications are realized, mainly due to difficulties mentioned above. Among the realized applications for instance, incorporation giant magnetoresistance, discovered in 1988 by Albert Fert and Peter Grnberg, has led to dramatic capacity increase in magnetic data storage technologies. Another example is high temperature superconductors.They are very important for areas like medical imaging, particle acceleration for high energy experiments and magnetically levitated vehicles. Strongly correlated materials can be employed and they have to potential to revolutionize almost any area of technology. Inclusion of degrees of freedom other than electronic charge existing in strongly correlated materials may revolutionize our information processing technologies.

Quite recently single crystal nanobeams of VO_2 become available with the introduction of the physical vapor deposition growth technique of VO_2 by Guiton *et.al.*[2]. Since these nanocrystals are smaller than the characteristic domain size and defect free, almost none of the problems in the bulk crystals and the poly-

crystalline films are present. Moreover, VO_2 is stable under ambient conditions, its metal-insulator transition is at a very convenient temperature and it offers many possible applications. Among those applications Mott field effect transistor [20], novel memory devices[21], ultrafast optical switches[22], nano-actuators[23], intelligent coatings[24], hydrogen sensors are few notable ones. These unique properties and possible applications, make VO_2 an excellent exemplary among other strongly correlated materials. In this thesis I present our studies on VO_2 nanocrystals. By studying nanocrystals, intrinsic properties of the VO_2 can be extracted from the experiments and findings from these experiments may shed light on development of new models for the MIT in VO_2 as well as may result in better understanding of similar systems.

1.1 First Order Phase Transitions

In equilibrium, a homogeneous thermodynamic system is defined by any pair of the thermodynamic quantities such as the pressure and the temperature. However, some systems may exhibit coexistence of different states at the given pair of thermodynamic quantities. These states that can coexist in contact with each other and in equilibrium are called phases of the system. Probably the most intuitive of all the thermodynamic phase transitions is the transition of H_2O, although it is not the most straightforward of them. For instance, water in a closed vessel (i.e. fixed volume) is in equilibrium with its gas phase, vapor in the air space in the vessel. In this system evaporation process, escaping of the water molecules with enough kinetic energy to break the intermolecular attraction in the liquid phase, is in equilibrium with the condensation.

For the phases to be in equilibrium, the temperatures (T_i) of the two phases and the pressures (P_i) in the two phases must be equal. From here it can be shown that chemical potentials, $\mu_1(T_1, P_1) = \mu_2(T_2, P_2)$, of the two phases in equilibrium must be equal. This is also true for phase equilibrium of more than two

phases. If we differentiate both sides of the equation with respect to temperature, Gibbs-Duhem relation will give us

$$\frac{\partial \mu_1}{\partial T} + \frac{\partial \mu_1}{\partial T}\frac{dP}{dT} = \frac{\partial \mu_2}{\partial T} + \frac{\partial \mu_2}{\partial T}\frac{dP}{dT} \tag{1.1}$$

Using the Maxwell relations and the latent heat of the transition $L = T(s_1 - s_2)$ we can show

$$\frac{dP}{dT} = \frac{L}{T(v_1 - v_2)} \tag{1.2}$$

where s_i and v_i are the specific entropy and the specific volume respectively for the phases in equilibrium. This is the Clausius-Clapeyron equation for the phase equilibrium. Using this equation phase equilibrium boundaries can be determined. This equation defines a first-order phase transition since by definition, first-order phase transitions involve a latent heat and they show an abrupt changes in physical quantities.

First order phase transitions exist in many systems in many different forms. Most common examples are eutectic transformations, order-disorder transitions, transitions between the ferromagnetic and the paramagnetic phases at the Curie temperature and changes in the crystallographic and the electronic structures as in VO_2.

1.2 Properties of VO_2

Vanadium dioxide is a binary transition metal oxide with vanadium atoms in V^{+4} valance state. In such $3d^1$ system, conventional electron-counting rules would give a half-filled outer shell resulting in a metallic ground state, which contradicts with existence of the MIT at 65 ℃. VO_2 undergoes a first order phase transition from the high temperature metallic phase to low temperature insulating phase. This electronic phase transition is accompanied by a structural one. Although there are some reports about de-linking of the electronic and the structural phase

transition [25], there is no definite demonstration. There are five known phases of VO_2 of which four of them are well known. One of them is the metallic tetragonal rutile phase, remaining three are identified to be insulating phases, where two of them are monoclinic, M1 and M2, and the remaining one is triclinic, T, phase. VO_2 displays dramatic changes during this phase transition in broad range of parameters such as thermal conductivity, dielectric coefficients, Seebeck coefficient, etc. Following subsections will provide a detailed view of all four phases.

1.2.1 The Metallic Rutile Phase

The metallic phase of VO_2 is a poor conductor with electrical conductivity along the rutile c-axis of $\sim 2 \times 10^5$ S m^{-1} * decreases slowly with increasing T [26]. The tetragonal lattice has a space group $P4_2/mnm$[27] with lattice constants $a_R \approx 4.55$ Å and $c_R \approx 2.85$ Å [28, 27]. Figure 1.1 shows the crystal structure of the metallic rutile VO_2. Metal ions in the crystal are surrounded by a octahedron with oxygen ions are at the corners of it. Looking through the c-axis channels formed by oxygen ions extend through the crystal uninterruptedly. Moreover the VO_6 octahedra share edges in the c-axis direction. The separation between vanadium ions is $c_R \approx 2.85$ Å whereas off c-axis separation is 3.52 Å[28, 27, 29]. This separation leads to anisotropy in electronic conductivity by roughly a factor of two, where conductivity is higher along the c-axis [29, 30].There has been several measurements of carrier density in the metallic phase using the Hall effect, yet almost all of the measurements are either performed on bulk[11, 31, 32] or film [33, 34, 35] samples. The problem for the bulk samples is, as reported in some references, cracking gives irreproducible results for the carrier density. The problem for the film samples, polycrystalline nature of the sputtered film may have inhomogeneous phase distribution and epitaxial films are typically under strain which

*For reference silver is 6.30×10^7 S m^{-1}

effect the carrier density. Typical carrier densities for the metallic phase along the c-axis is reported about 10^{24} and roughly 10^{23} along perpendicular to the c-axis and dominant carriers are electrons. Thermal conductivity of the metallic

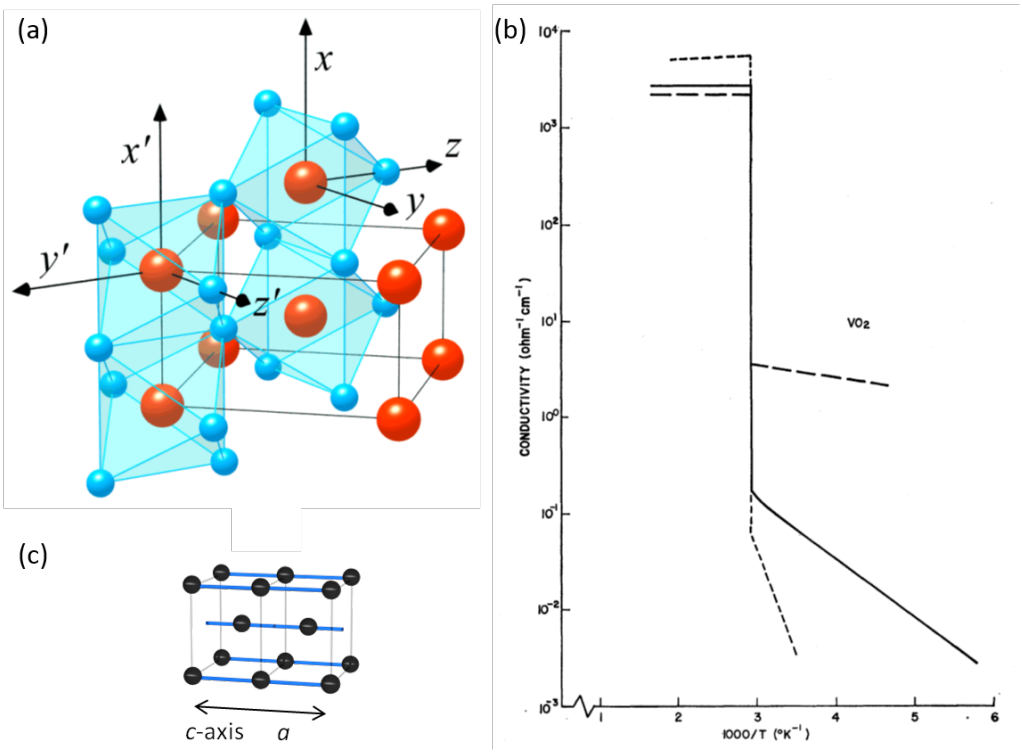

Figure 1.1: **The metallic rutile phase of VO_2.** (a) Schematic showing the unit cell of metallic VO_2 taken from Ref. [36].(b) Electrical conductivity of VO_2 from Ref. [11]. (c) Unit cell with only Vanadium atoms depicted. $a = 5.7028$[28] is twice the metallic lattice constant.

phase is found to be ~ 6 W m^{-1} K^{-1} in a recent paper[9] although Berglund et al. reports a range from 4 W m^{-1} K^{-1} to 7 W m^{-1} K^{-1} [11]. Indeed results from Oh et al. is consistent from what is expected from the Wiedemann-Franz law

$$\kappa_e = \frac{1}{3}\pi^2 \left(\frac{k_B}{e}\right)^2 \sigma T \tag{1.3}$$

where κ_e is the electronic contribution to the thermal conductivity, k_B is the Boltzmann constant, e is the electronic charge and T is the crystal temperature. However, ratio of the contributions of the lattice thermal conductivity to the elec-

tronic thermal conductivity is unknown. The Seebeck coefficient for the metallic phase is about -20μV/℃ with little temperature dependence [11].

Metallic VO_2 is paramagnetic with magnetic susceptibility of about 8×10^{-6} emu/g and there is a small anisotropy between parallel to the c-axis and perpendicular to the c-axis. This value is quite large and it cannot be attributed to conduction electrons only. The reason is extremely large extremely large density of states at the Fermi surface. However there is no evidence in the photoemission data showing such a high density of states and a narrow band near the Fermi level[11].

1.2.2 The Insulating M1 Phase

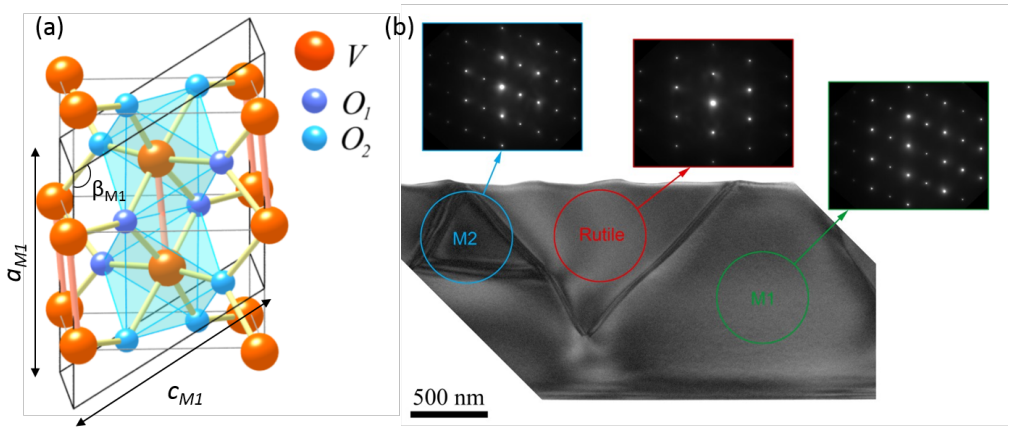

Figure 1.2: **The insulating M1 phase of VO_2.** (a) Schematic showing the unit cell of the M1 phase taken from Ref. [36].(b) TEM image and selected area electron diffraction patterns from different phases. Provided by Richard Beanland of University of Warwick.

The monoclinic M1 phase is an insulator with an optical gap of about 0.59 eV[37, 38]. Its resistivity depends on temperature T with an Arhenius type of equation, $\rho(T) = \rho_0 exp(E_a/k_B T)$, where E_a is the activation energy, k_B is the Boltzmann constant and ρ_0 is the proportionality constant. Similar to the metallic phase, anisotropy in resistivity is observed in the insulating phases but the measurements in the cited reports are insensitive to the phase insulating VO_2.

Same is also true for carrier density measurements [11, 31, 32, 33, 34, 35, 39]. A phase sensitive measurements is lacking for the Hall effect and anisotropy of the resistivity in the insulating phases. Another aspect related to the resistivity of the insulating phases is existence of constant resistivity upon heating above the transition temperature in suspended nanobeam devices[26, 40]. For M1 phase constant resistivity is reported to be $\rho_{th} = 7 \pm 2$ Ωcm. Existence of a constant resistivity implies that the transition temperature is closely linked to the metal-insulator transition temperature. The monoclinic structure has a space group $P2_1/c$ with lattice constants $a_{M1} \approx 5.75$ Å, $b_{M1} \approx 4.54$ Å, $c_{M1} \approx 5.38$ Å, and $\beta_{M1} \approx 122.65$ °[36]. Figure 1.2 shows the crystal M1 structure. Metal ions in the M1 phase are displaced with respect to their positions in the R phase in a zigzag pattern and they form pairs, while oxygen atoms stays relatively at a fixed position. M1 phase has a very small magnetic susceptibility[11] and shows van Vleck paramagnetism[14]. Thermal conductivity of M1 phase is not known accurately. For insulating phase it is found to be ~ 3 W m^{-1} K^{-1} in a recent paper[9] although Berglund et al. reports a range from 4 W m^{-1} K^{-1} to 7 W m^{-1} K^{-1} [11]. Similarly the Seebeck coefficient is not precisely known for M1 phase. Berglund et al. reports a wide range from -30 to -400 μV/℃ while Cao et al. reported about -350 μV/℃ with a slight temperature dependence[11, 10]. The M1 phase is charac-

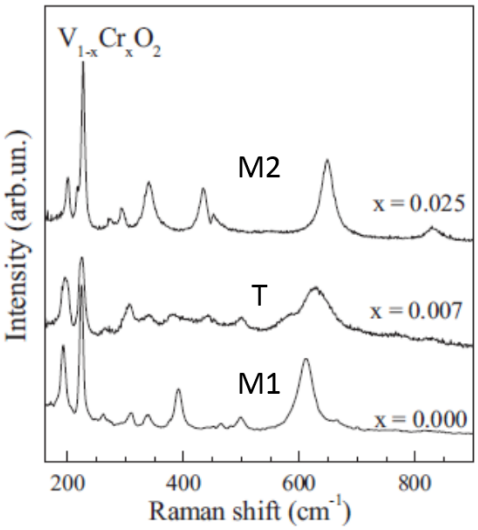

Figure 1.3: **Raman spectra of the insulating phases of VO_2** Spectra is taken from Ref. [41], where M1, M2 and T phases are stabilized by chromium doping.

terized by 18 Raman active modes with $9A_g$ and $9B_g$ [42]. Major Raman active modes that differ in other insulating phases are 610 cm^{-1} V-O, 223 cm^{-1} and 191 cm^{-1} V-V[41, 43, 42]. Figure 1.3 shows the Raman spectra in the insulating phases taken from Ref. [41].

1.2.3 The Insulating M2 Phase

The major difference between the crystal structures of the M1 phase and the M2 phase is the vanadium chain running along the center of the unit cell. In M1 phase V-V pairs both have zigzag pattern and also they are dimerized, yet for the M2 phase there is no dimerization, V-V pairs along the center are equally spaced as shown in Figure 1.4. M2 phase has a lattice space group $C2/m$[28]. Lattice constants are $a_{M2} \approx 9.07$ Å, $b_{M2} \approx 4.54$ Å, $c_{M2} \approx 4.53$ Å, and $\beta_{M2} \approx 91.88$ °[28]. Another difference between the M1 and the M2 phase is although they have the same activation energy of about 0.59 eV, resistivity ratios of M2 to M1 is $\rho_{M2}/\rho_{M1} = 2.3 \pm 0.2$ and temperature dependence is less than 5% [38]. There is no well established study on the carrier density of M2 phase. As stated before, all the measurements are either done on bulk or film samples and no report provides details for the phase that the insulating phase is in. Our photocurrent studies indicate a slight difference in the Seebeck coefficients of the two insulating phases [3]. If we assume these phases to be nondegenerate semiconductors with a electrons as the charge carrier than either the Fermi energy relative to the conduction band minimum is located at slightly different energy for M1 and M2 or electron scattering mechanisms are slightly different. Yet there is not enough information to draw a conclusive picture.

M2 phase can be stabilized by doping with dopants such as chromium[44] and aluminum[45], and by strain [43, 38, 46] along the rutile c-axis. Two monoclinic phases otherwise indistinguishable optically, can be distinguished from each other under polarized light. The difference between birefringence of M1 and M2 allows

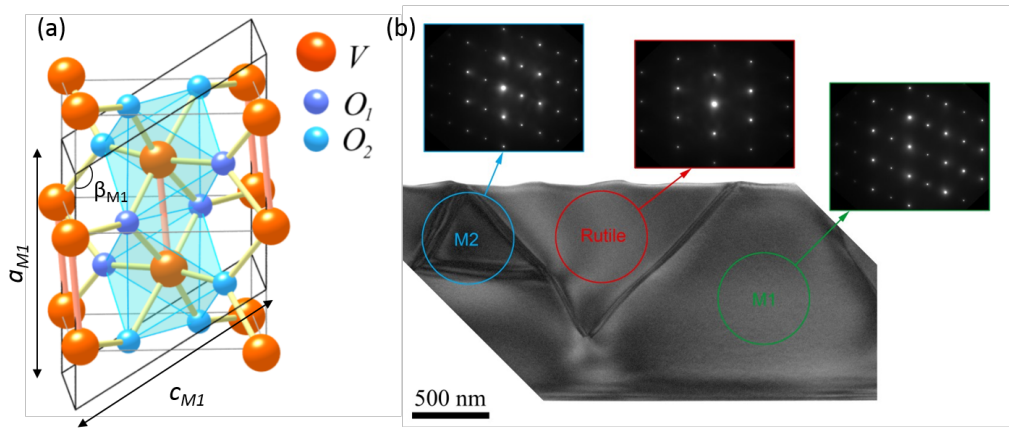

Figure 1.4: **The insulating M1 phase of VO_2.** (a) Schematic showing the unit cell of the M1 phase taken from Ref. [36].(b) TEM image and selected area electron diffraction patterns from different phases. Provided by Richard Beanland of University of Warwick.

this useful property which we benefited in our phase diagram experiments[38]. M2 phase does not rotate polarization upon reflection while M1 rotates[47, 48].

1.2.4 The Triclinic Phase

The triclinic phase of VO_2 has been reported in many different studies. In one of the earliest reports on existence of triclinic phase Kawada et al.[49] reported lattice constants of $a_T \approx 5.71$ Å, $b_T \approx 4.49$ Å, $c_T \approx 4.53$ Å, and $\alpha_T \approx 88.26$ $\beta_T \approx 122.50$, $\gamma_T \approx 90.18$ from the x-ray diffraction measurements of $VO_{2.07}$ crystals.These numbers are in close agreement in with the first report from Mitsuishi[50, 51, 52]. Detailed studies on the chromium doped VO_2 done by Pouget et al.[44] elucidate several aspects of the triclinic phase. The crystal structure of the triclinic phase is similar to that in M2 phase, where vanadium atoms are paired along the rutile c-axis but not tilted, for the inner chain they are tilted perpendicular to the rutile c-axis but not paired[28, 43]. Transitions from M1 to T is shown to be a second order phase transition, while M2 to T or T to M2 is first order determined by latent heat measurements[44], Raman spectroscopy[41, 43, 48] and electrical resistance measurements[38]. These studies also showed that there

is no R-T boundary in the phase stability diagram. Other properties of the T phase hasn't been studies in detail as it is studied for other phases. However, our studies show that resistivity of the T phase is more than the M1 phase[†]. Yet more detailed studies are required to have a better understanding of this phase.

There are claims about the existence of a monoclinic metallic phase[25] and another monoclinic phase identified phase is the M4 phase[53]. However more detailed studies are required to confirm and extend the understanding from these studies.

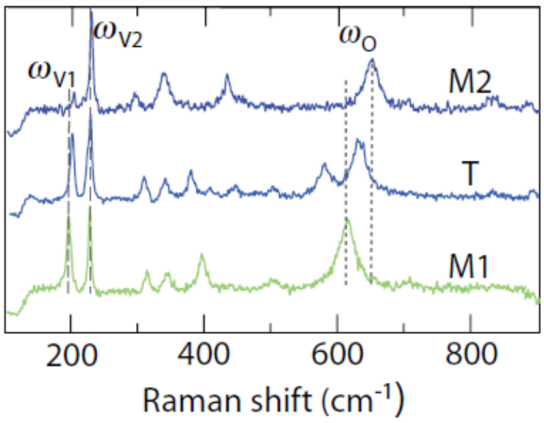

Figure 1.5: **Raman spectra of the insulating phases of VO_2** Spectra is taken from Ref. [43]. Different phases are stabilized by strain along the rutile c-axis unlike Fig. 1.3.

1.3 The Metal-Insulator Transition in VO_2

VO_2 and the metal-insulator transition is one the most commonly studied transition-metal oxide that shows MIT. During this first order phase transition, VO_2 goes from metallic rutile phase to one of the insulating monoclinic phases depending on stress, doping and temperature. Although it has been more than five decades over its first discovery by Morin, exact nature of this phase transition is not clear. Yet recent experiments indicate toward a Peierls-Mott type of transition is more probable where electron-electron correlations and dimerization of V-V pairs both play a role. There are several reasons for this. First of all, density functional theory and dynamic mean field theory(DMFT) calculations do not give the desired energy gap in the insulating phases[16] despite the fact that the molecular-orbital

[†]Please see chapter 3.

picture of Goodenough seems to provide a successful explanation to the energy gap formation in the insulating phase. Even inclusion of electron-electron and electron-phonon interactions into DMFT with local density approximation fails to predict the energy gap opening in the M2 phase [16]. These findings, especially M2 phase being insulating, suggest that a pure Peierls type of transition is not possible. Second, ultrafast spectroscopy in optical[54, 55, 56, 57], terahertz [58, 59, 60] and x-ray[61] regions has revealed that both electronic and structural changes play an important role in the phase transition. In these experiments, it has been shown that the metal-insulator transition can be induced non-thermally by shining pump beam above a critical flux depending on the sample temperature. The reason is consistent with the Mott=Hubbard picture since photoexcitation of the bonding $d_{\|}$ state of the insulator, increases the free carriers. At certain critical density of free carriers excitonic interactions due to strong correlations are screened. Third, existence of critical resistivity upon reaching the transition temperature indicates[26, 40] existence of a critical free carrier density enough to screen the electronic correlations. Last but not least, very short mean free path and electron mobility in the metallic phase also suggests strong electronic correlations in the metallic phase.

The critical temperature of the transition is at 65 ℃ which is the same as the triple temperature within 0.1 ℃[38]. Implications of this is not clear yet however a Landau phase transition theory may elucidate the underlying reason for this coincidence and predict new features about the nature of the transition.

1.4 Advantages of Studying Single Crystal VO_2 Nanobeams

There are several different methods to grow VO_2 crystals. Early studies on VO_2 used bulk crystals, often in single crystal form, and epilayers on rutile single crystals such as TiO_2 grown by solution growth, chemical vapor transport with $TeCl_4$ and epitaxial deposition epitaxial deposition from $VOCl_3$[62]. More recent growth

methods involve pulsed laser deposition[63, 64], atomic layer deposition[65, 66] and reactive sputtering[67]. These methods produce thin films of VO_2, as polycrystalline for reactive sputtering and usually epitaxial layers for other methods depending on the substrate and substrate preparation.

There are several problems associated with the bulk crystals. Twinning and domain structure combined with crystal defects result in cracking results in sample to sample variations upon cycling through the transition temperature[11, 18]. For the polycrystalline films, it is almost impossible to determine any intrinsic quantity since during the phase transition depending on the stress and purity of each crystallite there is a different phase. This means coexistence of different phases at a given temperature which smears the sharp features such as changes in conductivity[12]. In the case of the epitaxial films, depending on the lattice constant mismatch between the single crystal substrate and VO_2 there is a stress on the VO_2 film which alters the transition properties. In some cleverly designed experiments, this can be used in favor [68] but in most cases this control is limited and the effects of the strain on the phase transition is dramatic.

Nanocrystals of VO_2 grown on SiO_2 is superior to other types of crystals in many aspects. First of all, nanocrystals are very straightforward to grow[2]. Second, they are smaller than the typical domain sizes, pure and defect free. This allows a reproducible investigation of the phenomena observed in VO_2. Third, crystals thermodynamically favor growing along the rutile c-axis where most dramatic changes during the MIT happens along this axis. Fourth, unlike film samples, these crystals can be easily transferred on to other substrates or can be manipulated to make novel devices[38]. Finally, nanocrystals are more suitable for optical studies[3].

Chapter 2

Scanning Photocurrent Studies on VO_2

"If the result confirms the hypothesis, then you've made a measurement. If the result is contrary to the hypothesis, then you've made a discovery."

— Enrico Fermi

In this chapter results from the scanning photocurrent measurements(SPCM) on VO_2 nanobeams are presented. SPCM measurements on suspended nanobeam devices* has revealed that photoresponse of VO_2 above and below the MIT is governed by photothermal currents and conductivity changes. Consistent with the strong correlations, this photothermal response implies that carrier relaxation to a local equilibrium is fast. Temperature dependent measurements reveal subtle phase changes within the insulating state elucidating the changes in the configuration of the different insulating phases, I_{M1} and I_{M2}. We further demonstrate switching of the photocurrent by optical control of the metal-insulator boundary arrangement. These results are important for realization of the optoelectronic

*see Appendix B for detailed description and fabrication steps of devices used in this chapter.

applications using the peculiar properties of VO_2 as well as development of the correct theory of the MIT in VO_2. Results of the studies presented in this chapter are published in Nature Nanotechnology [3].

2.1 Introduction

2.1.1 Scanning Photocurrent Microscopy

Studying the local excitations in a semiconducting systems provides a route for probing the internal electric fields emerging from band offsets, surface states, defects, contacts or thermal gradients. Understanding and mastering the physics of free charge carriers under such intentional or unintentional fields had significant effect in the development of current semiconductor technology. Same approach will also have impact on transfer of novel material systems to practical applications[69, 70]. Spatially resolved detection of the electric current under a local perturbation is one way of observing the effects of the internal fields. Applying a local gate[71, 72, 73, 74, 75, 76, 77, 78] or exciting non-equilibrium carriers by focused light or electron beam[79, 80] are among the techniques that have been developed for studying the carrier dynamics in semiconducting systems. For instance, in scanning photocurrent microscopy(SPCM) by scanning a focused laser beam on a target sample, the current generated is detected as a function of the laser position via electrical contacts to the sample and mapped out[81]. A great variety of semiconducting structures and devices have been studied employing this technique[39, 82, 83, 84, 85, 86, 87, 88, 89, 90, 91, 92, 93]. The photoresponse of semiconducting systems in which electron-electron and/or electron-phonon correlations are negligible, it is clear that the photoresponse will be composed by the drift and diffusion of the non-equilibrium carriers created by the laser beam as well as a contribution from the photothermal effects due to heating caused by the laser beam. Total electric current generated can be described through the

local electric current density, which is given by

$$\mathbf{j} = \sigma\mathbf{E} - eD\boldsymbol{\nabla}n(x) + \sigma S\boldsymbol{\nabla}T(x) \tag{2.1}$$

where the first term is the Ohm's law for a material with conductivity of σ under the electric field $\mathbf{E}$, the second term is the diffusion of the carriers with e denoting the charge of the charge carriers, D being the diffusion coefficient for the given carrier type and $n(x)$ being the charge carrier density. The third term is the current due to emf generated by the thermopower with S being the Seebeck coefficient and $T(x)$ is the temperature distribution on the material. For most semiconducting systems, however, photovolatic effects dominate the photoresponse thus, the dominant terms are the first two terms in equation 2.1. Nature of the photoresponse is determined by the relaxation pathways of the photoexcited charge carriers. Typical lifetimes of the nonequilibrium charge carriers in an undoped indirect band gap semiconductor is on the order of milliseconds, thus nonequilibrium carriers can be collected under a source-drain bias while some of the energy is lost as heat. Modifying the relaxation pathways via electron-electron and electron-phonon correlations lead to novel photocurrent generation mechanisms. For instance, in graphene hot-carriers dominate the photoresponse since electron-electron scattering and optical phonon emission slows down the electron-lattice relaxation speed[92, 94]. Thus, thermal equilibrium between the lattice and electrons is not reached over length scales of several microns[95]. Similarly, due to impact excitation in single walled carbon nanotubes, multiple carriers are generated with extreme efficiency [89]. It is not clear what physics dominates the photoresponse of systems with strong electron-electron and electron-phonon correlations . As outlined in the first chapter of this thesis, materials with such strong correlations offer great variety of applications and rich physics. Again, as advertised in the first chapter, VO_2, which is known as the drosophila of the strongly correlated materials, offers applications in optoelectronic detection and ultrafast

switching up to ultraviolet wavelengths[21, 22, 56, 57, 96, 97]. Henceforth, studying the physics of photoresponse in VO_2 is important both for understanding the mechanisms of photocurrent generation in similar strongly correlated materials and their application in optoelectronic devices.

2.1.2 Experimental Setup

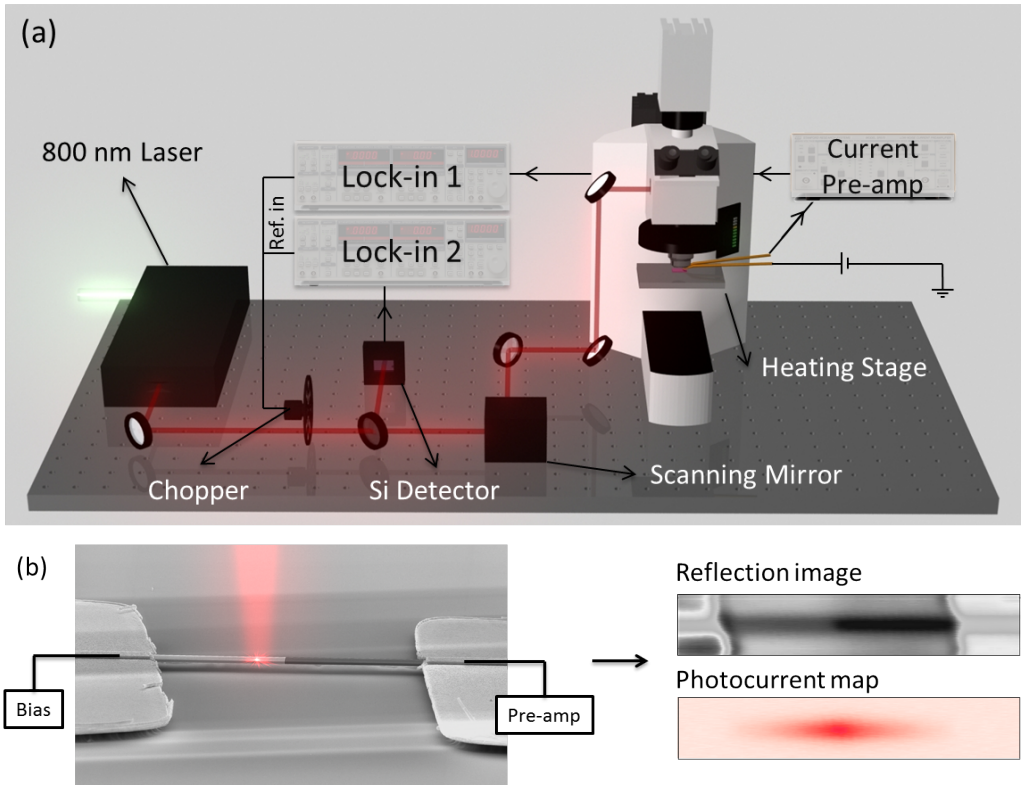

Figure 2.1: **Scanning photocurrent experiment setup.**(a) Laser beam at 800 nm is chopped and directed by scanning mirrors to the microscope and focused by an 40x long working distance objective.(b) Laser beam imposed on an SEM image showing the raster scan on a wire at coexistence. As mentioned in the text bias is connected to the left and the current pre-amp is connected to the right contact. Reflection image and corresponding photocurrent map is generated as described in the text.

The scanning photocurrent setup we use for this study is a home-made setup with ultra-fast pump-probe measurement and Raman spectroscopy capabilities. An ultrafast Ti:Sapphire laser (Coherent Mira 900) pumped by an 18 watt frequency

doubled green laser at 532 nm (Coherent Verdi V18) is used to get continuous wave or 250 fs pulsed wave at 800 nm. As shown in Figure 2.1(a) the laser beam chopped at 1 kHz is directed to the microscope (modified Olympus BW51) and focused onto the sample with a diffraction limited spot size. The sample is placed on an small invar temperature stage, with a DT670 silicon diode temperature sensor from Lakeshore embedded, to minimize the effects of thermal expansion. The temperature of the stage is controlled by a Lakeshore 340 controller. The current generated is collected by a DL instruments 1211 current preamplifier which is connected to an Stanford Research SR830 digital lock-in amplifier referenced by the chopper. The reflected light is collected by a Si photodiode which is also connected to another lock-in amplifier. Outputs of the lock-in amplifiers are recorded by a Labview program generates a synchronous map of the photocurrent and the reflected light. Same program controls the scanning mirrors. Throughout this chapter, for the sake of clarity and consistency we will stick with the conventions that the bias is applied from the left contact and the current pre-amp is connected to the opposite contact as shown in Figure 2.1(b)

Raman spectroscopy is performed using the 532 nm output of the pump laser directed to same beam path as the 800 nm beam. The reflected light is passed through a notch filter at the excitation beam wavelength collected by a monochromator (Princeton Research Acton) and recorded by a liquid nitrogen cooled CCD array. Whole setup rests on an optical table. The laser intensity is controlled by nd filters and power measurements are taken by a calibrated portable Si detector from Thorlabs.

2.2 Experiments

2.2.1 SPCM on Nanobeams in M1 Phase

We first start with performing experiments on the nanobeams at room temperature or slightly above the room temperature. Depending on the gap length between the contacts and the growth conditions of the nanobeams, nanobeams could be in either M1 phase and unbuckled or in M2 phase and buckled or some mixture of both M1 and M2 phases. For this part of the study we choose nanobeams that are completely in insulating M1 phase determined by Raman and resistance vs. temperature measurements.

Under no source-drain[†] bias V_{SD}, the photocurrent, I_{ph}, is negligibly small, less then few picoamperes with positive sign on pre-amp side and negative sign at the ground side (Figure 2.2(a)). When V_{SD} is not zero, there is a photocurrent generation along the entire nanobeam, increasing toward the middle of the beam. This change in the photocurrent can be described entirely in terms of a bias independent photoconductance. Figure 2.2(b) shows the photocurrent along the center of the nanobeam in the upper panel, and the photoconductance derived from that, $G_{ph} = (I_{ph} - I_0)/V_{DC}$, in the lower panel.

As it is shown clearly in the following section, laser heating plays a significant role in these measurements even with very small ($\sim$ 0.3 µW) laser powers and these measurements can be explained by the heating caused by the laser beam. The circles in Figure 2.2(b) lower panel denotes the calculated photoconductance emerging from a thermal resistance change. In the calculations we define x to be the fractional position along the suspended part of the nanobeam, running from 0 at the left contact to 1 at the right contact, which is 15 to 20 µm length depending on device. As it is depicted in Figure 2.3 the laser is focused at position x_l. The temperature at point x is $T(x) = T_0 + \delta T(x)$ where T_0 is the stage

[†] Here, unlike semiconductor industry, source designates the contact current applied and drain is the contact for measurement.

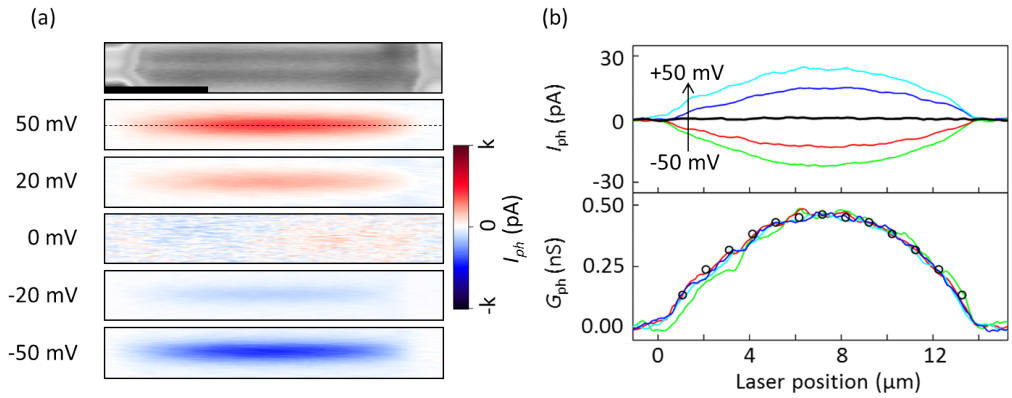

Figure 2.2: **SPCM at 30 °C.**(a) Reflection image of a suspended nanobeam is shown in gray scale with the scale bar representing 5 µm. Below the reflection image, corresponding photocurrent maps under different V_{SD} biases are presented. Except for the 0 mV bias, k denoting the range of the color scale is 30 and for 0 mV bias it is 5. (b) Upper panel shows photocurrent along the center of the nanobeam, shown by a dashed line in (a), under different biases. The lower panel shows the photoconductance measured (solid lines) and calculated (circles).

temperature. The measured change in conductance when the laser is applied $\Delta G = \Delta(\frac{1}{R}) = \frac{1}{R_{laseron}} - \frac{1}{R_{laseroff}}$, where R is the resistance of the nanobeam. For small temperature rise $\delta T(x)$

$$\Delta G = \Delta(\frac{1}{R}) \approx -\frac{1}{R^2}\Delta R \approx \frac{1}{R^2}\frac{L}{A}\int_0^1 \frac{d\rho}{dT}\delta T(x)dx = -\frac{1}{R^2}\frac{dR}{dT}\delta T_{av} \tag{2.2}$$

Here L is the length of the suspended part of the nanobeam, A is the cross-sectional area of the nanobeam, $\rho(T)$ is the resistivity of the nanobeam. Thus the negative temperature coefficient of $\rho(T)$ leads to a positive ΔG proportional to the average temperature rise $\delta T_{av} = \int_0^1 \delta T(x)dx$ along the nanobeam, with dependence of the laser position that follows this quantity, $\Delta G(x_l) \propto \delta T_{av}(x_l)$. To calculate $\delta T_{av}(x_l)$ we first assume that all the heat flows along the nanobeam since for these studies typically shorter nanobeams are used. Then $\delta T(x)$ simply drops linearly from a maximum value of $\delta T_l = \delta T(x_l)$ at the laser spot to zero at each of the gold contacts and as a result $\delta T_{av} = \delta T_l/2$. By symmetry $\delta T_l/2$ is maximum when $x_l = 0.5$, and making the heat current to left and right sum

to a constant (the absorbed laser power) gives $\delta T_l \propto x_l(1-x_l)$. Thus $\Delta G(x_l) \propto \delta T_{av}(x_l) \propto \delta T_l \propto x_l(1-x_l)$. This variation fits the measurements of G_{ph} vs x_l very well as seen in Figure 2.2(b).

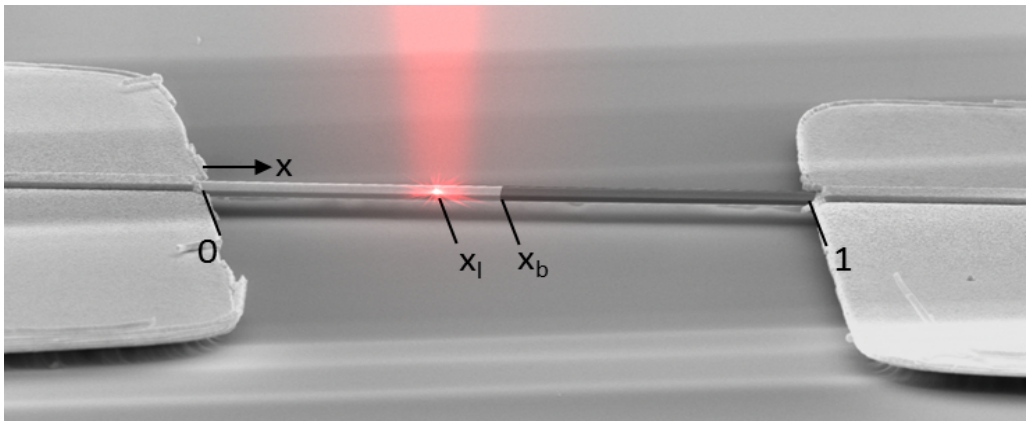

Figure 2.3: **SEM image with definitions.** The nanobeam has been colored dark on the right to indicate a metallic domain, though in reality there is no I-M contrast in the electron microscope.

2.2.2 SPCM on Nanobeams in Coexistence of Metallic and Insulating Phases

In order to quantify the rise in the temperature we exploited the coexistence of the two phases above T_c. The fraction x_b of insulator (I_{M2}) in the nanobeam depends on the lattice temperature T_b at the boundary, since x_b determines the axial tension, which must be appropriate for the two phases to coexist at T_b. x_b decreases with the increasing stage temperature T_0, as shown by the red circles in Figure 2.4 . It also decreases with increasing laser power P at fixed T_0, as shown by black circles. By comparing the effects of increasing P and T_0, we deduce that for device 1 the local temperature rise of the lattice with the laser near the middle is $\sim$ 1.5 ℃ per µW of laser power. Consistent with the laser heating as P increases interface boundary has a curved appearance in the reflection image shown in figure 2.4(b). This is due to as the laser beam passes through the middle of the nanobeam, heat absorbed becomes the largest. As the laser beam moves

to the sides of the nanobeam absorbed heat decreases leading to less temperature rise at x_b.

Next we looked at the photocurrent generated in coexistence of metallic and

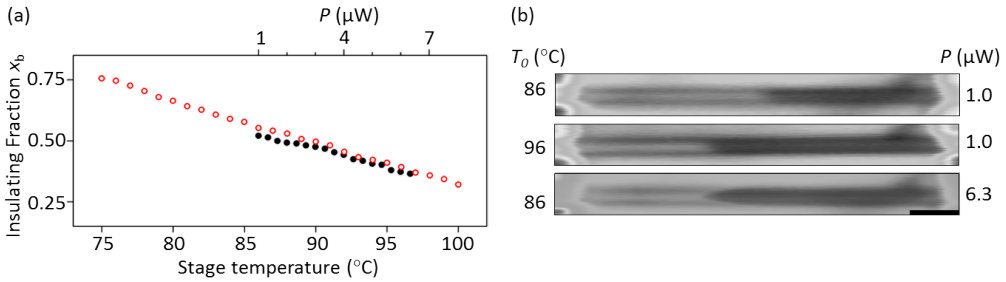

Figure 2.4: **Evidence for laser heating** (a) Insulating fraction versus stage temperature (red circles) and laser power (black circles) is given. Comparing the two gives a local temperature rise of the lattice with the laser near the middle is ~ 1.5 ℃ per μW of laser power for the device presented here. (b) Reflection images showing the effect of laser beam on the interphase boundary.

insulating phases above the transition temperature. In contrast to SPCM at low temperatures, this time we observe a relatively strong photoresponse when $V_{SD} = 0$. Also for $V_{SD} \neq 0$ we observe changes in the photoresponse. Figure 2.5 shows reflection image, photoresponse and photoconductance G_{ph} of a device at 75 and 90 ℃.

Both at 75 and 90 ℃, zero-bias photocurrent is peaked at the metal-insulator interface as shown by reflection images in panel ii of Fig. 2.5 (a) and (b). This is also evident in line trace along the uniaxial direction of the nanobeam shown in panel iii. As we apply bias, V_{SD} we observe a slightly different photoresponse for 75 and 90 ℃. Yet, as in the below T_c case we see that G_{ph} is same for different V_{SD}, for both temperatures. This can again be understood as the result of the temperature rise of the lattice with no hint of other contribution. The decrease in the insulating fraction x_b, which is determined by the boundary temperature since the axial stress needs to be appropriate for two phases to coexist, with boundary temperature rise $\delta T_b \equiv T_b - T_0$ results in a conductance increase that is largest when δT_b is maximum. In 95 ℃, it is when $x_l = x_b$. The more com-

plicated photoresponse at 75 ℃ is a result of change in resistivity $\rho(T)$ of the insulating part which is comparable to the effect interface movement. However, it is difficult to model accurately.

These observations are consistent with photothermal effects. Moreover, since we

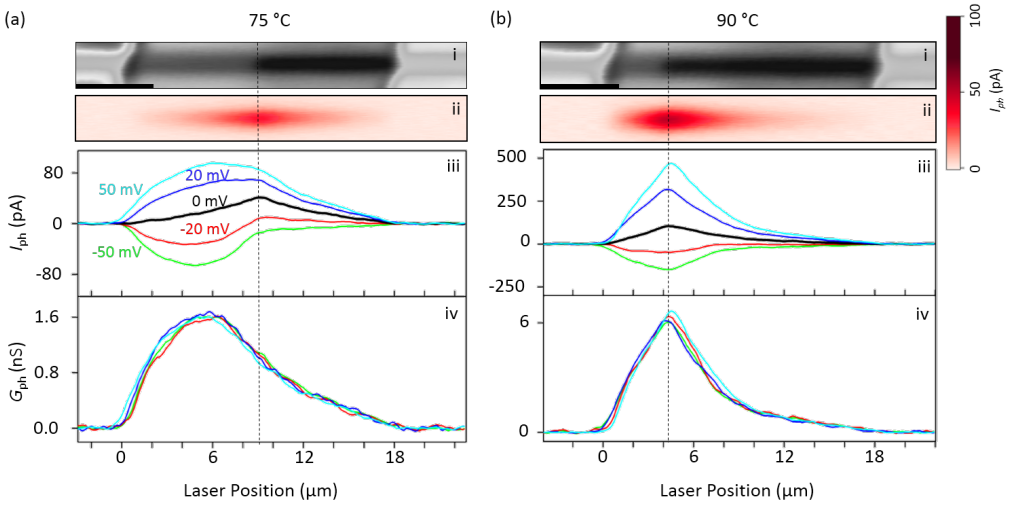

Figure 2.5: **Photoresponse above T_C** Panel i show reflection image, ii is the zero bias photocurrent map, iii line traces along the uniaxial direction of the nanobeam and iv shows photoconductance, G_{ph} for both (a) and (b). (a) Photoresponse at 75 ℃. Complicated behavior of the photoconductance can be explained by the change in resistivity $\rho(T)$(See the main text). (b) Photoresponse at 95 ℃. This time photoconductance is peaked at the phase boundary with a small hint of a hump on the insulating side as opposed to 75 ℃. This can be understood from the fact that as the laser gets close to the gold contacts δT_l decreases.

don't observe any nonequilibrium carrier response for time scales greater than our setup's minimum pulse width of 250 fs in the pump-probe experiments (data not presented here) and photoresponse has no laser wavelength dependence, consistent with a photothermal mechanism in which only the absorbed laser power is relevant (Fig. 2.6(b)), we can start our analysis with assuming that the carrier relaxation to complete equilibrium with the lattice is fast. The lattice temperature difference δT_b between the I-M boundary and the gold contacts will generate a thermoelectric electromotive force (emf) ,$V_{th} = -\Delta S_{IM} \delta T_b$, due to difference in

Seebeck coefficients of I_{M2} and M phases. From the literature [11, 10] $S_I \approx -350$ µV ℃$^{-1}$(for I_{M2}) and $S_M \approx -20$ µV ℃$^{-1}$, so $\Delta S_{IM} = -330$ µV ℃$^{-1}$. Result of this emf is expected to be $V_{th} \approx 500$ µV for a 1 µW laser focused near the middle since as found for the device studied above it gives $\delta T_b \approx 1.5$ ℃. Figure 2.6 (a) shows I_0 as a function of temperature and the corresponding emf, $V_0 = I_0 R$. V_0 reaches up to about 450 µV, in excellent agreement with V_{th} considering the uncertainty in the knowledge of the Seebeck coefficients of different phases. We can calculate the variation of V_0 as a function of stage temperature as well as variation of V_{th} with laser position, allowing for different thermal conductivities κ_M and $\kappa_{I_{M2}}$ of the two phases and for heat loss $\beta\delta T$ through the air.

As before, shown in Fig. 2.3, we define x to be the fractional position along the nanobeam ranging from 0 at the left contact and 1 at the right contact. Insulating phase is positioned to be on the left and position of the boundary, x_b, is equal to the length of the insulating phase. For the sake of simplicity we are going to assume that x_b is not effected by the laser since laser power P is small (indeed, effects on x_b will be quadratic in P). The laser is focused at the position x_l. Here, our aim is to find an analytic expression between δT_b and x_l so that we can get the line shape of I_0 as a function of x_l using $V_{th} = -\Delta S_{IM} \delta T_b$. Again as in the fully M1 case, we assume $\delta T(0) = \delta T(1) = 0$ at the gold contacts and $\delta T_l \equiv \delta_T(x_l)$ is due to absorbed power γP with γ being a constant. δT will satisfy a one-dimensional steady state heat equation with a Newtonian cooling factor $\beta\delta T(x)$ (heat loss per unit length to substrate through the air by conduction), of the form

$$\frac{\kappa A}{L^2} \frac{d^2 \delta T(x)}{dx^2} - \beta \delta T(x) = 0 \tag{2.3}$$

or, by rearranging all the constants in to a single constant

$$\frac{d^2 \delta T(x)}{dx^2} - \alpha^2 \delta T(x) = 0 \tag{2.4}$$

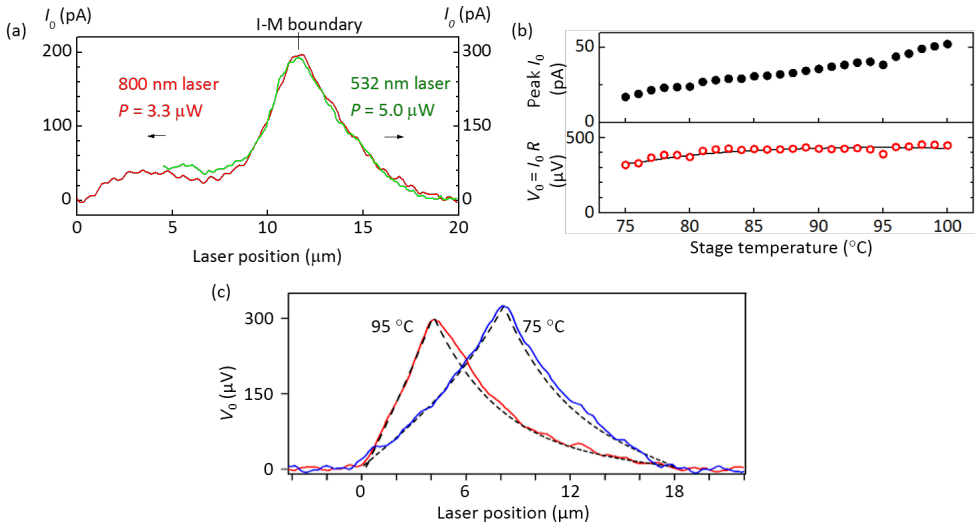

Figure 2.6: **Understanding the photoresponse above T_C** (a) In our measurements different laser wavelengths result in very similar results. Here, wavelength dependence of I_0 to 800 nm and 532 nm excitation is shown. Different powers were used for the two lasers and both lasers essentially have the same photocurrent profile along the nanobeam when scaled by the power difference. This implies similar absorption coefficient at both wavelengths. The bump in the insulating phase is due to relatively high laser powers used in here. (b) Upper panel shows the amplitude of the photocurrent, I_0 at the phase boundary as a function of stage temperature T_0. In the lower panel, red circles show the derived value of emf, V_0 from I_0 and dark resistance measurements as a function of stage temperature. Solid line shows the calculated value for the emf.(c) Red and blue lines show the profile of V_0 along the uniaxial direction the nanobeam as a function of the laser position. The emf is peaked at the phase boundary for both 75 and 95 ℃. Dashed lines are the expected emf from the analytical model. The excellent agreement of measurements to the expected values indicates the photothermal contribution of the photoresponse is the most dominant contribution.

where $\alpha = \sqrt{\beta L^2/\kappa A}$ and κ is the c-axis thermal conductivity which differes for insulating and metallic phases, where $\kappa = \kappa_{I_{M2}}$ for $x < x_b$ and $\kappa = \kappa_M$ otherwise. We take γ to be the same for both phases since it creates and step in the photoresponse which we don't observe in our measurements, possibly due to the finite size of the laser spot such sharp features are smeared.

Equation 2.4 can be solved in there regions piecewise, region I $(0, x_l)$, region II (x_l, x_b) and region III $(x_b, 1)$. Using the general solution with appropriate choice

of constants α_I or α_M and boundary conditions we get

$$\delta T(x)) = \begin{cases} \frac{\delta T_l \sinh \alpha_I x}{\sinh \alpha_I x_l} & 0 \leq x \leq x_l \\ \frac{1}{\sinh \alpha_I (x_l - x_b)} [\delta T_l \sinh \alpha_I (x - x_b) - \delta T_b \sinh \alpha_I (x - x_l)] & x_l \leq x \leq x_b \\ \frac{\delta T_b \sinh \alpha_M (1-x)}{\sinh \alpha_M (1-x_b)} & x_b \leq x \leq 1 \end{cases}$$

To find the values of δT_l and δT_b we apply the boundary conditions between regions I, II and III corresponding to conserving energy flow at $x = x_l$. So, we get

$$\frac{\kappa_I A}{L} \left(\left. \frac{dT}{dx} \right|_{x_l, I} - \left. \frac{dT}{dx} \right|_{x_l, II} \right) = \gamma P \tag{2.5}$$

and at $x = x_b$ we get

$$\kappa_I \left. \frac{dT}{dx} \right|_{x_l, I} - \kappa_M \left. \frac{dT}{dx} \right|_{x_l, II} = 0 \tag{2.6}$$

After making use of the expression above and eliminating δT_l we obtain the required expression to calculate the boundary temperature as a function of laser position

$$\delta T_b(x_l) = \frac{\delta T_l(x_l)}{C_1} = T_P \frac{\sinh \alpha_I (x_b - x_l)}{C_1 C_2 - 1} \tag{2.7}$$

where $T_P = \gamma P / \sqrt{\kappa_I \beta A}$, $C_1 = \cosh \alpha_I (x_b - x_l) + \sqrt{\kappa_M / \kappa_I} \coth \alpha_M (1 - x_b) \sinh \alpha_I (x_b - x_l)$ and $C_2 = \cosh \alpha_I (x_b - x_l) + \coth \alpha_I x_l \sinh \alpha_I (x_b - x_l)$.

For the case where $x_l > x_b$ we obtain similar equations where x is replaced by $1 - x$, x_b by $1 - x_b$ x_l by $1 - x_l$ and, κ_I and κ_M are interchanged. Finally, using equation 2.7 at $x_l = x_b$ in the expression $V_{th} = -\Delta S_{IM} \delta T_b$, we can find the dependence of V_0 to the stage temperature. $x_b(T_0)$ is determined from the reflection images at each temperature presented in figure 2.6 (b). Solid line on

the lower panel is a plot of function

$$V_0 = V_P \frac{1}{\coth \alpha I x_b(T_0) + \sqrt{\kappa_M/\kappa_I} \coth \alpha_M (1 - x_b(T_0))} \tag{2.8}$$

where $V_P = -\Delta S_{IM} \gamma P / \sqrt{\kappa_I \beta A}$, with values of the parameters $L = 18$ µm, $A = 0.2$ µm^{-1}, $\Delta S_{IM} = -330$ µV ℃$^{-1}$, $\kappa_I = 3.5$ W/m/℃[9] and $\kappa_M/\kappa_I = 2$. We treat T_P and β as fitting parameters. The best fit is obtained for $\beta \approx 0.03$ W/m℃and $T_P \approx 2.8$ ℃. From these we get $\alpha_I = 3.7$ and $\alpha_M = 2.6$. For this device $\gamma = 0.6$ and β is consistent with thermal conduction through the air($\kappa_{air} \approx 0.03$ W/m℃ at 80 ℃) between the bottom of the nanobeam which is of width ~ 1 µm and the substrate distance ~ 1 µm beneath it.

For V_{th} as a function of the laser position we, again, use equation 2.7 in $V_{th} = -\Delta S_{IM} \delta T_b$. For this device we used same parameters as above to get the best fit to the experiment data except $\gamma \approx 0.5$. This difference between the absorption coefficients of two devices could be as a result of differences in the cross-sections of the two nanobeams. Dashed lines in figure 2.6 (c) shows the excellent fit of calculations to the experiment data depicted by solid lines at two different temperatures, 75 and 95 ℃.

2.2.3 Investigation of Additional Contributions to the Photoresponse

In the previous sections we have established that the predominant contribution to photocurrent is photothermal and have given the hints of fact that it is indeed purely photothermal. Although we employ very small laser powers, there is no dependence to the excitation wavelength and we see no evidence of separation of the non-equilibrium carriers from the ultra-fast pump-probe experiments, we further investigate this possibility as it might be expected in a band semiconductor like silicon[98, 99]. Such contribution is not possible for excitation in the metallic phase, because electron-lattice relaxation occurs in picoseconds in all metals since there is no gap to block the low-energy recombination process. Thus

photocurrent signal extending many micrometers into the metallic region must be entirely photothermal. Moreover, the fact that there is no difference between the observed photocurrent for pulsed (250 fs repeated at 76 MHz) and continuous wave excitation at the same average power is consistent with only relevant quantity is the absorbed power. It has to be also noted that there are no reports of photoluminescence in the literature for the insulating phase of VO_2. This further strengthens the idea that there are no non-equilibrium carrier effects in this material, which is indeed consistent with the strong electron-phonon coupling and polaronic effects as expected in such material. This provides efficient mechanism for relaxation through interband scattering and slow diffusion. In accordance with this, metallic phase of VO_2 exhibits a very short scattering length almost at the Ioffe-Regel limit, that can be inferred from the poor conductivity of the metal and the prefactor of the activated insulator conductivity. To further support these ideas we performed several other experiments.

A second laser beam is fixed onto the center of the nanobeam, while the first laser kept scanning. Since the fixed beam is not chopped, its reflection is filtered out by the lock-in amplifier. At certain fixed laser power(for the case shown in Fid. 2.7(a) $P = 2.4$ µW), by paying the cost of elastic energy of creating another phase boundary, metallic phase is pulled in to the center of the nanobeam. This, instantly diminishes I_0 to almost zero for all positions of the first laser which is at $P = 1$ µW as shown in Fig.2.7(a). This is due to the fact that for the two phases to coexist under the same uniaxial strain temperatures at both boundaries must be the same. Although the scanning laser increases the temperature of one boundary at a pass, since metallic phase has twice the thermal conductivity and conduction through air to substrate is not significant from one boundary to another, both boundaries generate emfs of similar magnitude but opposite sign so the sum vanishes. Such a vanishing photoresponse independent of the laser position would not occur for other mechanisms. We also performed SPCM on

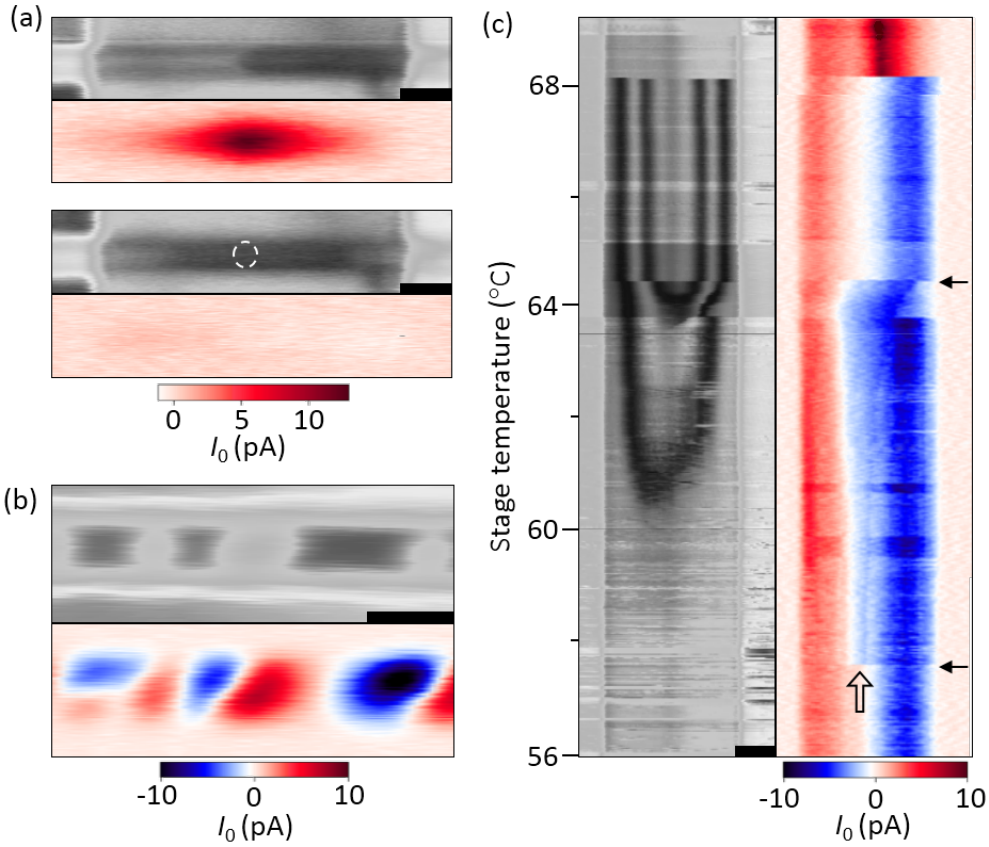

Figure 2.7: **Optical control of the photocurrent and imaging the evolution of the insulating phase** (a) Reflection and zero-bias photocurrent images at 70 ℃ with $P = 1$ µW, without(above) and with(below) a second laser($P = 2.4$ µW) focused at the location of the dashed circile. (b) Reflection and photocurrent images of an unsuspended nanobeam ($P = 0.6$ µW) (c) Reflection(left) and photocurrent (right) measured by repeatedly scanning along the centerline of a nanobeam while ramping the temperature up to and beyond the transition at 68.2 ℃. Horizontal black arrows indicate where the conversion of I_{M1} to I_{M2} begins(lower) and completes(upper). Scale bars are 2 µm for (a)-(b) and 5 µm for (c).

nanobeams that are not released from the substrate by BOE etching(see device fabrication techniques). Due to non-uniform strain alternating insulating and metallic domains occur in such devices[100]. In this case thermal conduction to the substrate is significant so that I_0 is localized at the laser spot where the temperature rise is the most significant and peaks are again centered at the I-M boundaries. Fig. 2.7(b) shows the reflection image and photocurrent map

scanned by a $P = 0.6$ µW laser above T_C. This is further supported by the fact that it takes about $P = 80$ µW to induce metallic domain around the laser spot focused on a VO_2 nanoplate on substrate at room temperature.

As mentioned in the first chapter, M1 and M2 phases can be distinguished optically using a high power microscope and polarized illumination otherwise indistinguishable optically. Understanding the properties and interconversion of these phases are crucial for a complete theory of the insulator-metal transition in VO_2 as well as for the realization of possible applications. Here, we show that SPCM technique can be used to visualize interphase boundaries and this can be generalized to visualization of other solid-state phase transitions otherwise invisible. In figure 2.7(c) a scan while temperature is ramped up, along the center of the nanobeam in the uniaxial direction is shown. Left images shows the reflection signal and the right image show the photocurrent. Below 57.5 ℃ the nanobeam is fully I_{M1} and above 68.2 it is in coexistence of I_{M2}-M and in both cases the nanobeam is straight. As the temperature ramps up, at 57.5 ℃ the photocurrent pattern changes. As temperature ramps up from 57.5 ℃ to 64.5 ℃ (marked by two horizontal arrows)a stripe pattern develops in the reflection image since the nanobeam starts buckling due to conversion of I_{M1} with shorter lattice constant to I_{M2} with longer lattice constant along the pseudo-rutile c-axis. During this process a feature in the photocurrent image appears marked by an vertical arrow and the photocurrent pattern changes. This change may reflect the nucleation of the I_{M2} phase and growing. This allows the visualization of two optically almost indistinguishable phase employing the difference between their photoresponse. Moreover, subtle differences in the properties of I_{M1} and I_{M2} phase such as Seebeck coefficients and thermal conductivities can be identified with this method.

2.3 Conclusion and Further Remarks

Results of this study is indeed not surprising. Strong electronic correlations in VO_2 is consistent with fast non-equilibrium carrier relaxation. A better picture can be drawn from these results for the conduction in VO_2 which may be interacting polaron hopping with activation. Another important aspect of this study is, it is among the first studies which investigated light-matter interactions in strongly correlated materials and our experiments shed light on usability of such materials in optoelectronic applications.

In this study we hadn't had much control over the nanobeam device's phase. Depending on the device parameters we could see M1-M2 coexistence or not. A better control over the phases would reveal many aspects about the MIT in VO_2. Combining the SPCM technique with the strain control I present in the next chapter is among our future plans. Another interesting study would be using SPCM on hydrogenated VO_2 nanobeams. This may reveal the nature of modification that hydrogenation causes on the strong correlations in VO_2. Chapter 4 is about hydrogenation of VO_2.

Chapter 3

Determining the Triple Point and the Critical Temperature of VO_2

"It doesn't matter how beautiful your theory is, it doesn't matter how smart you are. If it doesn't agree with experiment, it's wrong."

— Richard Feynman

In this third chapter of this thesis, I will discuss our measurements of the triple point and the critical temperature on strain-temperature phase diagram of the metal-insulator transition in VO_2. We designed and built a unique apparatus to apply stress and tension on nano-scale objects with extreme precision while controlling the temperature of samples with 50 mK stability*. Results of this study reveal the location of the triple point of a solid state phase transition on a strain-temperature for the first time. Strikingly we find that the triple point of the metallic phase and two insulating phases is at the transition temperature, $T_{tr} = T_C$, which we determine to be 65.0±0.1 ℃. Findings of this study are published in Nature [38].

*see Appendix C for detailed description of the apparatus.

3.1 Introduction

3.1.1 Requirements for Measurement of the Precise Phase Diagram VO_2

A precise and accurate determination of the phase stability diagram of VO_2 is important for a better understanding and theories of the MIT as well as realization of applications employing the MIT. Until recently there has been several attempts to study the strain-temperature phase diagram, however most of these experiments reported lack the required precision and sensitivity [43, 46]. There are three main ingredients for a precise and accurate measurement of the phase diagram: sensitive control of the strain, precise measurement of the applied strain and precise and accurate control of sample temperature. We achieved these three ingredients with our purpose-built strain measurement apparatus.

During the phase transitions in VO_2, major changes occur along the crystals pseudo-rutile c-axis. For instance vanadium chains along this axis dimerize and greatest change in the lattice constant happens along this axis. Thus in order to study stability of different phases under stress or tension, strain needs to be applied only along the pseudo-rutile c-axis. Moreover applied strain must be uniform along the nanobeam, otherwise multiple domains appearing will hinder the intrinsic phase diagram. This asserts the requirements that nanobeams need to be clamped from both ends firmly and suspended across a gap. In order to quantify the amount of strain applied one needs to know the change in the gap length of which the nanobeam is suspended across. Considering the fact that nanobeams are 20 to 40 μ m long, a strain of about 2% requires a control and measurement of about half a µm. Precise and accurate temperature control and uniform temperature distribution along the nanobeam are other important factors in determination of the phase diagram.

3.1.2 Experimental Setup

Here I will provide a brief overview of the apparatus. Technical details and a detailed description of the experiment setup is given in appendix C. Experiment setup consists of several components. First component is a temperature stage that is machined to house the paddle chips[†] as shown in figure 3.1. Heating elements and sensors are embedded in and mounted on several places of the temperature stage. A PCB board with metal contacts used to clamp down the chip and to make electrical contacts. Another component is the piezoelectric stage(PI MODEL P-611.10) with a sharp metal piece mounted on top as a pusher. Depending on the wide where it pushes the paddle, piezo-stage either closes the gap on the chip or opens it. Last component is the laser measurement system. A laser beam reflected off from the side of the paddle. This way depending on the gap opening, laser beam deflection angle changes and this deflection is measured by a position sensitive detector. This way precision down to a few nm is achieved in the measurement of the gap opening.

All the components of this setup is interfaced with a computer using National Instruments DAQ card and a home-brew LabView program. Temperature of the stage is controlled with a Lakeshore 325 temperature controller and interfaced to the LabView program via GPIB. Electronic transport measurements are performed under fixed voltage bias and the resulting current is measured with a Ithaca 1211 current preamplifier which is also interfaced with the LabView program. Laser gap length measurement is performed using a 632 nm laser diode pulsed with a function generator. Output of the position sensitive detector is connected to the LabView program and equipped with a software lock-in amplifier to improve signal to noise ratio of the detector. Experiments performed under a microscope with a linearly polarized light and image is captured with a 18 megapixel CMOS camera. Linear polarizer is used to distinguish M1 and M2

[†]See appendix B for the details of the micro-machined paddle chips.

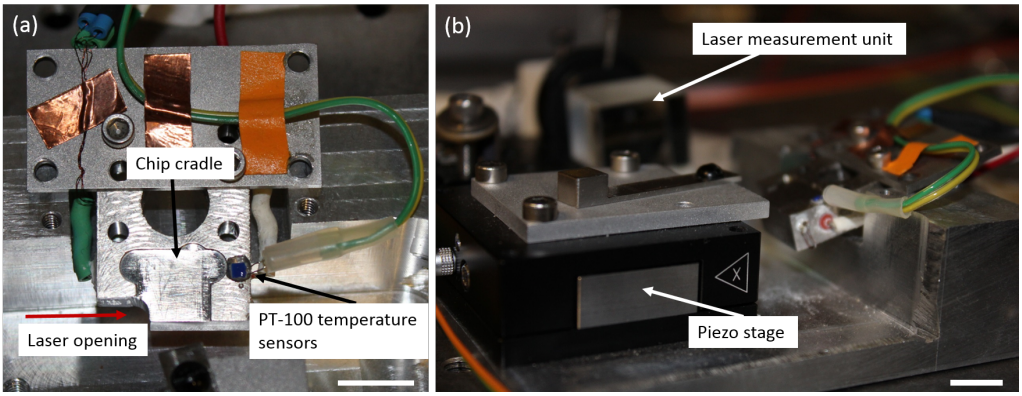

Figure 3.1: **Apparatus used to apply strain on nano-objects**(a)Top view of the setup's temperature stage. There are two PT-100 temperature sensors, one surface mounted with a high thermal conductive epoxy and the other one embedded into the invar stage, both uses 4-wire measurement. Part of the stage is removed to allow the tube that cases laser beam to get as close to the chip as possible.(b) Side view of the setup with piezo strage in and the temperature stage is shown. The stage is not bolted down. On the background beam splitter and components of the laser measurement system is visible. Scale bars are 1 cm.

phase optically[48].

3.2 Experiments

As mentioned before, our apparatus is designed to apply uniaxial tensile stress P_c along the rutile c-axis. From previous studies we expect to have the layout of phases in $P_c - T$ phase stability diagram to be as shown in Figure 3.2(a)[46, 101]. Although it is known that the free energies of M1 and M2 phases are very close near the transition[46] precise location of the triple point (T_{tr}, P_{tr}), was unknown.

3.2.1 Pinning Down the Triple Temperature T_{tr}: Fixed L

First, we determine the location of T_{tr}. Different phases on suspended VO_2 nanobeams across the paddle-chips are determined optically and confirmed by Raman spectroscopy as well as electrical measurements. By changing the gap length L and temperature T we can bring the nanobeam into coexistence of any pair of the three phases. From the predicted layout of the phase diagram we can

sketch a diagram that shows the state of the nanobeam as a function of L and T as shown in Figure 3.2(b). For a fixed length of nanobeam, we start in coexistence of M2+M1 coexistence and increase the temperature slowly. As the temperature increases the interface position y_{M2M1} changes smoothly since the stress required by the phase equilibrium changes[26]. At certain temperature $T_{\mathrm{M1}\to\mathrm{R}}$ R phase appears by reconfiguration of M1 phase. After this sudden reconfiguration, y_{M2R} changes smoothly again. The point where R phase is converted to M1 phase happens at some lower temperature $T_{\mathrm{R}\to\mathrm{M1}}$. Similarly when we start from M1+R coexistence, interface positions y_{M1R} and y_{M2R} changes smoothly above and below $T_{\mathrm{M1}\to\mathrm{M2}}$ upon warming up and $T_{\mathrm{M2}\to\mathrm{M1}}$ upon cooling down. Figure 3.3(a) shows the change of y_{M2M1}, y_{M2R}, y_{M1R} and y_{M2R} with temperature.

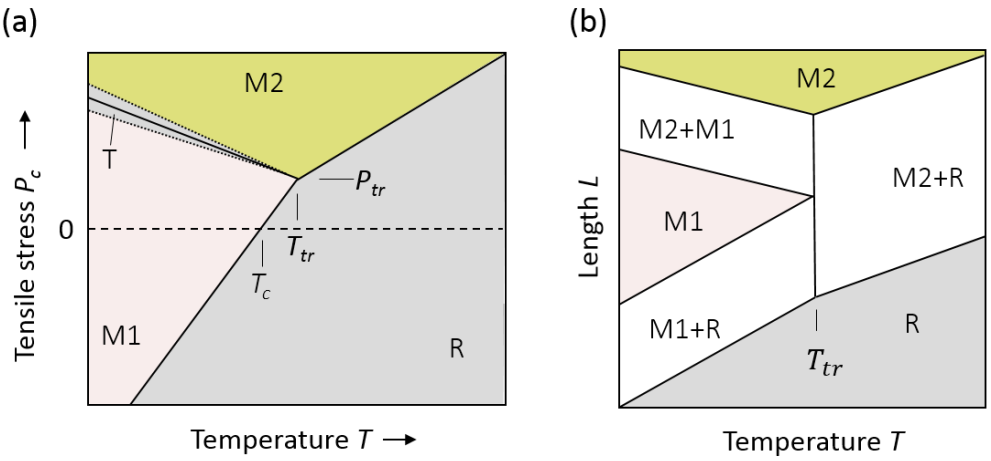

Figure 3.2: **Expected phase diagram of VO_2** (a)Expected phase stability diagram of VO_2 based on the literature. Transition is thought to be between M1 and R under no stress.(b) $L-T$ phase stability diagram.

Repeated measurements of reconfiguration temperature is taken where temperature is cycled up and down at 0.1 ℃min^{-1}. Histogram of these measurements is shown in Figure 3.3(b). For the particular device we have shown the results of measurements here, $T_{\mathrm{M1}\to\mathrm{R}} = 66.4$ ℃ and $T_{\mathrm{M1}\to\mathrm{M2}} = 65.3$ ℃. However, his-

tograms of $T_{\mathrm{R}\to\mathrm{M1}}$ and $T_{\mathrm{M2}\to\mathrm{M1}}$ are both peaked at 65 ℃. Even for different nanobeams with different lengths grown in different occasions, these two temperatures always lay between 64.9 and 65.2 ℃ range. The reason is there is always a small amount of M1 phase exists in M2+R coexistence right at the interphase boundary, often visible under microscope. On cooling therefore, there is no need for nucleation of M1 phase, so as soon as the temperature hits T_{tr} reconfiguration occurs. In Figure 3.3(c) this reconfiguration is evident from the sequence of images taken in less than a second during cool-down through 65 ℃ with a rate of 0.1 ℃min^{-1}. Here, R phase is replaced by expansion of a small wedge shaped M1 phase in between R and M2 phases upon cooling. These observations suggest that the triple point is between 64.9 and 65.2 ℃ range.

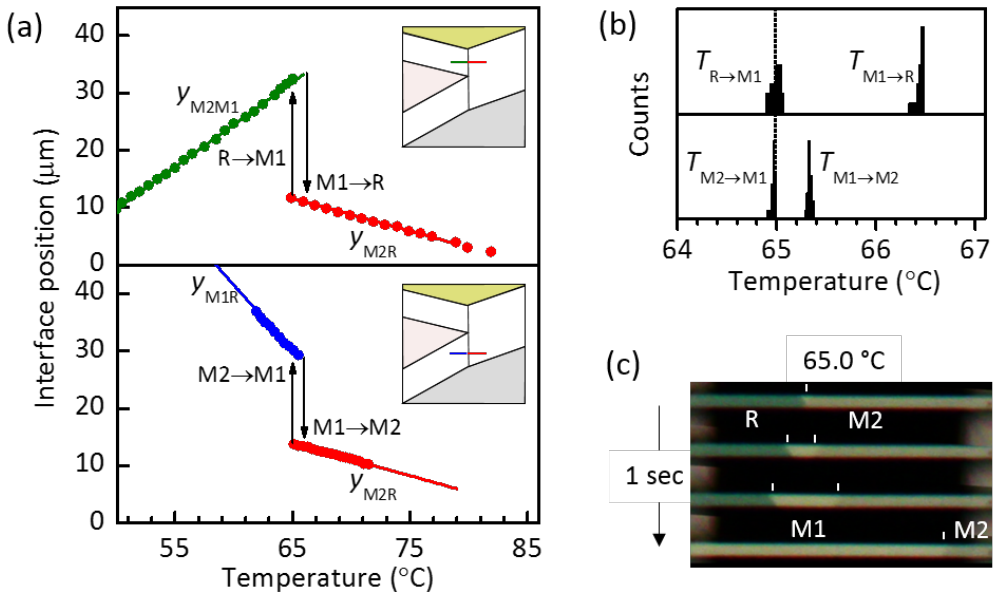

Figure 3.3: **Fixed L measurements** (a) Motion of the phase boundary with temperature at certain fixed length. Upper panel shows the transition form M1+M2 coexistence to M2+R coexistence and lower panel shows R+M1 to R+M2. Insets show the path followed in the expanded phase diagram.(b) Histogram of transition temperatures cycled many times with 0.1 ℃min^{-1} rate. Notice how $T_{R\to M1}$ and $T_{M2\to M1}$ accumulated around 65.0 ℃.(c) Sequence of images showing the expansion of M1 wedge between R and M2 while cooling down through 65.0 ℃ taken in less than a second. Gap length is 20 μm.

3.2.2 Measuring the Lattice Constants from the Interface Shift

At a given T and L, P_c is determined by the phase equilibrium for the phases in coexistence. By changing L at a fixed T, the interface moves to maintain P_c at the phase equilibrium value. In M1+R coexistence a length change by δL causes an interface shift δy_{M1R} which changes the nanobeams natural length by δL to keep the strain constant. This implies that shift in the interface must be proportional to the length change by $\alpha_{M1R} \equiv c_{M1}/c_R - 1$ where c denotes the lattice constant. Hence y_{M1R} should vary according to $dL/dy_{M1R} = \alpha_{M1R}$ and likewise $dL/dy_{M2R} = \alpha_{M2R} \equiv c_{M2}/c_R - 1$ and $dL/dy_{M2M1} = \alpha_{M2M1} \equiv c_{M2}/c_{M1} - 1$. Best linear fits to the data shown in Figure 3.4 is found to be $\alpha_{M2M1} = 0.0074, \alpha_{M1R} = 0.0100$ and $\alpha_{M2R} = 0.0174$.These values are very close to the values $0.0073, 0.0098$ and 0.0172 respectively from the literature[28, 102].

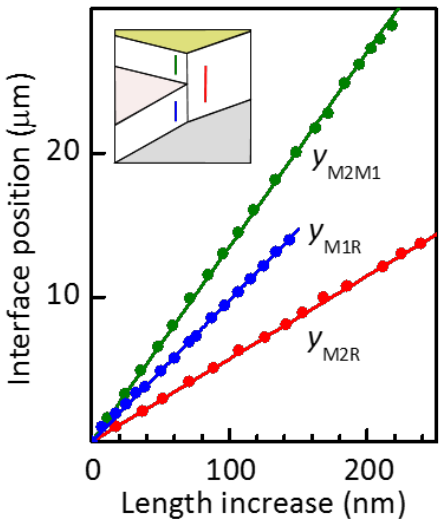

Figure 3.4: **Interface position vs. L Measurements** Slopes of interface position vs. L measurements give us the lattice constants of each phase consistent with the literature showing us the boundary motion is due to interconversion of phases only.

3.2.3 Pinning Down the Triple Temperature T_{tr}: Fixed T

Our ability to control the gap length L down to a few nm precision simultaneously with electrical resistance measurements allows us to determine the behavior very close to the triple point. The fact that different phases having different resistivities[26, 101] allow us to figure out the phase composition of the nanobeam.

First, we start measurements just below and just above 65.0 ℃. We took series of closely spaced measurements and each time we started from sufficiently small L to stabilize R phase. As L changes at 65.30 ℃ as shown in Figure 3.5(a) M2+R boundary moves smoothly. At 63.9 ℃ it changes in a more complicated way. First it starts in R phase and as the L increases, resistance shows the features for M1+R, M1 and finally M1+M2 phases. Due to first order nature of the transitions hysteresis and sudden jumps are visible in the measurements. Measurements just below and just above 65 ℃ as shown in Figure 3.5(b) shows a dramatic change between resistances of 64.95 ℃ and 65.05 ℃ . In 64.95 ℃ as the gap length increases, after a brief M1+R coexistence M1 phase persists and then M2 nucleates. Just 100 mK above R converts into M2+R directly without M1 involvement. This measurement is consistent with what we got from the fixed L measurements. We conclude that $T_{tr} = 65.0 \pm 0.1$ ℃ including uncertainties from temperature calibration and fluctuations as well as sample to sample variations.

3.2.4 Further Findings from Resistance vs. Length Measurements

First, we investigated the effect of strain on resistance of the M1 state. Activation energy of the resistance of the M1 phase increases with tensile strain, $\eta = (L - L_0)/L_0$, L_0 being the effective natural length of the nanobeam. We determine the slot width at $\eta = 0$ using our knowledge that the triple point is at zero strain which corresponds to roughly 300 nm length increase in Figure 3.5(c). The dotted lines in Figure 3.5(c) shows $R \propto exp[-(\Delta_0 + \gamma\eta)/k_BT]$ using coefficient values $\Delta_0 = 0.31$ eV and $\gamma = 0.77$ eV, where k_B is the Boltzmann's constant. These values give the best fit to our data shown.

We determined the ratio of resistivities of M2 and M1 phase from the variation of R in M1+M2 coexistence. As the nanobeam gradually converts from M1 to M2, the interface position y_{M2M1} changes from 0 to L_0. We can deduce the ratio

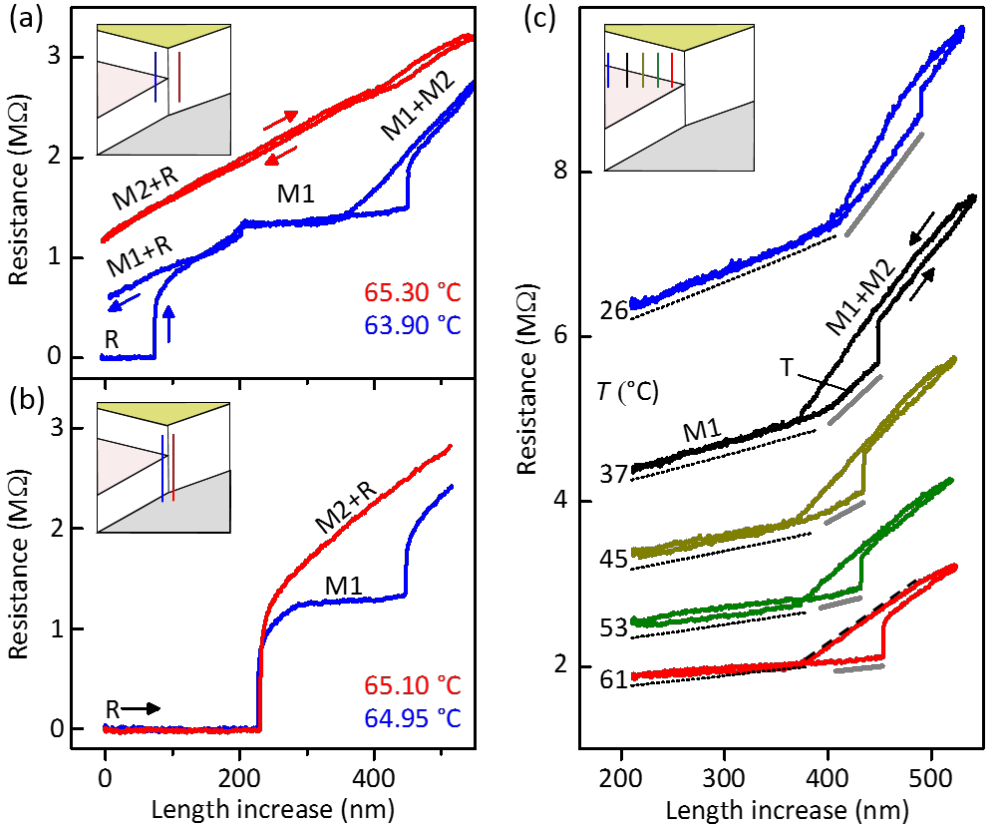

Figure 3.5: R **vs.** L **Measurements** (a) Motion of the phase boundary with temperature at certain fixed length. Upper panel shows the transition form M1+M2 coexistence to M2+R coexistence and lower panel shows R+M1 to R+M2. Insets show the path followed in the expanded phase diagram. (b) Histogram of transition temperatures cycled many times with 0.1 ℃ min^{-1} rate. Notice how $T_{R\to M1}$ and $T_{M2\to M1}$ accumulated around 65.0 ℃. (c) Sequence of images showing the expansion of M1 wedge between R and M2 while cooling down through 65.0 ℃ taken in less than a second. Gap length is 20 µm.

of their resistivities using

$$R = R_{M1} + (R_{\mathrm{M2}} - R_{\mathrm{M1}})\frac{y_{\mathrm{M2M1}}}{L_0} \tag{3.1}$$

from which we have

$$\frac{1}{R_{\mathrm{M1}}}\frac{dR}{dL} = \left(\frac{R_{\mathrm{M2}}}{R_{\mathrm{M1}}} - 1\right)\frac{1}{L_0}\frac{dy_{\mathrm{M2M1}}}{dL} = \left(\frac{\rho_{\mathrm{M2}}}{\rho_{\mathrm{M1}}} - 1\right)\frac{1}{L_0}\frac{1}{\alpha_{\mathrm{M2M1}}} \tag{3.2}$$

and thus

$$\frac{\rho_{\mathrm{M2}}}{\rho_{\mathrm{M1}}} = 1 + \frac{\alpha_{\mathrm{M2M1}} L_0}{R_{\mathrm{M1}}} \frac{dR}{dL} \tag{3.3}$$

Using equation 3.3 we can deduce that $\rho_{M2}/\rho_{M1} = 2.3 \pm 0.2$. This ratio hasn't been determined accurately before. In addition we find that $\rho_{\mathrm{M2}}/\rho_{\mathrm{M1}}$ does not change by more than 5% between 26 and 64 ℃, implying that the activation energies are equal to within a few percent.

Another implication from these resistance versus length measurements is continuous distortion of M1 phase into the T phase. The additional increase in R as the length increases, indicated by the gray lines in Figure 3.5(c) show that there is a phase between M1 and M2 with higher resistivity than M1 and that phase is unstable relative to M2 at all temperatures from T_{tr} to below 26 ℃. Also this finding is shown on the phase diagram (Figure 3.7) by a gray shaded strip.

3.2.5 Determining the Critical Temperature of Transition

To determine the critical temperature of the transition, which is the condition where $P_c = 0$, we break the nanobeams using a nanomanipulator after all the measurements have been completed. Once broken, we end up with two cantilevers pointing each other. When we start from M1 phase and warm up toward T_c, as we brought the cantilevers together, compression produces a domain of R phase in one of them. After retraction, this domain only persists only above a certain temperature. Below it, it shrinks as the compression removed. This temperature is the T_c. An example of the measurement is shown in Figure 3.6. By performing this experiment on several devices we concluded that T_c is equal to T_{tr} within an uncertainty of 50 mK governed by the temperature fluctuations, $T_c = T_{tr} \approx 65.0 \pm 0.1$ ℃. This discovery may have important implications about the nature of this solid state phase transition and may be useful for development of more accurate theories of the MIT in VO_2.

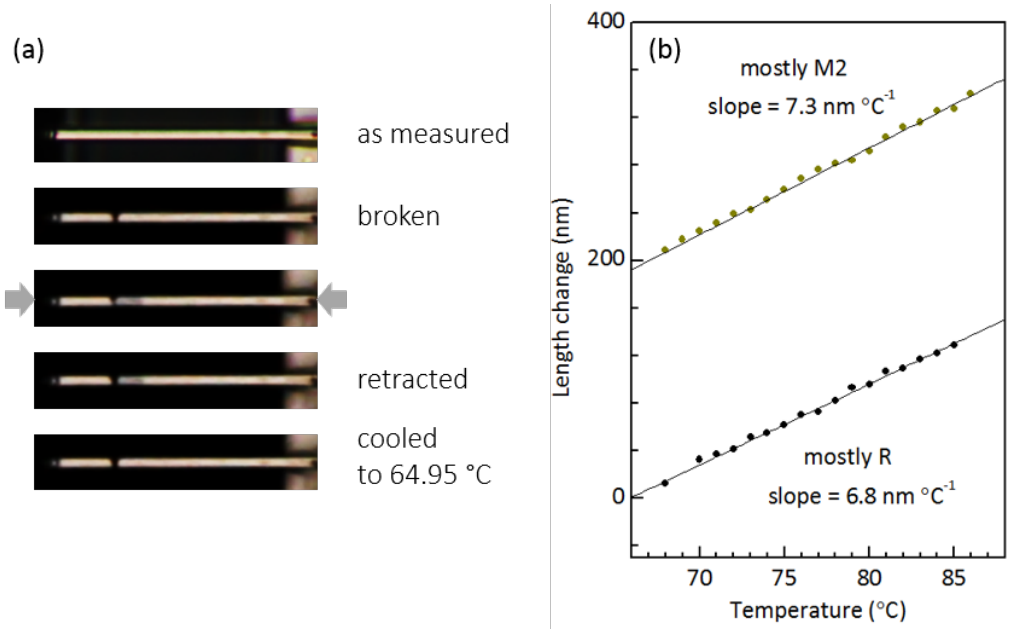

Figure 3.6: **Finding the critical temperature and the effect of thermal expansion** (a) The transition temperature T_c at zero stress is measured by finding the temperature above which the metallic phase becomes stable in a cantilever, as illustrated here.(b) Measurements of length change needed to maintain a fixed M2-R interface position yielding a difference in thermal expansion coefficients $K_R - K_{M2} \approx 0.17 \times 10^{-4}$ °C.

3.2.6 Constructing the Phase Diagram

As mentioned before, construction of the phase stability diagram of VO_2 is crucial for both understanding the MIT in VO_2 and for the realization of applications using VO_2. To construct the phase diagram we used measurements from ten nanobeams. The shape of the phase boundaries between phases can be deduced from measurements of interface position y_{ij} vs T where i and j denotes M1, M2 or R phases. The idea is, since the nanobeams are straight and the stress is applied from the ends, the stress in coexistence should be nearly uniform. Therefore phase equilibrium $P_c(T)$ at the interface must be equal to the stress along the nanobeam. Assuming similar values for the Young's modulus E for each phase then the axial strain has a uniform value $\eta = P_c/E$. Although a recent study[103] reports evidence of a difference between M1 and M2 about 10-20% this would still

have not much effect on our results. Moreover even if E we substantially different its only effect would be altering the phase boundary slopes somewhat but would have no effect on our main conclusion. η varies with temperature according to

$$\frac{1}{E}\left.\frac{\partial P_c}{\partial T}\right|_{ij} = \left.\frac{d\eta}{dT}\right|_{ij} = -\frac{\alpha_{ij}}{L_0}\frac{dy_{ij}}{dT} - \Delta K \tag{3.4}$$

where L_0 is the effective clamped length. $\Delta K = K_{VO_2} - K_{Si}$ is the thermal expansion mismatch between the nanobeam and the silicon substrate. We choose not to compensate for the thermal expansion mismatch since the thermal expansion coefficients are not known accurately and the effect is not larger than the spread in the measurements between devices. We measured the difference in K_{VO_2} for different phases by comparing measurements made for the nanobeam mainly in phase i with those for it meanly in phase j. For example in Figure 3.6 measurements made for R+M2 coexistence where $L_0 = 40$ µm is shown. Here, to keep y_{M2R} constant while changing the temperature, we varied the gap length. We find a 0.5 nm $^{\circ}C^{-1}$ difference in the slopes for the nanobeam with suspended part mostly R and 75% M2. This difference results solely from the difference between K_R and K_{M2}, which should be about $0.75L_0 \times (K_R - K_{M2}) \approx 0.17 \times 10^{-4}$ $^{\circ}C^{-1}$. This is consistent with the values reported in the literature.

For the monoclinic phases[102], $K_{VO_2} \approx 0.12 \times 10^{-4}$ $^{\circ}C^{-1}$ giving $\Delta K \approx 0.09 \times 10^{-4}$ $^{\circ}C^{-1}$, with $K_{Si} = 0.03 \times 10^{-4}$ $^{\circ}C^{-1}$. For the R phase[102], $K_{VO_2} \approx 0.30 \times 10^{-4}$ $^{\circ}C^{-1}$, but typically we perform experiments with about half of the nanobeam metallic, in which case $\Delta K \approx 0.2 \times 10^{-4}$ $^{\circ}C^{-1}$. Hence ΔK gives a correction to the phase boundary slope less than 10%.

To draw the phase diagram of VO_2, we deduced $P_c(T)|_{ij}$ from measurements of y_{ij} versus T. A constant from each $y_{ij}(T)$ dataset is subtracted to set $y_{ij} = 0$ at $T_{tr} = 65.0$ $^{\circ}C$since triple point is at zero stress. Then plugging y_{ij} dataset in to equation 3.4 with proper L_0 with some allowance for a slightly different apparent clamping length. Another constraint comes from the Clausius-Clapeyron

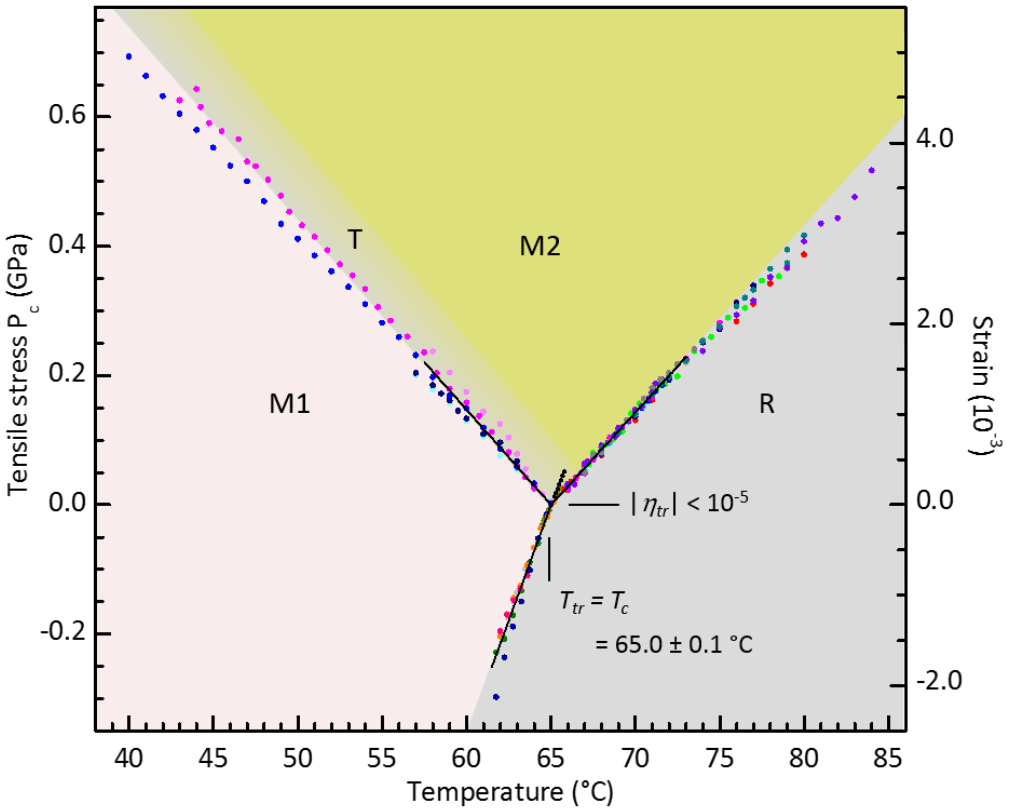

Figure 3.7: **Phase stability diagram of VO_2** Deduced stress-temperature phase diagram. The small black filled circles are for the superheated M1 phases. The grey shaded strip is where a metastable T phase can occur.

relations,

$$\frac{1}{E}\left.\frac{\partial P_c}{\partial T}\right|_{ij} = \frac{S_j - S_i}{b^2(a_i - a_j)} \approx \frac{S_j - S_i}{\alpha_{ij} V} \tag{3.5}$$

where S_i is the entropy per vanadium pair and $b = 4.55$ Å is the base length and $V = b^2 a_{\mathrm{R}} = 59$ Å is the volume of the tetragonal unit cell. Using equation 3.4, we can eliminate entropy terms in the Clausius-Clapeyron equation which will give us

$$\alpha_{\mathrm{M2M1}} \left.\frac{\partial \eta}{\partial T}\right|_{\mathrm{M2M1}} + \alpha_{\mathrm{M1R}} \left.\frac{\partial \eta}{\partial T}\right|_{\mathrm{M1R}} = \alpha_{\mathrm{M2R}} \left.\frac{\partial \eta}{\partial T}\right|_{\mathrm{M2R}} \tag{3.6}$$

The deduced boundary slopes from this constrain equation is shown in Figure 3.7 by the solid straight lines. We obtained a specific latent heat $T_c(S_{\mathrm{R}} - S_{\mathrm{M1}})/V = 1020$ cal/mol from the slope of the line fit to the M1-R phase boundary

($\partial P_c/\partial T|_{M1R} = 71$ MPa °C^{-1}). This value is consistent with the previously reported measurements in macroscopic crystals[11]. Similarly we deduce 710 cal/mol for both M2-R and M2-M1 phase boundaries with $\partial P_c/\partial T|_{M1R} = 29$ MPa °C^{-1}. As indicated on the phase diagram, strain at the triple point is less than 1.0×10^{-5} since T_{tr} and T_c is equal within $\delta T \approx 0.05$ °C. Entropy differences per vanadium chain is deduced to be $S_{\mathrm{R}} - S_{\mathrm{M1}} = (3.0 \pm 0.3) k_B$ and $S_{\mathrm{R}} - S_{\mathrm{M2}} = (2.1 \pm 0.1) k_B$. Also the temperature dependence of the Gibbs free energies G_i of the phases of unstrained VO_2 is sketched in Figure 3.8 by setting $G_{\mathrm{R}=0}$. The slopes are entropies $S_i = -dG/dT$ at zero stress. At the MIT we find that M1 and M2 phases are simultaneously degenerate with R phase.

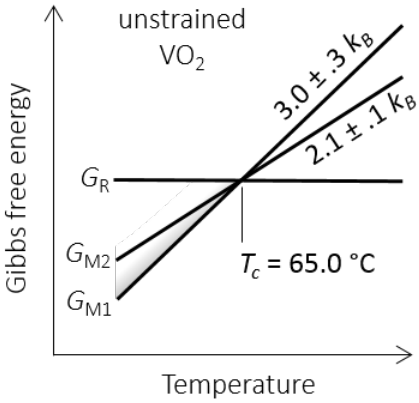

Figure 3.8: **Gibbs free energy of phases** At triple point free energies of the phases become degenerate.

3.3 Conclusions and Further Remarks

Current models of the MIT in VO_2 doesn't include or explain most of the facts revealed in our experiments. We believe findings in this study will be crucial ingredients for development of mew models of this phase transition as well as realization of the applications employing it. This study revealed the first precise phase diagram of a solid state phase transition and techniques used in this study can be employed in studying different systems. For instance using the methods developed here can be used to study properties of 2D layered transition metal dichalcogenides. It is known that strain causes some changes in electronic properties in such materials [104, 105]. However there are only preliminary studies that investigated such effects and our scheme provides a precise and well con-

trolled way. Combining optical methods with our setup as mentioned at the end of chapter 2 will provide an excellent platform to study the effects of strain on optoelectronic properties of such nano-scaled materials. There are also things we can learn from strain measurements on hydrogenated nanobeams of VO_2 as discussed in chapter 4. Studying the effects of hydrogen on the phase stability may reveal how hydrogen modifies the strong correlations and suppresses the MIT depending on the hydrogen concentration.

One limitation of the strain setup is that it is designed to work under ambient conditions and at slightly elevated temperatures. It is not small enough to fit into a cryostat or a TEM chamber. A new design is needed to perform studies at such closed environments. However there are many nano-fabrication challenges for applications of strain and also for gap spacing measurement. Also, one of the main advantages of our strain setup is that cost of each chip is less than $100 since it doesn't contain any active elements on it. This simplicity made it possible to study many different samples over a short period of time. However a chip that can fit into a small chamber must have active elements on chip which increases fabrication time and costs.

Chapter 4

Hydrogen Doping of VO_2

"Soon I knew the craft of experimental physics was beyond me- it was the sublime quality of patience - patience in accumulating data, patience with recalcitrant equipment which I sadly lacked."

— Abdus Salam

Doping crystals by replacing few atoms in the lattice, intercalation of atoms into the crystal or by creating vacancies is an important modification for material processing technologies. For instance, currently semiconductor technology relies on doping of silicon with boron or phosphorus to change electronic conduction properties of the pure silicon crystal. This allows fabrication of devices such as transistors, diodes etc. Another example of doping is using rare-earth metals such as neodymium, erbium, ytterbium into crystals or quartz core in fiber optics. These are used as for making lasers where doped crystal acts as a gain medium. As another example, reversible intercalation of lithium ions inside polymers allow charge generation.

In VO_2 there are several dopants that can alter the MIT temperature and the transition properties. For instance chromium stabilizes M2 phase[28]. Another dopant known for VO_2 is tungsten[106], which decreases the MIT temperature.

Such control over the phases and the MIT in VO_2 enables more possibilities for applications. Another dopant for VO_2 is hydrogen, which is the least studied of all the dopants mentioned above. There are only two papers in the literature [37, 107] and only a little is known about the nature of hydrogenation in VO_2. In this part of the thesis I will discuss our findings about the hydrogenation in VO_2.

4.1 Introduction

Hydrogen is one of the most promising fuels among the alternatives to hydrocarbon based fuels[108, 109]. There are several reasons for that. Firts, hydrogen is the most abundant material on earth, although most of it is in molecular form. Second, even using hydrogen as a fuel in an internal combustion engine will increase the efficiency of the engine and also since the only product of this combustion is water, carbon emission will be zero. Third, there are novel methods to produce electricity by combining hydrogen with oxygen and this electricity can be used to drive several more efficient and less costly electric motors. However, low density, and low ignition energy of hydrogen makes storage and transportation for practical uses difficult[110, 111]. Other reason for the interest in diffusion of hydrogen in materials is the changes that it causes in the electronic and the crystal structure. For instance hydrogen passivates shallow impurities[112], saturates dangling bonds at surfaces, grain boundaries and vacancies in semiconductors[113]. In silicon industry, such effects may play significant role in device performance and fabrication. Another example is the hydrogenated ZnO[114], an n-type semiconductor with a band gap of about 3.4 eV. Due to large band gap, ZnO has been utilized as active layer in transparent thin-film transistors[115]. Electrical conductivity of the ZnO crystals heated in hydrogen environment is higher and the process is reversible[116]. The importance of hydrogen in ZnO is the fact that during the growth of ZnO crystals hydrogen is present in the envi-

ronment. Since hydrogen acts as a donor, making functional devices consisting of p-type ZnO becomes harder[117]. Final example I am going to discuss is the hydrogenation of TiO_2. Rutile TiO_2 has the same crystal structure as the metallic VO_2, titanium atoms arrayed on a body-centered tetragonal sub lattice and octahedrally coordinated to the oxygens. This arrangement results in open channels in the crystal parallel to the c-axis. As demonstrated in the late 70's, these channels are the reason for large anisotropy in the diffusion of hydrogen[118, 119]. Hydrogen forms an O-H bond with the oxygen atoms in the octahedral. Vibrational modes can be detected by infrared absorption and Raman spectroscopy. Hydrogenation also alters the electronic conductivity in TiO_2[120].

A better understanding of hydrogenation in materials is important for both fundamental aspects and applications in hydrogen sensing, storage, generation, transparent optoelectronics and material processing. VO_2 offers a unique platform for studying hydrogenation of materials for several reasons. First, unlike any other material hydrogen gradually decreases the insulating gap[37] and above certain concentration it suppresses the MIT. This allows optical observation of hydrogenation since it manifest itself as color change. Second, effects of hydrogenation on strongly correlated materials aren't known well. Alterations to strong correlations may lead to better control over the observed phenomena. Third, a better understanding of hydrogenation in VO_2 may lead to applications in hydrogen sensing and production.

In the early paper by Chippindale et al.[107] hydrogenated VO_2 (H_xVO_2, $0 < x < 0.37$) is prepared by both hydrothermal synthesis and spillover method. The vibrational spectrum has been measured using elastic neutron spectroscopy. Hydrogen amount in the unit cell is determined by X-ray diffraction on H_xVO_2 powder. For the values of $0 < x < 0.08$ VO_2 retains monoclinic phase while in the range $0.16 < x < 0.37$ it converts to a distorted rutile like orthorhombic structure. Experiments performed at 80 K and vibration frequencies calculated

for H_xVO_2. Results show that hydrogen forms bond with oxygen in a similar way to hydrogen in TiO_2.

More recent paper from Natelson's group by Wei et al. reports measurements and *ab* initio calculations of hydrogenation in single crystal VO_2 nanobeams similar to described in this thesis. They show that Raman shift in the range from 100 to 950 cm^{-1} for hydrogenated VO_2 at room temperature is similar to metallic VO_2 above T_c(Figure 4.1(a)). Moreover, electronic transport measurements revealed that as the hydrogen amount increases in the crystal, energy gap of the insulating state gradually decreases as shown in Figure 4.1(b). This indicates that hydrogen modifies the strong correlations. Nature of this modification is unclear. Selected area electron diffraction with limited resolution indicates that hydrogenated VO_2 has either orthorhombic as reported before[107] or rutile structure (Figure 4.1(c)).

This is more or less all known about hydrogenation of VO_2. In the following sections I will present the results of our studies performed on single crystal nanobeams.

4.2 Experiments

To understand the intrinsic behavior of hydrogenated VO_2, crystals need to be strain free. Complications from strain may alter the hydrogen diffusion characteristics and make it harder to interpret the results. Thus we either used cantilevered nanobeams or crystals on a soft polymer, PDMS, where former is proven to be superior over the nanobeams on PDMS. A thin layer, 1 nm of Pd acts as a catalyst to break molecular hydrogen gas to atomic hydrogen and speeds up the process. Unless otherwise stated all the devices used in our experiments are coated partially with Pd. Details of the fabrication processes of these samples are given in appendix B. Hydrogenation of VO_2 takes place in an hydrogen rich environment, at temperatures usually around 150 ℃. We built a purpose made

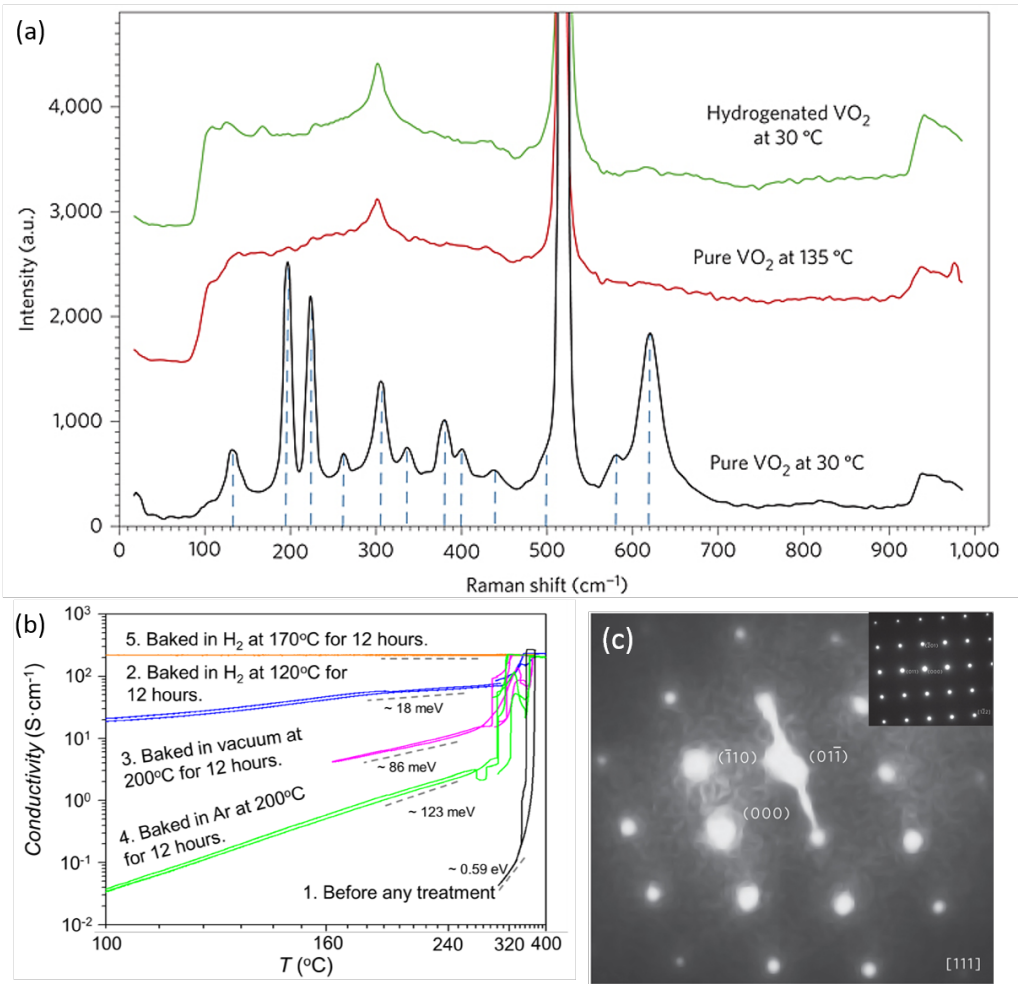

Figure 4.1: **Hydrogen Doping of VO_2** Graphs from Wei et al. [37] showing (a)Raman measurements of both hydrogenated and normal crystals, (b)electronic conductivity change with hydrogenation and (c) selected area electron diffraction of M1 phase.

hydrogenation setup to have a better control over the process. Details of the setup is given in appendix D.

4.2.1 Anisotropy of Hydrogen Diffusion in VO_2

First we looked at the anisotropy of hydrogen diffusion in VO_2. A nm of Pd is evaporated on to VO_2 on PDMS and diffusion of hydrogen is observed from metallic region formation. As shown in Figure 4.2(a) dark regions only appear

at the facets that lead to rutile c-axis. There is no observable color change that diffuses from other facets. Also, by evaporating Pd to a part of the $(\bar{2}01)$ facet, we observe hydrogen diffusion only along the c-axis direction. These observations indicate that the hydrogen diffusion is much faster along the rutile c-axis, very similar to what is observed in TiO_2. To see the extent of this similarity we did a preliminary measurement of the diffusion coefficient of hydrogen in VO_2, $D_{c\|}^{\text{r-VO}_2}$ parallel to the rutile c-axis. Hydrogenation performed at 100 ℃ and pictures of the sample are taken after certain intervals of hydrogenation at several different temperatures. Images taken at 60 ℃ are used to have an enhanced contrast of the hydrogenated region. We find that $D_{c\|}^{\text{r-VO}_2} \approx 2.0 \times 10^{-11}$ cm^2/s. This is very similar to the value measured in TiO_2, $D_{c\|}^{\text{r-TiO}_2} = 1.8 \times 10^{-11}$ cm^2/s [121]. Experimental data and images are shown in Figure 4.3. Diffusion coefficient is calculated using Fick's law in 1D, $L \approx 2\sqrt{\tau D_{c\|}^{\text{r-VO}_2}}$, where L is the diffusion length measured from the length of the metallic region. τ is the exposure time to hydrogen gas. However the anisotropy of diffusion shows that if Pd layer does not cover some parts of the beam, hydrogenation happens nonuniformly along the nanobeams. This leads to complications due to lattice constant mismatch between hydrogenated parts and non-hydrogenated parts. For instance, if Pd layer is evaporated straight from the below as shown in Figure 4.2(b)-iii, only top portion of the beam facets gets covered by Pd. This results in hydrogenation of top potion only as shown in Figure 4.2(a).

To overcome this problem we fabricated cantilevered beam devices. This allowed us to evaporate Pd onto entire $(\bar{2}01)$ facet as explained in appendix B and this strain-free nanobeams demonstrate intrinsic behavior of hydrogenated VO_2.

4.2.2 Supercooling of Hydrogenated VO_2

We observe supercooling of the metallic phase in VO_2 down to liquid nitrogen temperatures, especially when they are on PDMS. After hydrogenation, since we

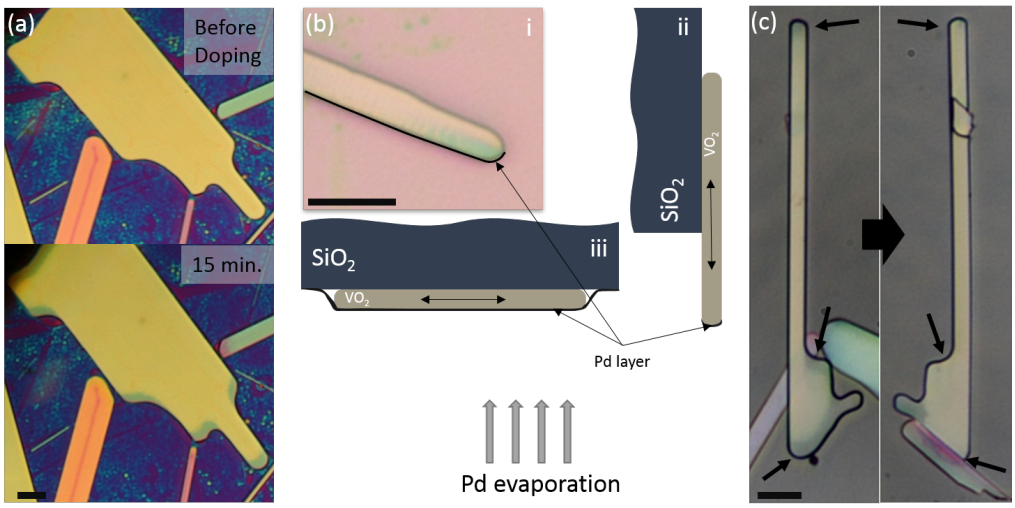

Figure 4.2: **Anisotropy of hydrogen diffusion and the effect of Pd evaporation** (a) Crystals showing anisotropic diffusion. There is no color change in the middle part of the crystal as well as from the sides. However, facets leading to the rutile c-axis shows dark regions after 15 min exposure to hydrogen gas at 150 ℃.(b)Pd is evaporated i- slanted, to one side of the beam only as depicted by a black line. Only the part of the $(\bar{2}01)$ facet is covered. ii shows Pd evaporation to a cantilevered beam and iii shows evaporation on top directly.(c)Pd evaporated on to top surface of the crystal on PDMS and the right picture shows bottom of it. Black arrows indicate hydrogenated regions and after flipping the crystal upside down these regions look insulating. This confirms that Pd only covers a small part at the top of the crystal and hydrogen doesn't diffuse in other directions as fast as it diffuses along the rutile c-axis.(c)Top picture shows Scale bars are 10 µm.

perform hydrogenation at temperatures above the T_c, even after cooling down to room temperature crystals stay metallic. Depending on the hydrogenation time, we observed supercooling down to liquid nitrogen temperature. Only after reaching that temperature, most of the crystal turns insulating. Only the regions that are close to the $(\bar{2}01)$ facets, which gets the most of the hydrogen, stays metallic. Increasing the temperature gradually turns insulating parts into metallic. If there are regions in the crystal that hydrogen hasn't diffused during the hydrogenation process, the nanobeam turns metallic completely only after reaching $T_c = 65$ ℃. Supercooling can be observed repeatedly by cycling up and down the T_c. Figure 4.4 shows series of hydrogenation steps that decreased the

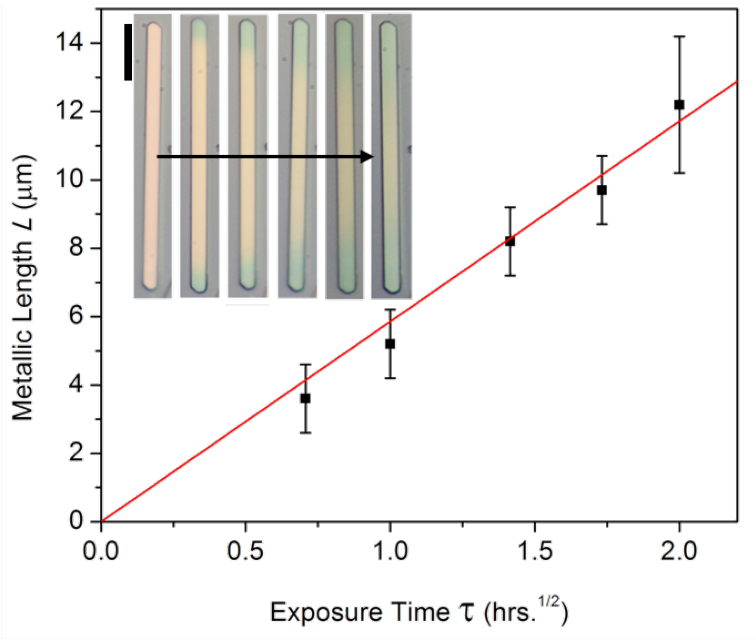

Figure 4.3: **Preliminary measurement of the diffusion coefficient** Graph shows the length of the metallic region stabilized by the hydrogen vs square root of exposure time. Using Fick's law in 1D, we derived the diffusion coefficient of hydrogen at 100 ℃. Inset shows the images after series of hydrogenation ranging from half an hour to 4 hours, increasing from left to right indicated by the black arrow. Scale bar is 10 μm.

supercooling temperature.

Supercooling of the hydrogenated metallic phase in cantilevered beams, however, is not as prominent as the beams on PDMS. Although the exact nature of this phenomenon is not known to us, we believe, doping only the upper parts of the crystals on PDMS plays a role. The idea is, at temperatures above the T_c hydrogenated regions are stable in the metallic phase. As it cools down to room temperature, bottom portion turns to insulator but this transition doesn't destabilize the hydrogenated metallic layer on the top. As lower temperatures are reached, region in the top middle of the crystal turns insulating since it has less hydrogen concentration than the ends. Warming up to room temperature is not enough to induce the metallic phase in most regions where the T_c is reduced by only a few degrees from its intrinsic value. However a more detailed study is

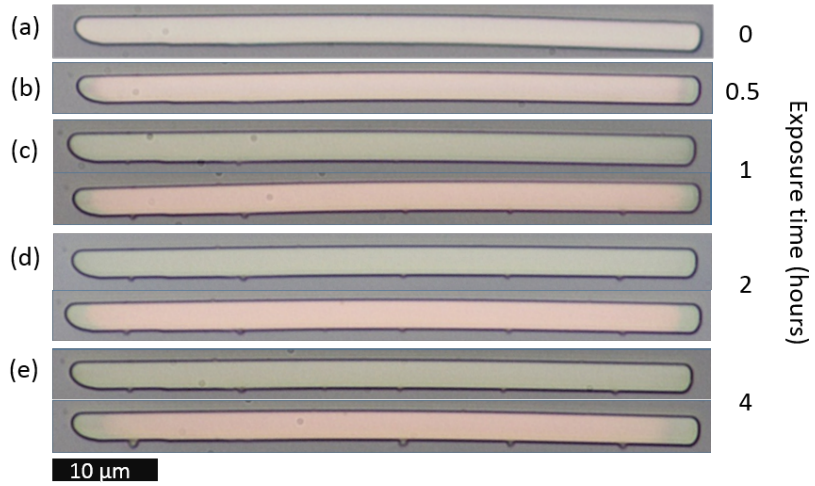

Figure 4.4: **Supercooling of the hydrogenated metallic phase.** All pictures are taken at room temperature and hydrogenation is performed at 100 ℃. (a)Before hydrogenation, (b)after half an hour no supercooling, (c) after total of 1 hour. Upper picture is right after doping, lower picture is after cooling down to -10 ℃. (d)After 2 hours total, this time insulator appears below -20℃ and (e) after 4 hours insulator is retrieved by dipping the sample into liquid nitrogen, so it is somewhere between -20 ℃ to -196 ℃.

required to elucidate this claim. Another aspect of supercooling is, after several hours over the hydrogenation, without need to cooling down to low temperatures, most of the crystal, except highly doped regions relaxes to insulating phase. This is only observed in crystals on PDMS, which suggests that the observed effect might be due to PDMS substrate such as slow relaxation of PDMS with time.

4.2.3 Segregation of Hydrogen in VO_2

One of the most intriguing aspects about hydrogenation of VO_2 is segregation of hydrogen over time. The effect can be observed in two ways. First, if hydrogenation is performed under low concentration hydrogen environment at temperatures slightly above the T_c such as 90 ℃, it takes about 3 hours under 5 mL/min H_2 and 10 mL/min Ar flow to have a 15 micron hydrogenated region on the cantilevered beam. As the beam cools down from T_c first non-hydrogenated part turns insulating. Following that, rather than the metal-insulator interface gradu-

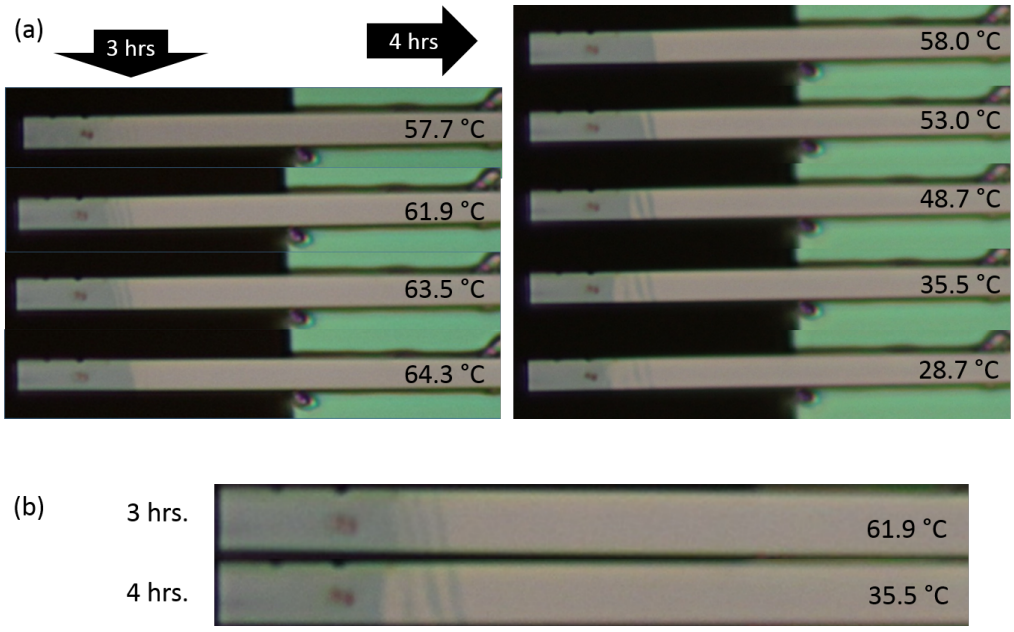

Figure 4.5: **Formation of stripes on cantilevered nanobeams.** (a)1.2 nm of Pd layer is evaporated to the tip of the nanobeam only. Sequence of images shown at the left is after exposure to hydrogen for three hours and the sequence on the right shown same nanobeam after 1 more hour of hydrogenation at the same conditions, 90 ℃ and same hydrogen concentration. To show how stripes evolve sequences of images are shown at different temperatures. (b) Comparison between stripes after 3 and 4 hours of exposure. After 3 hours stripe separation is 0.9 µm while after 4 hours it is 1.3 µm. Length of the free part of the beam is 27.5 µm.

ally moving, parts further from the tip of the cantilever starts turning into insulator in discrete jumps. As a section of the beam turns insulator it leaves a thin stripe, usually about a micron wide, behind.As the temperature decreases number of stripe increases till at certain temperature stripes start to disappear in the order they appeared. Second occasion where we observe that kind of formation is hydrogenated crystals on PDMS. After a certain amount of time, which is not known to us exactly similar stripes form. For instance, a sample hydrogenated 2 months before shows a stripe near the end. Figure 4.5(a) shows series of images taken at different temperatures and how the metallic region changes with temperature. Figure 4.5(b) shows pictures taken after 3 and 4 hours of exposure to same hy-

drogen environment at 90 ℃. These pictures are selected to show the differences. These observations suggest that there are at least two mechanisms governing the motion of the hydrogen inside the VO_2 crystal. One of them is the diffusion of hydrogen within the crystal which spreads the hydrogen. Another mechanism is the one responsible for the segregation. This might be resulting from the fact that hydrogen atoms are more stable in the metallic phase than the insulating phase, so such segregation lowers the free energy of the hydrogenated crystal. At temperatures near or below the T_c this mechanism is faster than the diffusion which results in such segregation. At higher temperatures however, since diffusion is much faster and hydrogenation happens in minutes we don't observe formation of stripes. However, again these claims need more evidence to be supported and even if the explanation is correct we don't know why hydrogen prefers to accumulate in a small region rather than diffusing to entire crystal.

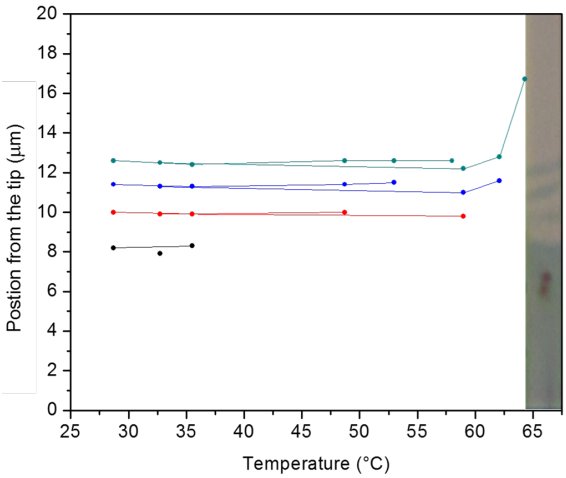

Figure 4.6: **Position of the stripes over a temperature cycle.** Graph shows the change of positions of the stripes with temperature.Cycle starts from 58 ℃ and after cooling down, we ramp up to 64.9 ℃.

4.2.4 Hysteresis in Metallic Length

To see how the metallic region induced by the hydrogen depends on the sample temperature we did several temperature cycles and measured the metallic length L_T from the tip of the cantilever. A cantilevered beam with 1 nm Pd coated on to the tip is hydrogenated for 10 and 15 minutes at 120 ℃. Temperature

cycle is started at 27 ℃ for both 10 and 15 mins. L_T doesn't expand, indeed it shrinks by fraction of a micron till above 40 ℃. Then most of the time close to the T_c, cantilever becomes fully metallic(Figure 4.7). Cooling down shows a different and more monotonic pattern. Once a certain temperature is reached, L_T decreases smoothly. In our experiments we cooled slightly below zero and metallic phase persisted. Heating from the lowest temperature follows a similar pattern to the initial warm up. L_T starts increasing only after certain temperature which is about 40 ℃. We believe steady decrease in the metallic length with

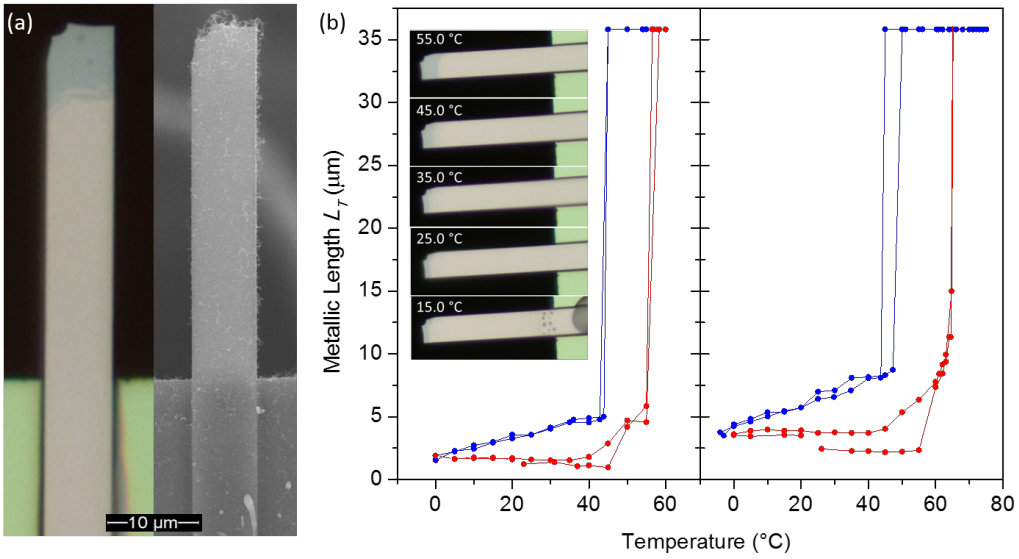

Figure 4.7: **Hysteresis of the metallic length** (a)1 nm of Pd layer is evaporated to the tip of the nanobeam only. Hydrogenation is performed at 120 ℃ for 10 mins. and 15 mins. Optical and SEM images are shown. Flakes seen in the SEM image are due to an exploded indium contact. (b) Graph on the left is change of the metallic length from the tip of the nanobeam with temperature after 10 mins and the graph on the right after 15 mins. Red lines indicate warming and blue lines indicate cooling. There are two cycles in both graphs. Inset shows the change of metallic region with temperature after 10 mins. of hydrogenation. Free beam length is 37.5 µm.

temperature indicates the hydrogen density along the nanobeam. Position where the jump to fully metallic state happens at the position where beyond there is no hydrogen. Line fit to the decrease in L_T with temperature indicates that for 10 min. exposure $L_T = 0$ will be at ~ -20 ℃ and for 15 min. exposure ~ -40 ℃

with 0.074 µm/℃ and 0.095 µm/℃ slopes respectively. A more detailed study is required to interpret the results of these measurements.

Another observation we made is the size of the nanobeam has no considerable

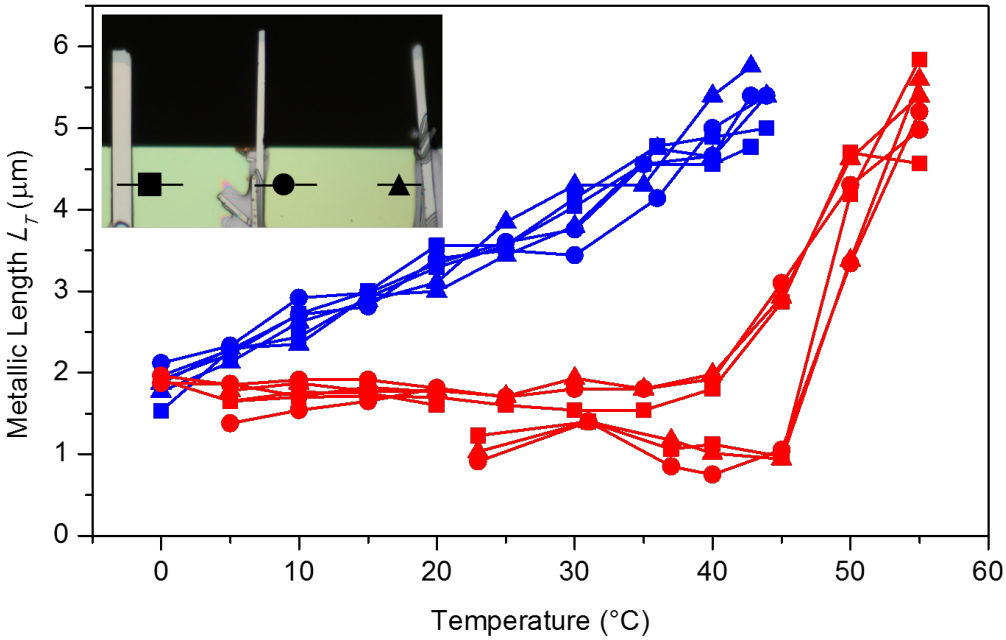

Figure 4.8: **Effect of the beam dimensions on hydrogenation .** Graph shows the change of metallic length L_T with temperature of three different nanobeams on the same substrate as shown in the inset. All three beams essentially show same temperature dependence. Only coexistence regime is shown for clarity.

effect on the formation of metallic domain, which is consistent with diffusion being 1-dimensional. As shown in Figure 4.8 all three beams with different dimensions show no distinguishable temperature dependence of L_T. This is the same device presented earlier in this subsection. The length measurements are taken after 10 minutes at 120 ℃ with 5 mL/min H_2 and 10 mL/min Ar flow.

4.3 Conclusion and Future Directions

This is a very fascinating area of research because of the reasons stated in the introduction part of this chapter. Being able to see hydrogen diffusion optically

is unique to VO_2 and further investigation of hydrogenation may have significant impact on our understanding of hydrogenation of materials. Another fascinating aspect of hydrogen doping is it acts as a control knob for strong correlations as stated before. Mastering such a degree of freedom may result in better understanding the MIT and realization of applications proposed.

Studies presented here are not capable of drawing a complete picture about hydrogenation of VO_2, however, still we have clarified its new aspects. For instance one of our new results is the fact that there are several mechanisms that control the propagation of hydrogen inside the VO_2 crystal. More experiments are needed to elucidate this new phenomenon. For instance, a careful measurement of formation of stripes with doping temperature can provide how fast this segregating process takes place. Also an observation of long time evolution of the stripes is needed to understand how much this mechanism effects hydrogenated samples at room temperature. Another experiment would be the measurement of Raman active optical phonon modes that emerge due to hydrogen in the VO_2 crystal. We have done some preliminary measurements but failed to locate any modes due to equipment inadequacies. Measurement of these modes would provide useful information about how hydrogen interacts with the ions in the crystal. Electronic transport measurements can also provide invaluable information. For instance multi-contact measurement of resistivity can provide a more accurate way to measure hydrogen diffusion along the nanobeam. In-*situ* measurements during hydrogenation can lead to measurement of hydrogenation rate and hydrogen amount inside the crystal. Electromigration of hydrogen can also be studied with such a system. Also effects of electric and magnetic field on the metallic stripes can lead to new information.

Other than fundamental interest, immediate applications of hydrogenation is apparent. For instance a hydrogen sensor made of VO_2 films may have extreme sensitivity and selectivity to hydrogen gas. Also from our experiments, devices

can survive and can be hydrogenated over months waiting under ambient conditions. Another application can be hydrogen sensing in organic environments. Free protons in the organic solutions can be detected by electrical resistivity measurements. Further investigation will reveal new and novel applications.

Appendices

Appendix A

VO_2 Nanocrystal Growth

We grow single crystal VO_2 nanobeams and nanoplates using slightly modified version of Guiton *et al.*'s [2] physical vapor deposition (PVD) method. Here we discuss the details of the growth setup, the techniques and the parameters that we use to grow VO_2 nanocrystals on various substrates.

A.1 Growth Setup

We use a fairly simple growth setup. A quartz tube with vacuum and gas feed flanges placed inside a Lindberg/Blue M TF55035A-1 tube furnace that can go up to 1100 ℃. Temperature is constant within 10 cm from the center of the furnace and decreases quadratically towards the edges. Argon and oxygen gases are connected to the quartz tube with copper tubing from one end with a fixed flange, and to an Edwards 12 vacuum oil pump from the other end with a high vacuum hose. Flow meters from the gas cylinders allow us to control the amount of gas passing per unit time and a pressure gauge and a control valve allows us to control and measure the pressure inside the tube. A schematic of the setup is depicted in Figure A.1(a). We place the source crucible and the substrate in a secondary, smaller diameter quartz tube and slide that tube in to the outer

tube by removing the hinged clamp connecting the high vacuum hose from the vacuum pump to the flange on the outer quartz tube (not shown in the figure). This allows us to change inner tube with ease as it accumulates source material on the walls,which helps to keep the outer tube clean and minimizes the growth to growth variations due to accumulation of excess material on the walls of the quartz tube.

The relevant dimensions of the setup is given in the caption of the Figure A.1(b).

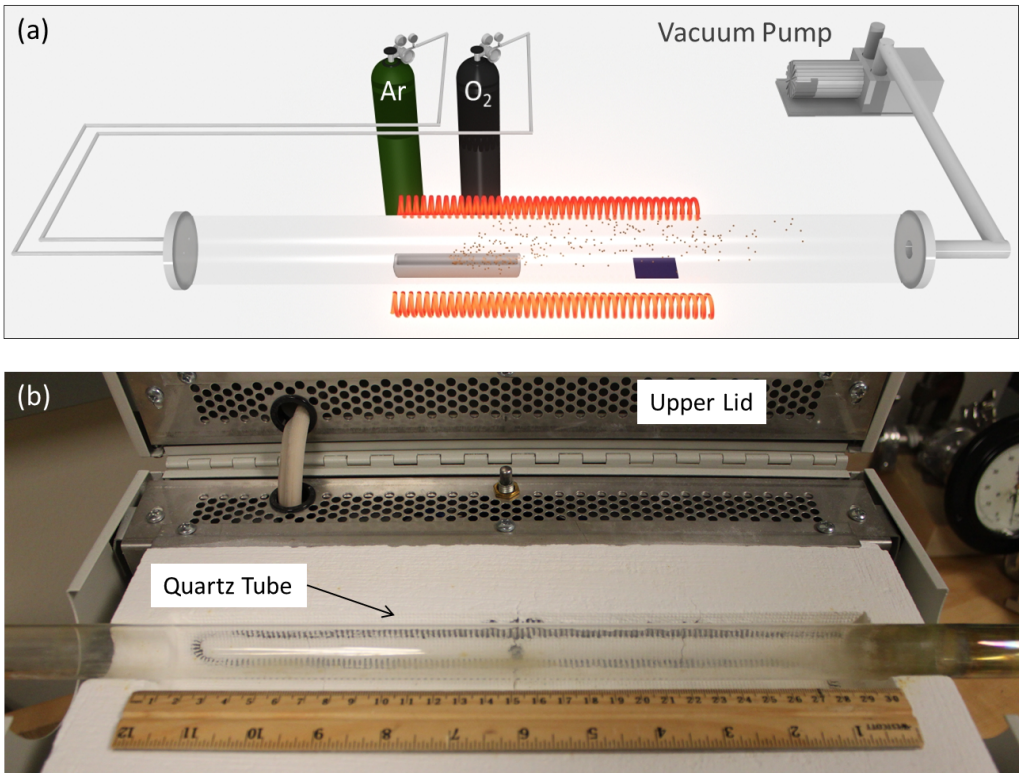

Figure A.1: **Growth setup** (a) A schematic of the growth setup. The source crucible and the substrate is placed in to the center of the tube furnace few centimeters apart. Red coils denote the hot zone of the furnace where temperatures can reach up to 1100 ℃. Vacuum pump evacuates the quartz tube and argon and oxygen gases are flown through the tube.(b)Picture of the furnace with upper lid open. Length of the ruler is 30 cm. Diameter of the outer tube is 2.5 cm and the inner tube is 1.8 cm. Total length of the outer tube without flanges is 78 cm.

A.2 Growth Parameters and Procedures

Although we have a good understanding about the parameters that are involved in the growth process, we are far from having a complete control over the growths. Over the course of 3 years we collected all parameters that might be relevant to the crystal growth in a database. In this section we are going to discuss the growth parameters and their effects on the growth of the crystals depending on the trends in the growth database and the literature.

A.2.1 Growth Parameters

Source Material

Although the original method [2] is a PVD, we (not published) and other groups [122, 123] realized that using V_2O_5 powder promotes the growth of VO_2 under certain conditions. We put tens of milligrams of V_2O_5 powder from Alfa Aesar® into an alumina crucible from Almath, 5 cm long 0.5 cm wide and 1 cm tall. We use same crucible over many growths. Using new crucible shows no significant difference than the multiple times used one in terms of grown crystals, however a layer of black crystal chunk covers the surface of the crucible that can be scratched off to some extend.

Vacuum and Ar Flow Rate

Vacuum control is crucial for the success of the growth process since even small amounts of oxygen in the system can alter the oxidation state of the source or intermediate states at elevated temperatures, which may result in growth of undesired stoichiometries. Thus leaks in the system must be checked throughly and fixed. We perform crystals growth under few mbar when there is no argon gas flowing. Typical vacuum leak for our setup is around 1 mbar/hr.

Argon gas is used as carrier for the vanadium compound vapor from the source

crucible to the substrate. Flow rate should be adjusted such that the vapor can land onto substrate without leaving the chamber. However exact dynamics of that process is unknown to us although some insight can be gained by examining the dynamics of the growth with source placed onto substrate as studied by Strelcov *et al.* [122]. Argon flow rate is kept around 0.42 l/min which raises the tube pressure to 10 mbar.

Temperature and Growth Duration

Growths can be performed at different temperatures with different growth durations. As shown in Figure A.2 during the growth as temperature changes the source material goes through different oxidation states. Although the typical growth temperature we use is 950 ℃, growths can be performed at temperatures ranging from 850-1000 ℃.

Growth duration is another crucial parameter that determines the shape and size of the crystals. If the duration is too short, under-grown crystals will be dominant. If the duration is too long, then over-growth over the sample will be observed. Typical growth duration ranges from 3 to 15 minutes.

Source Crucible and Substrate Positions

As mentioned before temperature profile inside the furnace is almost constant over a region of 20 cm. To utilize the hot region most, we place the source crucible 2.5 cm to the left of the center and the substrate to few centimeters to the right. Although there are some clues about the combined effect of the argon flow and the substrate position, it is hard to isolate sole effect of position dependence of the growth since the effect of surface preparation of the substrate plays a big role but it can only controlled to some extend. Yet under idealized conditions, substrate within a centimeter of the source usually results in thick plates, 1 to 7 cm may result in plates or wires, and beyond 10 cm usually results

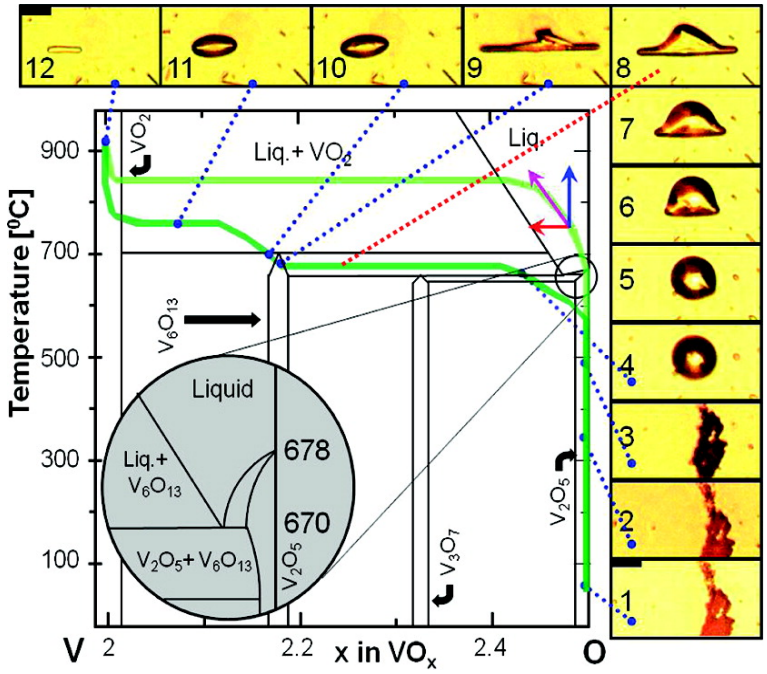

Figure A.2: Figure from Strelcov *et. al.* [122] showing the stages of growth based on the data from [124] and [125]. Optical images shows the transformation of source material as the growth proceeds. V_2O_5 powder turns darker as temperature increases as a result of chemical reduction. Then the powder melts around 670 ℃, and forms small droplets (picture 4). Intermediate V_6O_{13} crystalline nanowires start nucleating after melting by consuming the liquid (picture 5-9). Around 710 ℃, the V_6O_{13} crystalline melts (picture 10) and VO_2 crystals start forming (picture 10-12). The dark and light green lines show the evolution of the system described as motion of the figurative point along two distinct trajectories.

in incomplete growth since temperature does not get high enough to form VO_2 crystals.

Surface Preparation of the Substrate and Catalysts

Type of the crystals grown depends heavily on the properties of the substrate surface. Most of the crystals are grown on silicon substrate covered with SiO_2. Depending on the device needs wafer with either 500 nm or 2 µm oxide is used. However no study has been done on the effect of the thickness of oxide layer on the growth and we haven't seen any direct relation between growth type and density with the oxide thickness. Typical surface preparation involves ace-

tone, isopropyl alcohol(IPA), distilled(DI) water rinse and nitrogen gas drying, respectively. However, almost any substrate prepared this way yields different, irreproducible growth even though all the parameters are kept the same. It is most likely that organic chemicals have a catalytic effect on the growth and slight difference in the cleaning process leads to dramatic changes (will be discussed in growth parameters in detail).

Another growth type is epitaxial growth on single crystal substrates. One of the most suitable substrate for the epitaxial growth is TiO_2, which has the same crystal structure as the high temperature rutile VO_2. In this growth type, surface de-oxidation of TiO_2 must be controlled in order to get the right stoichiometry for VO_2. Details of this growth method is discussed in next subsection A.2.2.

Catalysts play an extremely important role in the growth. For instance stamping textured finger-tip of purple nitrile powder-free gloves by Kimberly-Clark promotes crystal growth dramatically. However, the chemicals involved in the catalyzation using nitrile glove is unknown to us.

A.2.2 Growth Procedures

Depending on the type of crystals that are intended to grow and the substrate type, growth parameters and substrate preparation varies. Here I list the details of how to grow each crystal type.

Sparse, tens of microns long VO_2 nanowire growth

Growth of crystals start from certain "fuel" stations as shown in figure A.2 and nanowires crystallize from these stations. In PVD growth density of the fuel stations in a region on the substrate are determined by several factors such as density of catalyzers in that region, duration of growth, temperature, flow rate etc. To grow sparse long nanowires, tap the surface of dried substrate very lightly with Kimberly-Clark purple nitrile powder-free glow after cleaning the substrate

with acetone-IPA-DI water in this order. A short growth duration is needed to keep the number of fuel stations at a desired level. Typically a growth of 5 minutes at final temperature will be enough to grow long nanowires. Another parameter to control is the Ar flow duration. Flowing Ar beginning from the warm up cycle will result in too much source deposition. So Ar should only be flown during the growth duration at final temperature. Source amount doesn't matter much to our experience and something between 10-50 mg will be enough. After growth we usually perform a rapid cooling and stop the Ar flow immediately after the specified growth duration which helps to stop growth while the oven is cooling down. Before removing the sample, oven should cool down to at least 300 ℃ in order to prevent excessive surface oxidation.

Plate growth

Growing plates is easier than growing nanowires most of the time. Preparation of substrate will be same as nanowire growth except that glove print stamping should be with a little more pressure on the substrate. Again, over pressing the glove will result in extremely dense growth. Growth time should be a little bit longer than 5 minutes, too. Except than these, other procedures are the same as nanowire growth.

Epitaxial growth on single crystal rutile substrates

Using PVD method for epitaxial growth is a very cheap way of getting epitaxial films of VO_2 compared to pulsed laser deposition or molecular beam epitaxy methods. However, we had no chance of comparing the quality of the films grown by PVD method to other more advanced methods. To grow epitaxial films, one need to carefully control the surface de-oxidation of the target substrate. The problem is as the temperature inside the furnace increases toward the growth temperature, surface of the oxide substrate, i.e. TiO_2 reduces by loosing oxygen.

Thus, during ramp up oxygen gas needs to be flown into the chamber. Typically a rate of 0.25 l/min is enough. Once the growth temperature is reached, oxygen gas must be turned off and Ar gas needs to be flown. Duration of the growth is usually limited to several minutes, however if one needs thicker films it can be extended. Typically no surface preparation is necessary for gowth on TiO_2. This growth method requires experience with PVD growth. The problem is TiO_2 is very expensive and adjusting the growth parameters require extensive experience with the current state of the furnace(calibration of thermocouple, leak rates, source etc.).

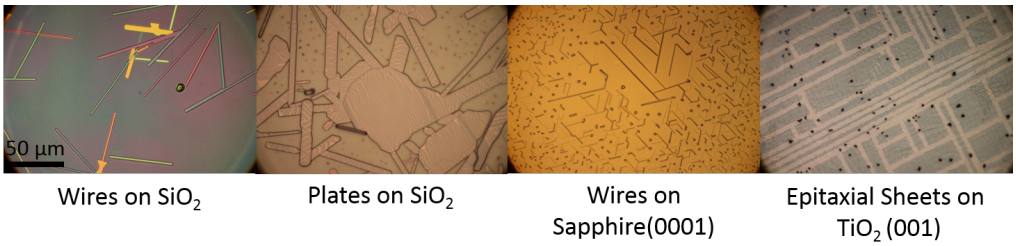

Figure A.3: Different VO_2 crystal types.

A.2.3 Concluding remarks on growth procedures

From a physicist's perspective crystal growth is more art than science. There are many parameters that can have effect on the growth and the phase space that those parameters form is usually very complicated to tackle for someone whose aim is to study the crystal itself rather than how it grows. However, this does't mean that one needs to do arbitrary things to get crystals. There are few golden rules to follow.

- As for most growths, VO_2 growth is very sensitive to air leaks into the growth tube. Both oxygen and nitrogen have adverse effects on the growth.
- Substrate preparation is very important. Usually organic compounds have dramatic effect on the growth.

- In PVD growth, temperature needs to be high enough to have a volatile constituents from the source and these constituents need to be translated toward the substrate which needs to be at right temperature to form the desired crystals. If the substrate is not in the correct temperature zone, you won't be able to grow the desired crystal.
- Gas flow is important in PVD method, however excessive flow may result in washing the constituents that for the crystal.
- Usually the quartz tube used for the growth gives hints about the growth. By investigating tube it is possible to understand how growth went.
- Last but not least, in crystal growth never jump to conclusion, or take action after you see something once!

Appendix B

Device Fabrication Techniques

In this appendix I discuss the details of device fabrication techniques used in the experiments presented in this thesis. Sections in this appendix describe the devices in each experiment and their ordering follow the chapter ordering.

B.1 Suspended Nanobeam Devices for Photocurrent Studies

As described in the main text when VO_2 is grown on the SiO_2 surface, adhesion to substrate causes non-uniform strain on the nanobeam. This leads to complicated domain patterns [100] and makes it difficult to study different phases. However, an ingenious design by Wei *et al.*[26] relieves the non-uniform strain by suspending the nanobeam across the gold contacts which only leaves a uniform stress along the pseudo-rutile c-axis of the nanobeam. The constraint on the distance between two contacts manifests it self as when the temperature goes above the transition temperature T_c, some portion of the beam turns into metallic phase and the other part stays insulating. Given the fixed gap length L above the T_c, nucleation of the metallic domain decreases the natural length of the beam since the metallic phase has shorter lattice constant along the pseudo-rutile c-axis. As

metallic domain size grows with the increasing temperature stress is adjusted so that two phases coexists.

In our scanning photocurrent experiments we used devices similar to Wei *et. al.* paper. Scanning electron microscope images are shown in FigureB.2(b). Both images are taken at room temperature with upper panel showing a typical unbuckled device whereas lower panel is showing a buckled one. The distance between the contacts varies for the devices we used in the SPCM studies. Depending on the contact separation, device characteristics also changes. For instance, devices with contact separations greater than 20 m we observe I_{M1}I-$_{M2}$ coexistence below T_c. Also, as expected these devices show buckling.

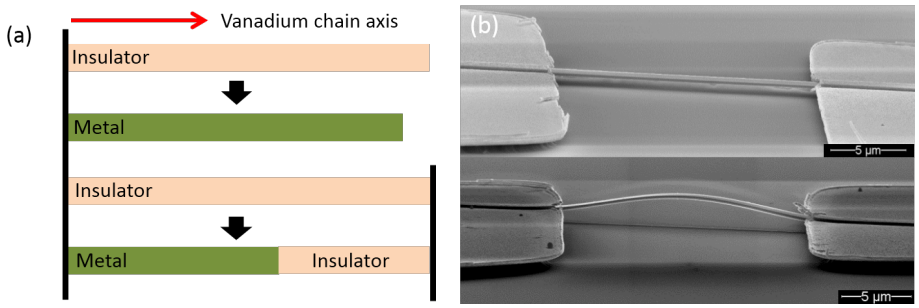

Figure B.1: **Suspended Nanobeam Devices** (a) Comparison between cantilevered nanobeam (upper) and doubly clamped suspended VO_2 nanobeam (lower) before and after the phase transition indicated by down arrows. Vanadium chain axis(pseudo-rutile c-axis) denoted by an horizontal arrow. When the nanobeam is fixed on both ends it is energetically more favorable to go into coexistence.(b) SEM micrographs of two suspended nanobeam devices at room temperature. The image on the lower panel shows a buckled beam.

B.1.1 Device Fabrication and Typical Issues Encountered

Device fabrication starts with preferably more than 30 µm long and about 2 µm wide nanobeams grown on Si chip with 2 µm thick oxide layer. Long wires ensure better clamping while thick oxide makes sure that once the oxide layer is removed in order to suspend the nanobeam later in the fabrication, contacts won't short via Si substrate. A schematic of device fabrication steps in shown in Figure

B.2(a). Using optical lithography, we locate suitable nanobeams and write the contact pad patterns. Heidelberg µPG mask writer is used for that purpose since locating wires is simple with the built in camera. For all of the devices that we measured, we used Az1512 photoresist for patterning the contacts. After writing the pattern, resist is developed and the chip is rinsed throughly. In some samples we used oxygen plasma to clean off the any residue from the resist, however no significant difference is observed between well exposed and developed devices and plasma cleaned devices. Then using e-beam evaporator, 100 to 300 nm of gold is evaporated following 5 to 10 nm of titanium as wetting layer for gold. During the evaporation of gold, rotation of the sample holder of the e-beam evaporator is crucial since if the holder is stationary gold doesn't cover the sides of the nanobeam leading to a poor clamping of the wire. After the evaporation excess metal is removed by dissolving the resist layer under the gold. As the resist dissolves in acetone, only the metal on the patterned regions stays while the rest lifts off. Usually hot acetone bath (60 ℃) is used in order to speed up the lift off process. In some cases short bursts of sonication is needed to remove metal in certain areas. Final step is etching the oxide layer, which leaves the nanobeam suspended and completes the fabrication of the device. We used buffered oxide etchant(BOE), a mixture of HF (hydrofluoric acid), NH_4F and H_20. Typically 80 nm/min etch rate is achieved by 1 part 48% HF and 6 parts of 40% NH_4F mixture BOE. Devices are etched about 8 minutes to suspend typical beams. Longer etch time is required for wider beams. After etching we optically investigate the beams for obvious defects that are mentioned below. Then $R-T$ characteristics of the ones with no obvious defects are studied from room temperature up to point where it is completely metallic. If the device is stable after few cycles and the $R-T$ curves show no change over the cycles, then devices are used in SPCM study.

Figure B.2(b) shows SEM images of devices with typical problems. Upper panel

shows a device with inadequate gold evaporated. Also the sample holder of the evaporator was stationary. As a result BOE gets underneath the beam and after one cycle above the T_c due to stress on the beam gold contact can no longer hold the beam down. Another problem is over etching the oxide layer, exemplified in the middle panel. BOE gets beneath the nanobeam from the sides and the front and carves out the oxide supporting the nanobeam. Thus, beam fells down off the metal leaving no or bad contact. Final common example is underetched devices as shown in the lower panel. Unetched SiO_2 causes non-uniform strain on the beam which is not desired in our devices.

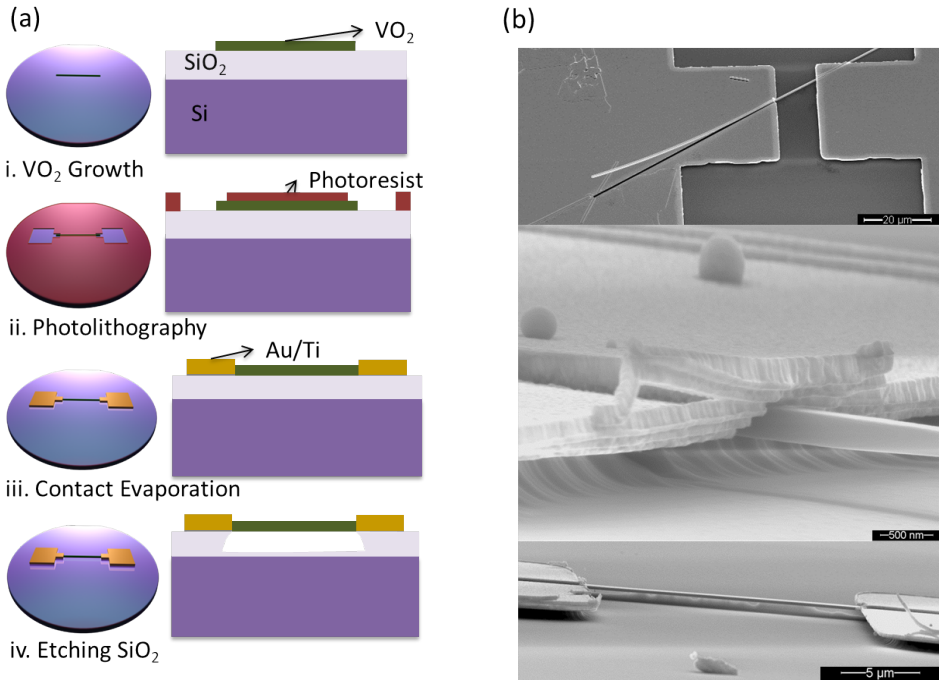

Figure B.2: **Fabrication of Suspended Nanobeam Devices** (a) Fabrication steps from growth of VO_2 nanobeams on oxidized Si chip to etching the oxide layer. Details of the steps are described in the text.(b) SEM micrographs of bad devices. Details are explained in the text.

B.2 Cantilevered VO_2 Beams for Hydrogen Doping

As it is mentioned in chapter 4 due to extreme anisotropy of hydrogen diffusion in VO_2 crystal, covering the facets leading to the rutile c-axis with Pd is important for avoiding any complications that might arise in the experiments due to off c-axis non-uniform hydrogen density. However as shown in Figure B.3 when Pd is evaporated straight from above or even with a very steep angle, only the upper parts of the end facets are covered with Pd. Figure B.3(a)-(b) shows top and bottom side of a nanoplate respectively. Comparison of these two images clearly shows that only a fraction along the thickness of the nanoplate end is covered with Pd, thus the bottom portion has a different hydrogenation pattern. To avoid that problem we fabricated cantilevered beam devices.

After loosening PVD grown nanobeams in buffered oxide etchant(BOE) for

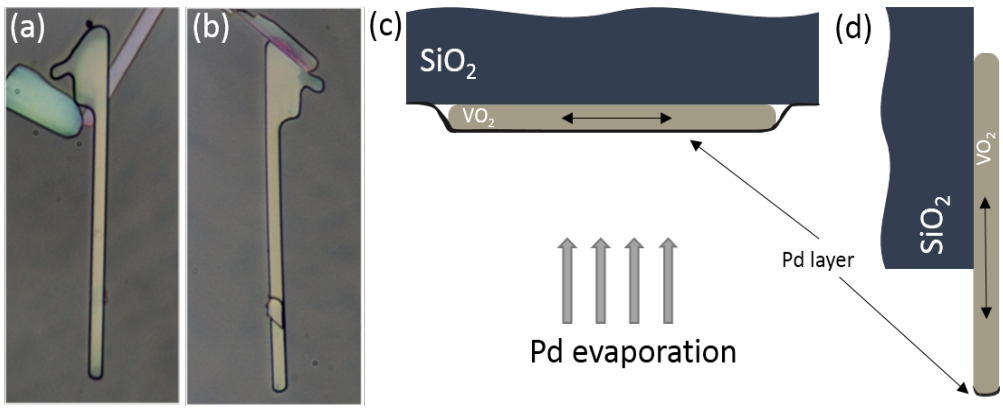

Figure B.3: **Importance of Sample Orientation** Top, side where Pd evaporation performed, and bottom side of the same nanoplate is shown in (a)-(b) respectively. (c) and (d) are cartoon showing the Pd accumulation on VO_2 depending on the orientation of the crystal.

couple of seconds, using a sharp tip attached to a Marzhauser Tango nanomanipulator, nanobeams are transfered onto side of either a Si chip or a PDMS coated Si chip. Transfer process takes a lot of practice and a good technique. It is easier to pick wires from the sides of the growth chips. Electrostatics can also be used to pick up the nanobeams. Care taken to ensure that the transferred sides of

the substrates are not rough or uneven. Although the transferred nanobeams go through BOE cleaning before the transfer, transfer process often introduces debris onto nanobeams. Also any oxide layer left on the VO_2 nanobeams may have adverse affect on hydrogenation. Due to these reasons a second BOE cleaning is necessary, yet without any fixture to the transferred substrate, BOE washes away the nanobeams. Thus nanobeams are fixed with a UV curable epoxy. A droplet of Norman Electronic Epoxy 121, is picked up with a very sharp glass needle and placed very close to the nanobeam without touching the nanobeam to avoid sticking to glass needle. As the needle raised, due to surface tension droplet starts spreading and when the needle losses contact with the epoxy, epoxy rushes to the nanobeam and partially covers it. A few minutes under UV lamp hardens the epoxy leaving the beam fixed. It is a good idea to check the side of nanobeam faces toward substrate since in some rare cases epoxy covers the cantilevered region. After fixing the beams, second BOE cleaning is performed and without any delay, chips are placed in to e-beam evaporator with free end of the cantilevered beams facing to the source crucible. Thickness of evaporated Pd seems to matter although we haven't done a detailed study to back-up this observation. Usually thickness of around 2 nm works best and for films around 10 nm fails to catalyze hydrogen gas as efficient.

For transport measurements and electromigration studies, indium contacts are placed on part of the beam on the substrate.

B.3 Suspended VO_2 Beams for Strain Measurements

The chips used for the strain measurements are micromachined from silicon chip with 500nm thermal oxide using deep-reactive ion etching technique at Santa Barbara nanofabrication facility at a cost. A four-inch wafer is patterned with photolithography and 20 or 40 µm gaps are etched through the whole thickness. Once we receive the chips, surface coating is resolved by acetone and some of

the chips are evaporated with gold via a shadow mask. Then nanobeams are transferred across the gap in a similar way as described in the previous section for cantilevered beams. The only difference here is the nanobeam is glued down from both ends and some of the are contacted with indium to shadow evaporated gold contacts.

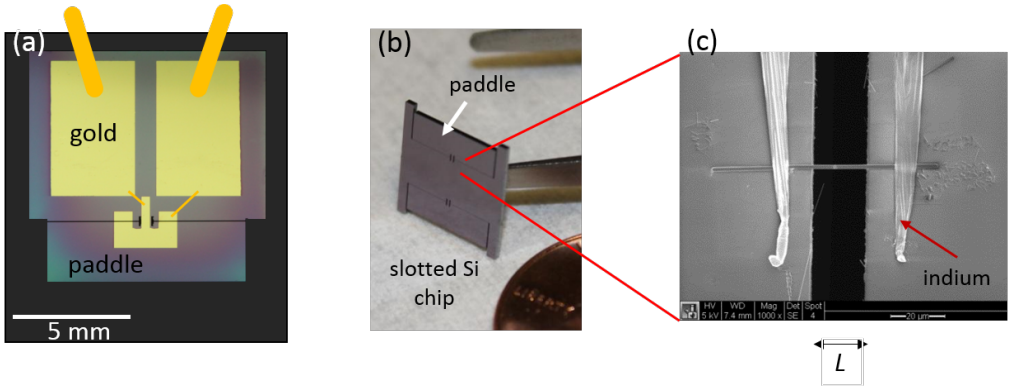

Figure B.4: **Device for Strain Measurements** (a) A device with gold pads is shown.(b) A two paddled design is shown.(c) An SEM image of a nanobeam contacted by indium and glued down, ready for measurements.

Since the paddle part is held in place by a tiny fixture, strain chips are very fragile. In every step of device fabrication care must be taken to protect the device. Even closing the lid of a container may break the paddle. Never grab the chips from the paddle part. Also, once the beam is transferred across the slot extra attention needs to be payed since if the gap opening changes more than several microns nanobeam may be broken.

Appendix C

Nano-Scale Object Strain Setup

The strain setup consists of several different components. First component is the temperature stage which holds the chip in place with a precisely machined slot. 1 cm by 1 cm slot recessed by half a millimeter provides a firm encapsulation to the body of the micro-machined chip. Two notches carved to the sides for easy removal of the chip from the slot. Additional holes are drilled on the temperature stage to decrease the thermal mass of the stage. There are two PT-100 sensors one buried in the stage and the other is mounted with high thermal conductivity epoxy on the top surface of the stage close to the chip measures the temperature. 4-wire measurement technique is used to minimize the offset in temperature that might be caused by the cabling to the temperature controller. Temperature measurement and closed-loop control is performed with a Lakeshore 325 temperature controller. The piece that holds the temperature stage also holds a PCB board with metal pins sticking down both clamps the chip down and also makes the electrical contact for electronic transport measurements. A small piece from the side of the temperature stage is removed to allow laser beam reflection from the side of the chip's paddle part. Second major component is the laser detection system. A laser diode through a pinhole is passed through a beam splitter travels through a hollow glass tube to the side of the paddle. The glass tube has

an important function in eliminating the noise caused by deflection of the laser due to warm air currents near the temperature stage. After reflection from the paddle, beam splitter diverts part of the laser beam to a position sensitive detector(PSD) from OSI optoelectronics, duolateral PSD SL-5. Depending on how much the laser deflects a comparator circuit determines the relative change in the distance. Laser beam is pulsed at 500 Hz and a software lock-in method is used to filter out the noise. Finally the pizeoelectric stage from PI (Model P-611.10) with a probe mounted on top pushes the paddle. The piezo stage is connected to a remotely controllable power supply. All the electronic components are connected to a DAQ card from National Instruments. Readings from the DAQ card is processed with a custom made LabView program. Also whole setup is mounted on a high magnification microscope equipped with linear polarizer and a Canon T3i camera. Camera image is calibrated with an AFM calibration standard for length measurements on the image. Based on these measurements a screen pixel reading program, MB ruler, is used to measure lengths on the image. These measurements are correlated with the temperature and gap change measurements. Whole setup is enclosed with a grounded aluminum foil coated cover to shield interference and air currents which affects the precision of the measurements during the experiments.

Appendix D

Hydrogen Doping Setup

For hydrogenation a controlled environment is important. A vacuum chamber with temperature control is desired for creating this controlled hydrogenation environment. The chamber we built for hydrogenation is capable of providing this environment. Sample temperature can be controlled from -40 to 200 ℃ and a less than a mTorr vacuum can be achieved. Also the chamber is integrated with microscope and it can be modified to have a window for in-*situ* optical measurements as well as electrical vacuum feed-through for electronic transport measurements. System can be controlled via a LabView program.

Chamber and the lid is machined out of 6061 aluminum alloy. Total thickness of the chamber is kept below 2.5 cm to make it compatible with most long-working distance microscopes. Gas inlets and vacuum pump outlet are copper tubes fitted into the aluminum chamber and fixed by Varian Torr Seal. Before connecting the copper tube to the chamber, both contact surface are cleaned throughly. Torr Seal is an excellent low vapor pressure epoxy and works very well under low temperatures. Temperature of the sample is controlled with a Peltier plate specifically designed for high temperatures from Custom Thermoelectric(Part number= 03111-9L31-0600). The Peltier plate is fixed on to a copper cooling stage for water cooling with an thermally conductive epoxy, Omega Bond-200

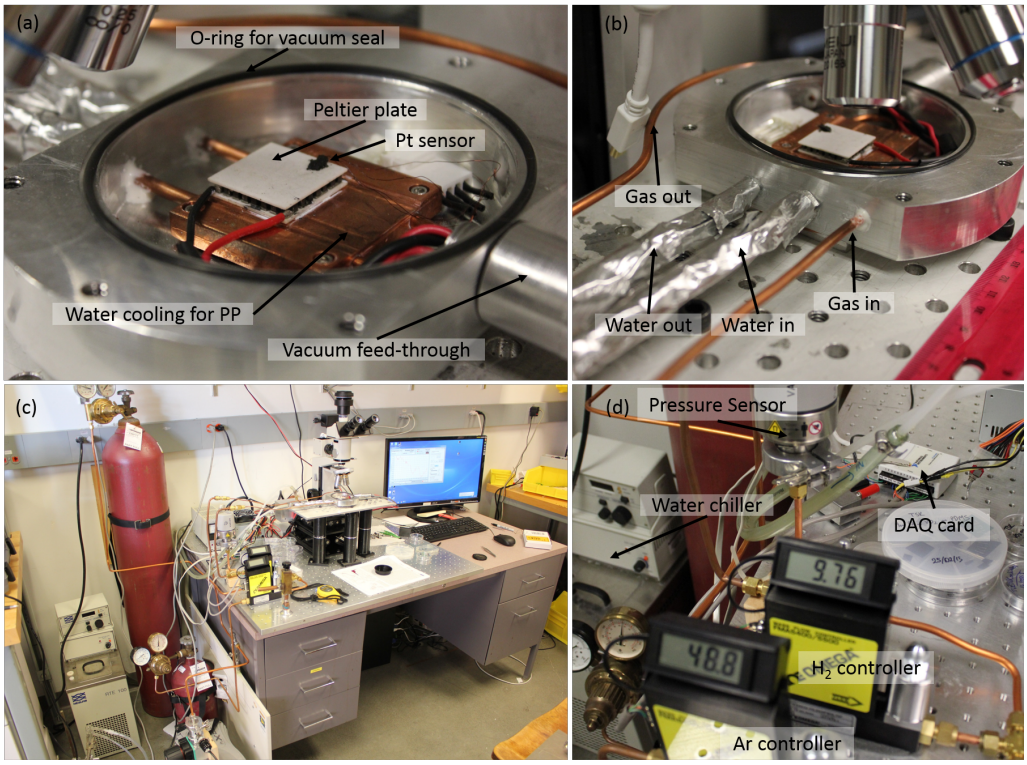

Figure D.1: **Hydrogen doping setup** (a)Close-up view of the chamber. Essential components are marked on the image. Viton o-ring from Marco Rubber is used to seal the chamber with when aluminum lid is closed. Peltier plate(PP) is fixed down with a high thermal conductivity epoxy. Pt-100 temperature sensor attached to 4-wires is glued onto the stage with very high thermal conductive epoxy. Water cooling base is essentially a copper heat exchanger to dissipate excess heat during cooling operation of the Peltier plate. Cable connections to the PP and the temperature sensor is made through a vacuum feed-through from Fischer scientific. Multiple pins of the feed-through is used to separate the maximum 4 ampere current. (b)Gas and water ins and outs. (c) General view of the setup. Water chiller, gas tanks, vacuum pump, on the ground and the setup and the computer controls are on the table. There is an optical table to dampen the vibrations. (d) Close-up view of the flow controllers, the pressure sensor and the daq card with the water chiller on the background.

durable at high temperatures. A PT-100 platinum sensor is also attached to the top surface of the Peltier plate using the same epoxy. Since Peltier plates require high currents for operation we used a current source connected to a Lakeshore 340 temperature controller. This allowed us to achieve temperature stability at desired temperature on the order of mK when the chamber is closed. Ar and H_2

gas flow rates are controlled using Omega FMA5414 flow controller and meters calibrated for the gases used. Two pressure sensors, one before the chamber, other before the pump used. All the electronics are interfaced with a DAQ card to a computer and controlled by a LabView program. We designed and wrote the program which allows users to control the setup, perform automated hydrogenation and track changes in the system parameters. Moreover microscope integration allows simple visual inspection at them moment but improvements on the optics will allow more detailed studies.

Bibliography

[1] Morin, F. J. Oxides which show a metal-to-insulator transition at the Neel temperature. *Phys. Rev. Lett.* **3**, 34–36 (1959). URL http://link.aps.org/doi/10.1103/PhysRevLett.3.34. [cited at p. iv, 2]

[2] Guiton, B. S., Gu, Q., Prieto, A. L., Gudiksen, M. S. & Park, H. Single-crystalline vanadium dioxide nanowires with rectangular cross sections. *Journal of the American Chemical Society* **127**, 498–499 (2005). URL http://pubs.acs.org/doi/abs/10.1021/ja045976g. http://pubs.acs.org/doi/pdf/10.1021/ja045976g. [cited at p. iv, 3, 14, 67, 69]

[3] Kasirga, T. S. *et al.* Photoresponse of a strongly correlated material determined by scanning photocurrent microscopy. *Nature Nano.* **7**, 723–727 (2012). URL http://dx.doi.org/10.1038/nnano.2012.176. [cited at p. v, 10, 14, 16]

[4] Baibich, M. N. *et al.* Giant magnetoresistance of (001)Fe/(001)Cr magnetic superlattices. *Phys. Rev. Lett.* **61**, 2472–2475 (1988). URL http://link.aps.org/doi/10.1103/PhysRevLett.61.2472. [cited at p. 1]

[5] Si, Q. & Steglich, F. Heavy fermions and quantum phase transitions. *Science* **329**, 1161–1166 (2010). URL http://www.sciencemag.org/content/329/5996/1161.abstract. http://www.sciencemag.org/content/329/5996/1161.full.pdf. [cited at p. 1]

[6] Mott, N. F. & Pierels, R. Discussion of the paper by de Boew and Verwey. *Proc. Phys. Soc.* **49** (1937). [cited at p. 1]

[7] Bednorz, J. & Mller, K. Possible high T_C superconductivity in the Ba-La-Cu-O system. *Z. Phys. B* **64** (1986). [cited at p. 2]

[8] Leggett, A. J. What do we know about high T_C. *Nature Phys.* **2** (2006). [cited at p. 2]

[9] Oh, D.-W., Ko, C., Ramanathan, S. & Cahill, D. Thermal conductivity and dynamic heat capacity across the metal-insulator transition in thin film VO_2. *App. Phys. Lett.* **96**, 151906 (2010). [cited at p. 2, 7, 9, 28]

[10] Cao, J., Fan, W., Zheng, H. & Wu, J. Thermoelectric effect across the metal-insulator domain walls in VO_2 microbeams. *Nano Letters* **9**, 4001 (2009). URL http://dx.doi.org/10.1021/nl902167b. 10.1021/nl902167b. [cited at p. 3, 9, 25]

[11] Berglund, C. & Guggenheim, H. Electronic properties of VO_2 near the semiconductor-metal transition. *Physical Review* **185**, 1022–1033 (1969). URL

http://dx.doi.org/10.1103/physrev.185.1022. 10.1103/physrev.185.1022. [cited at p. iii, 3, 6, 7, 8, 9, 14, 25, 46]

[12] Qazilbash, M. M. *et al.* Mott transition in VO_2 revealed by infrared spectroscopy and nano-imaging. *Science* **318**, 1750–1753 (2007). URL http://www.sciencemag.org/content/318/5857/1750.abstract. http://www.sciencemag.org/content/318/5857/1750.full.pdf. [cited at p. 3, 14]

[13] Kawakubo, T. & Nakagawa, T. Phase transition in VO_2. *J. of the Phys. Soc. of Japan* **19**, 517–519 (1964). [cited at p. 3]

[14] Zylbersztejn, A. & Mott, N. F. Metal-insulator transition in vanadium dioxide. *Phys. Rev. B* **11**, 4383–4395 (1975). URL http://link.aps.org/doi/10.1103/PhysRevB.11.4383. [cited at p. 3, 9]

[15] Rice, T. M., Launois, H. & Pouget, J. P. Comment on "VO_2: Peierls or mott-hubbard? a view from band theory". *Phys. Rev. Lett.* **73**, 3042–3042 (1994). URL http://link.aps.org/doi/10.1103/PhysRevLett.73.3042. [cited at p. 3]

[16] Biermann, S., Poteryaev, A., Lichtenstein, A. I. & Georges, A. Dynamical singlets and correlation-assisted peierls transition in VO_2. *Phys. Rev. Lett.* **94**, 026404 (2005). URL http://link.aps.org/doi/10.1103/PhysRevLett.94.026404. [cited at p. 3, 12, 13]

[17] Eyert, V. VO_2: A novel view from band theory. *Phys. Rev. Lett.* **107**, 016401 (2011). URL http://link.aps.org/doi/10.1103/PhysRevLett.107.016401. [cited at p. 3]

[18] Fillingham, P. J. Domain structure and twinning in crystals of vanadium dioxide. *Journal of Applied Physics* **38**, 4823–4829 (1967). URL http://link.aip.org/link/?JAP/38/4823/1. [cited at p. 3, 14]

[19] Cox, P. *Transition metal oxide* (1992). [cited at p. 3]

[20] F., C., Luryi, S. & Spivak, B. Switching device based on first-order metal-insulator transition induced by external electric field. *Future Trands in Microelectronics: the Nano Millenium* (2002). [cited at p. 4]

[21] Driscoll, T. *et al.* Dynamic tuning of an infrared hybrid-metamaterial resonance using vanadium dioxide. *Applied Physics Letters* **93**, 024101 (2008). URL http://link.aip.org/link/?APL/93/024101/1. [cited at p. 4, 18]

[22] Verleur, H. W., Barker, A. S. & Berglund, C. N. Optical properties of VO_2 between 0.25 and 5 eV. *Phys. Rev.* **172**, 788–798 (1968). URL http://link.aps.org/doi/10.1103/PhysRev.172.788. [cited at p. 4, 18]

[23] Rua, A., Fernandez, F. E. & Sepulveda, N. Bending in VO_2-coated microcantilevers suitable for thermally activated actuators. *Journal of Applied Physics* **107**, 074506 (2010). URL http://link.aip.org/link/?JAP/107/074506/1. [cited at p. 4]

[24] Soltani, M., Chaker, M., Haddad, E. & Kruzelesky, R. V. Thermochromic vanadium dioxide smart coatings grown on kapton substrates by reactive pulsed laser deposition. vol. 24, 612–617 (AVS, 2006). URL http://link.aip.org/link/?JVA/24/612/1. [cited at p. 4]

[25] Kim, B.-J. *et al.* Micrometer x-ray diffraction study of vo$_2$ films: Separation between metal-insulator transition and structural phase transition. *Phys. Rev. B* **77**, 235401 (2008). URL http://link.aps.org/doi/10.1103/PhysRevB.77.235401. [cited at p. 6, 12]

[26] Wei, J., Wang, Z., Wei, C. & Cobden, D. H. New aspects of the metalinsulator transition in single-domain vanadium dioxide nanobeams. *Nature* **4**, 420–422 (2009). [cited at p. 6, 9, 13, 37, 39, 77]

[27] McWhan, D. B., Marezio, M., Remeika, J. P. & Dernier, P. D. X-ray diffraction study of metallic VO_2. *Phys. Rev. B* **10**, 490–495 (1974). URL http://link.aps.org/doi/10.1103/PhysRevB.10.490. [cited at p. 6]

[28] Marezio, M., McWhan, D. B., Remeika, J. P. & Dernier, P. D. Structural aspects of the metal-insulator transitions in Cr-doped VO_2. *Phys. Rev. B* **5**, 2541–2551 (1972). URL http://link.aps.org/doi/10.1103/PhysRevB.5.2541. [cited at p. iii, 6, 7, 10, 11, 39, 49]

[29] Bongers, P. F. Anisotropy of the electrical conductivity of VO_2 single crystals. *Solid State Communications* **3**, 275–277 (1965). [cited at p. 6]

[30] Everhart, C. R. & MacChesney, J. B. Anisotropy in the electrical resistivity of vanadium dioxide single crystals. *Journal of Applied Physics* **39**, 2872–2874 (1968). URL http://scitation.aip.org/content/aip/journal/jap/39/6/10.1063/1.1656687. [cited at p. 6]

[31] Barker, A. S., Verleur, H. W. & Guggenheim, H. J. Infrared optical properties of vanadium dioxide above and below the transition temperature. *Phys. Rev. Lett.* **17**, 1286–1289 (1966). URL http://link.aps.org/doi/10.1103/PhysRevLett.17.1286. [cited at p. 6, 9]

[32] Rosevear, W. H. & Paul, W. Hall effect in VO_2 near the semiconductor-to-metal transition. *Phys. Rev. B* **7**, 2109–2111 (1973). URL http://link.aps.org/doi/10.1103/PhysRevB.7.2109. [cited at p. 6, 9]

[33] Ruzmetov, D., Heiman, D., Claflin, B. B., Narayanamurti, V. & Ramanathan, S. Hall carrier density and magnetoresistance measurements in thin-film vanadium dioxide across the metal-insulator transition. *Phys. Rev. B* **79**, 153107 (2009). URL http://link.aps.org/doi/10.1103/PhysRevB.79.153107. [cited at p. 6, 9]

[34] Chen, C. *et al.* Influence of defects on structural and electrical properties of VO_2 thin films. *Journal of Applied Physics* **110**, – (2011). URL http://scitation.aip.org/content/aip/journal/jap/110/2/10.1063/1.3609084. [cited at p. 6, 9]

[35] Kittiwatanakul, S., Lu, J. & Wolf, S. A. Transport anisotropy of epitaxial VO_2 films near the metal–semiconductor transition. *Applied Physics Express* **4**, 091104 (2011). URL http://apex.jsap.jp/link?APEX/4/091104/. [cited at p. 6, 9]

[36] Eyert, V. The metal-insulator transitions of VO_2: A band theoretical approach. *Annalen der Physik* **11**, 650–704 (2002). [cited at p. iii, 7, 8, 9, 11]

[37] Wei, J., Ji, H., Guo, W., Nevidomskyy, A. & Natelson, D. Hydrogen stabilization of metallic vanadium dioxide in single-crystal nanobeams. *Nature Nanotechnology* **7**, 357–362 (2012). [cited at p. vi, 8, 50, 51, 53]

[38] Park, J. H. *et al.* Measurement of a solid-state triple point at the metal-insulator transition in VO_2. *Nature* **500**, 431–434 (2013). URL http://dx.doi.org/10.1038/nature12425. [cited at p. 8, 10, 11, 13, 14, 33]

[39] Allen, J. E., Perea, D. E., Hemesath, E. R. & Lauhon, L. J. Nonuniform nanowire doping profiles revealed by quantitative scanning photocurrent microscopy. *Advanced Materials* **21**, 3067–3072 (2009). URL http://dx.doi.org/10.1002/adma.200803865. [cited at p. 9, 16]

[40] Cao, J. *et al.* Constant threshold resistivity in the metal-insulator transition of VO_2. *Phys. Rev. B* **82**, 241101 (2010). URL http://link.aps.org/doi/10.1103/PhysRevB.82.241101. [cited at p. 9, 13]

[41] Marini, C. *et al.* Optical properties of $V_{1-x}Cr_xO_2$ compounds under high pressure. *Phys. Rev. B* **77**, 235111 (2008). URL http://link.aps.org/doi/10.1103/PhysRevB.77.235111. [cited at p. iii, 9, 10, 11]

[42] Jones, A. C., Berweger, S., Wei, J., Cobden, D. & Raschke, M. B. Nano-optical investigations of the metalinsulator phase behavior of individual VO_2 microcrystals. *Nano Letters* **10**, 1574–1581 (2010). URL http://pubs.acs.org/doi/abs/10.1021/nl903765h. http://pubs.acs.org/doi/pdf/10.1021/nl903765h. [cited at p. 10]

[43] Atkin, J. M. *et al.* Strain and temperature dependence of the insulating phases of VO_2 near the metal-insulator transition. *Phys. Rev. B* **85**, 020101 (2012). URL http://link.aps.org/doi/10.1103/PhysRevB.85.020101. [cited at p. iii, 10, 11, 12, 34]

[44] Pouget, J. P. *et al.* Dimerization of a linear heisenberg chain in the insulating phases of $V_{1-x}Cr_xO_2$. *Phys. Rev. B* **10**, 1801–1815 (1974). URL http://link.aps.org/doi/10.1103/PhysRevB.10.1801. [cited at p. 10, 11]

[45] Ghedira, M., Chenavas, J. & Marezio, M. Cation disproportionation and pairing in the insulating t phase of $V_{0.985}Al_{0.15}O_2$. *Journal of Physics C: Solid State Physics* **10**, L309 (1977). URL http://stacks.iop.org/0022-3719/10/i=11/a=007. [cited at p. 10]

[46] Pouget, J. P., Launois, H., D'Haenens, J. P., Merenda, P. & Rice, T. M. Electron localization induced by uniaxial stress in pure VO_2. *Phys. Rev. Lett.* **35**, 873–875 (1975). URL http://link.aps.org/doi/10.1103/PhysRevLett.35.873. [cited at p. 10, 34, 36]

[47] Tselev, A. *et al.* Interplay between ferroelastic and metalinsulator phase transitions in strained quasi-two-dimensional vo2 nanoplatelets. *Nano Letters* **10**, 2003–2011 (2010). URL http://pubs.acs.org/doi/abs/10.1021/nl1008794. PMID: 20455527, http://pubs.acs.org/doi/pdf/10.1021/nl1008794. [cited at p. 11]

[48] Tselev, A. *et al.* Symmetry relationship and strain-induced transitions between insulating m1 and m2 and metallic r phases of vanadium dioxide. *Nano Letters* **10**, 4409–4416 (2010). URL http://pubs.acs.org/doi/abs/10.1021/nl1020443. http://pubs.acs.org/doi/pdf/10.1021/nl1020443. [cited at p. 11, 36]

[49] Kawada, I., Kimizuka, N. & Nakahira, M. Crystallographic investigations of the phase transition of VO_2. *Journal of Applied Crystallography* **4**, 343–347 (1971). URL http://dx.doi.org/10.1107/S0021889871007180. [cited at p. 11]

[50] Mitsuishi, T. On the phase transformation of VO_2. *Japanese Journal of Applied Physics* **6**, 1060–1071 (1967). URL http://jjap.jsap.jp/link?JJAP/6/1060/. [cited at p. 11]

[51] Umeda, J., Kusumoto, H., Narita, K. & Yamada, E. Nuclear magnetic resonance in polycrystalline VO_2. *The Journal of Chemical Physics* **42**, 1458–1459 (1965). URL http://scitation.aip.org/content/aip/journal/jcp/42/4/10.1063/1.1696136. [cited at p. 11]

[52] ichi Umeda, J., Ashida, S., Kusumoto, H. & Narita, K. A new phase appearing in metal-semiconductor transition in VO_2. *Journal of the Physical Society of Japan* **21**, 1461–1462 (1966). URL http://jpsj.ipap.jp/link?JPSJ/21/1461/. [cited at p. 11]

[53] Kosuge, K. & Kachi, S. Phase diagram of $Fe_xV_{1-x}O_2$ in the 0¡x¡0.25 region. *Materials Research Bulletin* **11**, 255 – 262 (1976). URL http://www.sciencedirect.com/science/article/pii/0025540876901884. [cited at p. 12]

[54] Cavalleri, A. *et al.* Femtosecond structural dynamics in VO_2 during an ultrafast solid-solid phase transition. *Phys. Rev. Lett.* **87**, 237401 (2001). URL http://link.aps.org/doi/10.1103/PhysRevLett.87.237401. [cited at p. 13]

[55] Cavalleri, A., Dekorsy, T., Chong, H. H. W., Kieffer, J. C. & Schoenlein, R. W. Evidence for a structurally-driven insulator-to-metal transition in VO_2: A view from the ultrafast timescale. *Phys. Rev. B* **70**, 161102 (2004). URL http://link.aps.org/doi/10.1103/PhysRevB.70.161102. [cited at p. 13]

[56] Hilton, D. J. *et al.* Enhanced photosusceptibility near T_C for the light-induced insulator-to-metal phase transition in vanadium dioxide. *Phys. Rev. Lett.* **99**, 226401 (2007). URL http://link.aps.org/doi/10.1103/PhysRevLett.99.226401. [cited at p. 13, 18]

[57] Kübler, C. *et al.* Coherent structural dynamics and electronic correlations during an ultrafast insulator-to-metal phase transition in VO_2. *Phys. Rev. Lett.* **99**, 116401 (2007). URL http://link.aps.org/doi/10.1103/PhysRevLett.99.116401. [cited at p. 13, 18]

[58] Pashkin, A. *et al.* Ultrafast insulator-metal phase transition in VO_2 studied by multiterahertz spectroscopy. *Phys. Rev. B* **83**, 195120 (2011). URL http://link.aps.org/doi/10.1103/PhysRevB.83.195120. [cited at p. 13]

[59] Hada, M., Okimura, K. & Matsuo, J. Photo-induced lattice softening of excited-state VO_2. *Applied Physics Letters* **99**, – (2011). URL http://scitation.aip.org/content/aip/journal/apl/99/5/10.1063/1.3621900. [cited at p. 13]

[60] Cocker, T. L. *et al.* Phase diagram of the ultrafast photoinduced insulator-metal transition in vanadium dioxide. *Phys. Rev. B* **85**, 155120 (2012). URL http://link.aps.org/doi/10.1103/PhysRevB.85.155120. [cited at p. 13]

[61] Cavalleri, A. *et al.* Band-selective measurements of electron dynamics in VO_2 using femtosecond near-edge x-ray absorption. *Phys. Rev. Lett.* **95**, 067405 (2005). URL http://link.aps.org/doi/10.1103/PhysRevLett.95.067405. [cited at p. 13]

[62] Merenda, P. & Sol, N. Vapor phase epitaxy of pure VO_2 and $V_{1-x}Cr_xO_2$. *Journal of Crystal Growth* **40**, 195–199 (1977). [cited at p. 13]

[63] Soltani, M., Chaker, M., Haddad, E., Kruzelecky, R. V. & Nikanpour, D. Optical switching of vanadium dioxide thin films deposited by reactive pulsed laser deposition. *Journal of Vacuum Science and Technology A* **22**, 859–864 (2004). URL http://scitation.aip.org/content/avs/journal/jvsta/22/3/10.1116/1.1722506. [cited at p. 14]

[64] Nagashima, K., Yanagida, T., Tanaka, H. & Kawai, T. Influence of ambient atmosphere on metal-insulator transition of strained vanadium dioxide ultrathin films. *Journal of Applied Physics* **100**, – (2006). URL http://scitation.aip.org/content/aip/journal/jap/100/6/10.1063/1.2345600. [cited at p. 14]

[65] Rampelberg, G. *et al.* Semiconductor-metal transition in thin VO_2 films grown by ozone based atomic layer deposition. *Applied Physics Letters* **98**, – (2011). URL http://scitation.aip.org/content/aip/journal/apl/98/16/10.1063/1.3579195. [cited at p. 14]

[66] Zhang, K. *et al.* Synthesis of VO_2 thin films by atomic layer deposition with temav as precursor. *ECS Transactions* **50**, 175–182 (2013). URL http://ecst.ecsdl.org/content/50/13/175.abstract. http://ecst.ecsdl.org/content/50/13/175.full.pdf+html. [cited at p. 14]

[67] Duchene, J., Terraillon, M. & Pailly, M. R.f. and d.c. reactive sputtering for crystalline and amorphous VO_2 thin film deposition. *Thin Solid Films* **12**, 231 – 234 (1972). URL http://www.sciencedirect.com/science/article/pii/0040609072900818. [cited at p. 14]

[68] Aetukuri, N. B. *et al.* Control of the metal-insulator transition in vanadium dioxide by modifying orbital occupancy. *Nature Physics* **9**, 661 (2013). [cited at p. 14]

[69] Liu, W. *et al.* Role of metal contacts in designing high-performance monolayer n-type WSe_2 field effect transistors. *Nano Letters* **13**, 1983–1990 (2013). URL http://pubs.acs.org/doi/abs/10.1021/nl304777e. [cited at p. 16]

[70] Jeong, J. *et al.* Suppression of metal-insulator transition in VO_2 by electric field-induced oxygen vacancy formation. *Science* **339**, 1402–1405 (2013). [cited at p. 16]

[71] Topinka, M. A. *et al.* Coherent branched flow in a two-dimensional electron gas. *Nature* **410**, 183–186 (2001). URL http://dx.doi.org/10.1038/35065553. [cited at p. 16]

[72] Berezovsky, J., Borunda, M. F., Heller, E. J. & Westervelt, R. M. Imaging coherent transport in graphene (part i): mapping universal conductance fluctuations. *Nanotechnology* **21**, 274013 (2010). URL http://stacks.iop.org/0957-4484/21/i=27/a=274013. [cited at p. 16]

[73] Connolly, M. R. *et al.* Scanning gate microscopy of current-annealed single layer graphene. *Applied Physics Letters* **96**, 113501 (2010). URL http://link.aip.org/link/?APL/96/113501/1. [cited at p. 16]

[74] Jalilian, R. *et al.* Scanning gate microscopy on graphene: charge inhomogeneity and extrinsic doping. *Nanotechnology* **22**, 295705 (2011). URL http://stacks.iop.org/0957-4484/22/i=29/a=295705. [cited at p. 16]

[75] Garcia, A. G. F., König, M., Goldhaber-Gordon, D. & Todd, K. Scanning gate microscopy of localized states in wide graphene constrictions. *Phys. Rev. B* **87**, 085446 (2013). URL http://link.aps.org/doi/10.1103/PhysRevB.87.085446. [cited at p. 16]

[76] Woodside, M. T. & McEuen, P. L. Scanned probe imaging of single-electron charge states in nanotube quantum dots. *Science* **296**, 1098–1101 (2002). [cited at p. 16]

[77] Bleszynski, A. C. *et al.* Scanned probe imaging of quantum dots inside InAs nanowires. *Nano Letters* **7**, 2559–2562 (2007). URL http://pubs.acs.org/doi/abs/10.1021/nl0621037. [cited at p. 16]

[78] Paradiso, N. *et al.* Imaging backscattering through impurity-induced antidots in quantum Hall constrictions. *Phys. Rev. B* **86**, 085326 (2012). URL http://link.aps.org/doi/10.1103/PhysRevB.86.085326. [cited at p. 16]

[79] Leamy, H. J. Charge collection scanning electron microscopy. *Journal of Applied Physics* **53**, R51–R80 (1982). URL http://link.aip.org/link/?JAP/53/R51/1. [cited at p. 16]

[80] Chen, C. Y. *et al.* Electron beam induced current in InSb-InAs nanowire type-III heterostructures. *Applied Physics Letters* **101**, 063116 (2012). URL http://link.aip.org/link/?APL/101/063116/1. [cited at p. 16]

[81] Lang, D. V. & Henry, C. H. Scanning photocurrent microscopy: a new technique to study inhomogeneously distributed recombination centers in semiconductors. *Solid-State Electronics* **21**, 1519–1524 (1978). [cited at p. 16]

[82] Balasubramanian, K. *et al.* Photoelectronic transport imaging of individual semiconducting carbon nanotubes. *Applied Physics Letters* **84**, 2400–2402 (2004). URL http://link.aip.org/link/?APL/84/2400/1. [cited at p. 16]

[83] Lee, E. J. *et al.* Electronic-band-structure mapping of nanotube transistors by scanning photocurrent microscopy. *Small* **3**, 2038–2042 (2007). URL http://dx.doi.org/10.1002/smll.200700418. [cited at p. 16]

[84] Freitag, M. *et al.* Imaging of the schottky barriers and charge depletion in carbon nanotube transistors. *Nano Letters* **7**, 2037–2042 (2007). URL http://pubs.acs.org/doi/abs/10.1021/nl070900e. http://pubs.acs.org/doi/pdf/10.1021/nl070900e. [cited at p. 16]

[85] Lee, E. J., Balasubramanian, K., Weitz, R. T., Burghard, M. & Kern, K. Contact and edge effects in graphene devices. *Nat Nano* **3**, 486–490 (2008). URL http://dx.doi.org/10.1038/nnano.2008.172. [cited at p. 16]

[86] Koren, E., Rosenwaks, Y., Allen, J. E., Hemesath, E. R. & Lauhon, L. J. Nonuniform doping distribution along silicon nanowires measured by kelvin probe force microscopy and scanning photocurrent microscopy. *Applied Physics Letters* **95**, 092105 (2009). URL http://link.aip.org/link/?APL/95/092105/1. [cited at p. 16]

[87] Xia, F. *et al.* Photocurrent imaging and efficient photon detection in a graphene transistor. *Nano Letters* **9**, 1039–1044 (2009). URL http://pubs.acs.org/doi/abs/10.1021/nl8033812. http://pubs.acs.org/doi/pdf/10.1021/nl8033812. [cited at p. 16]

[88] Park, J., Ahn, Y. H. & Ruiz-Vargas, C. Imaging of photocurrent generation and collection in single-layer graphene. *Nano Letters* **9**, 1742–1746 (2009). URL http://pubs.acs.org/doi/abs/10.1021/nl8029493. PMID: 19326919, http://pubs.acs.org/doi/pdf/10.1021/nl8029493. [cited at p. 16]

[89] Gabor, N. M., Zhong, Z., Bosnick, K., Park, J. & McEuen, P. L. Extremely efficient multiple electron-hole pair generation in carbon nanotube photodiodes. *Science* **325**, 1367–1371 (2009). URL http://www.sciencemag.org/content/325/5946/1367.abstract. http://www.sciencemag.org/content/325/5946/1367.full.pdf. [cited at p. 16, 17]

[90] Peters, E. C., Lee, E. J. H., Burghard, M. & Kern, K. Gate dependent photocurrents at a graphene p-n junction. *Applied Physics Letters* **97**, 193102 (2010). URL http://link.aip.org/link/?APL/97/193102/1. [cited at p. 16]

[91] Dufaux, T., Boettcher, J., Burghard, M. & Kern, K. Photocurrent distribution in graphene-CdS nanowire devices. *Small* **6**, 1868–1872 (2010). URL http://dx.doi.org/10.1002/smll.201000950. [cited at p. 16]

[92] Gabor, N. M. *et al.* Hot carrierassisted intrinsic photoresponse in graphene. *Science* **334**, 648–652 (2011). [cited at p. 16, 17]

[93] Sun, D. *et al.* Ultrafast hot-carrier-dominated photocurrent in graphene. *Nature Nano.* **7**, 114–118 (2012). URL http://dx.doi.org/10.1038/NNANO.2011.243. [cited at p. 16]

[94] Bistritzer, R. & MacDonald, A. H. Electronic cooling in graphene. *Phys. Rev. Lett.* **102**, 206410 (2009). URL http://link.aps.org/doi/10.1103/PhysRevLett.102.206410. [cited at p. 17]

[95] Song, J. C. W., Rudner, M. S., Marcus, C. M. & Levitov, L. S. Hot carrier transport and photocurrent response in graphene. *Nano Letters* **11**, 4688–4692 (2011). URL http://pubs.acs.org/doi/abs/10.1021/nl202318u. http://pubs.acs.org/doi/pdf/10.1021/nl202318u. [cited at p. 17]

[96] Cavalleri, A., Rini, M. & Schoenlein, R. Ultra-broadband femtosecond measurements of the photo-induced phase transition in VO_2: From the mid-ir to the hard x-rays. *Journal of the Physical Society of Japan* **75**, 011004 (2006). [cited at p. 18]

[97] Rini, M. *et al.* Optical switching in VO_2 films by below-gap excitation. *Applied Physics Letters* **92**, 181904 (2008). URL http://link.aip.org/link/?APL/92/181904/1. [cited at p. 18]

[98] Graham, R., Miller, C., Triplett, M. & Yu, D. Scanning photocurrent microscopy in single nanowire devices. *Proc. SPIE* **8106**, 81060–81061 (2011). [cited at p. 28]

[99] Miller, M., C.and Triplett *et al.* Unusually long free carrier lifetime and metalinsulator band offset in vanadium dioxide. *Phys. Rev. B* **85**, 085111 (2012). [cited at p. 28]

[100] Wu, J. *et al.* Strain-induced self organization of metal-insulator domains in single-crystalline VO_2 nanobeams. *Nano Letters* **6**, 2313–2317 (2006). URL http://pubs.acs.org/doi/abs/10.1021/nl061831r. PMID: 17034103. [cited at p. 30, 77]

[101] Cao, J. *et al.* Extended mapping and exploration of the vanadium dioxide stress-temperature phase diagram. *Nano Letters* **10**, 2667–2673 (2010). URL http://pubs.acs.org/doi/abs/10.1021/nl101457k. http://pubs.acs.org/doi/pdf/10.1021/nl101457k. [cited at p. 36, 39]

[102] Kucharczyk, D. & Niklewski, T. Accurate x-ray determination of the lattice parameters and the thermal expansion coefficients of VO_2 near the transition temperature. *Journal of Applied Crystallography* **12**, 370–373 (1979). URL http://dx.doi.org/10.1107/S0021889879012711. [cited at p. 39, 44]

[103] Guo, H. *et al.* Mechanics and dynamics of the strain-induced m1m2 structural phase transition in individual VO_2 nanowires. *Nano Letters* **11**, 3207–3213 (2011). URL http://pubs.acs.org/doi/abs/10.1021/nl201460v. http://pubs.acs.org/doi/pdf/10.1021/nl201460v. [cited at p. 43]

[104] Yun, W. S., Han, S. W., Hong, S. C., Kim, I. G. & Lee, J. D. Thickness and strain effects on electronic structures of transition metal dichalcogenides: 2H-MX_2 semiconductors (M = Mo, W; X = S, Se, Te). *Phys. Rev. B* **85**, 033305 (2012). URL http://link.aps.org/doi/10.1103/PhysRevB.85.033305. [cited at p. 46]

[105] He, K., Poole, C., Mak, K. F. & Shan, J. Experimental demonstration of continuous electronic structure tuning via strain in atomically thin MoS_2. *Nano Letters* **13**, 2931–2936 (2013). URL http://pubs.acs.org/doi/abs/10.1021/nl4013166. http://pubs.acs.org/doi/pdf/10.1021/nl4013166. [cited at p. 46]

[106] Tang, C. *et al.* Local atomic and electronic arrangements in $W_xV_{1-x}O_2$. *Phys. Rev. B* **31**, 1000–1011 (1985). URL http://link.aps.org/doi/10.1103/PhysRevB.31.1000. [cited at p. 49]

[107] Chippindale, A., Dickens, P. & Powell, A. Synthesis, characterization, and inelastic neutron scattering study of hydrogen insertion compounds of VO_2(rutile). *Journal of Solid State Chemistry* **93**, 526 – 533 (1991). URL http://www.sciencedirect.com/science/article/pii/002245969190327E. [cited at p. 50, 51, 52]

[108] Steele, B. C. H. & Heinzel, A. Materials for fuel-cell technologies. *Nature* **414**, 345–352 (2001). [cited at p. 50]

[109] Dresselhaus, M. & Thomas, I. L. Alternative energy technologies. *Nature* **414**, 332–337 (2001). [cited at p. 50]

[110] Schlapbach, L. & Zttel, A. Hydrogen-storage materials for mobile applications. *Nature* **414**, 353–358 (2001). [cited at p. 50]

[111] Fukuzumi, S. Bioinspired energy conversion systems for hydrogen production and storage. *Eur. J. Inorg. Chem.* 1351–1362 (2008). [cited at p. 50]

[112] Pankove, J. I., Carlson, D. E., Berkeyheiser, J. E. & Wance, R. O. Neutralization of shallow acceptor levels in silicon by atomic hydrogen. *Phys. Rev. Lett.* **51**, 2224–2225 (1983). URL http://link.aps.org/doi/10.1103/PhysRevLett.51.2224. [cited at p. 50]

[113] Van de Walle, C. G., Denteneer, P. J. H., Bar-Yam, Y. & Pantelides, S. T. Theory of hydrogen diffusion and reactions in crystalline silicon. *Phys. Rev. B* **39**, 10791–10808 (1989). URL http://link.aps.org/doi/10.1103/PhysRevB.39.10791. [cited at p. 50]

[114] Mollwo, E. Die wirkung von wasserstoff auf die leitfhigkeit und lumineszenz von zinkoxydkristallen. *Zeitschrift fr Physik* **138**, 478–488 (1954). URL http://dx.doi.org/10.1007/BF01340694. [cited at p. 50]

[115] Wager, J. F. Transparent electronics. *Science* **300**, 1245–1246 (2003). URL http://www.sciencemag.org/content/300/5623/1245.short. http://www.sciencemag.org/content/300/5623/1245.full.pdf. [cited at p. 50]

[116] Thomas, D. G. & Lander, J. J. Hydrogen as a donor in zinc oxide. *The Journal of Chemical Physics* **25**, 1136–1142 (1956). URL http://scitation.aip.org/content/aip/journal/jcp/25/6/10.1063/1.1743165. [cited at p. 50]

[117] Van de Walle, C. G. Hydrogen as a cause of doping in zinc oxide. *Phys. Rev. Lett.* **85**, 1012–1015 (2000). URL http://link.aps.org/doi/10.1103/PhysRevLett.85.1012. [cited at p. 51]

[118] Bates, J. B. & Perkins, R. A. Infrared spectral properties of hydrogen, deuterium, and tritium in TiO_2. *Phys. Rev. B* **16**, 3713–3722 (1977). URL http://link.aps.org/doi/10.1103/PhysRevB.16.3713. [cited at p. 51]

[119] Cathcart, J. V., Perkins, R. A., Bates, J. B. & Manley, L. C. Tritium diffusion in rutile TiO_2. *Journal of Applied Physics* **50**, 4110–4119 (1979). URL http://scitation.aip.org/content/aip/journal/jap/50/6/10.1063/1.326490. [cited at p. 51]

[120] Chen, W. P., Wang, Y. & Chan, H. L. W. Hydrogen: A metastable donor in TiO_2 single crystals. *Applied Physics Letters* **92**, – (2008). URL http://scitation.aip.org/content/aip/journal/apl/92/11/10.1063/1.2900957. [cited at p. 51]

[121] Johnson, O. W., Paek, S. & DeFord, J. W. Diffusion of h and d in VO_2: Suppression of internal fields by isotope exchange. *Journal of Applied Physics* **46**, 1026–1033 (1975). URL http://scitation.aip.org/content/aip/journal/jap/46/3/10.1063/1.322206. [cited at p. 54]

[122] Strelcov, E., Davydov, A. V., Lanke, U., Watts, C. & Kolmakov, A. In situ monitoring of the growth, intermediate phase transformations and templating of single crystal VO_2 nanowires and nanoplatelets. *ACS Nano* **5**, 3373–3384 (2011). URL http://pubs.acs.org/doi/abs/10.1021/nn2007089. http://pubs.acs.org/doi/pdf/10.1021/nn2007089. [cited at p. viii, 69, 70, 71]

[123] Varghese, B., Tamang, R., Tok, E.-S., Mhaisalkar, S. G. & Sow, C. H. Photothermoelectric effects in localized photocurrent of individual VO_2 nanowires. *The Journal of Physical Chemistry C* **114**, 15149–15156 (2010). URL http://pubs.acs.org/doi/abs/10.1021/jp1051936. http://pubs.acs.org/doi/pdf/10.1021/jp1051936. [cited at p. 69]

[124] Kosuge, K. The phase diagram and phase transition of the V_2O_3-V_2O_5 system. *Journal of Physics and Chemistry of Solids* **28**, 1613 – 1621 (1967). URL http://www.sciencedirect.com/science/article/pii/0022369767902934. [cited at p. viii, 71]

[125] Wriedt, H. The O-V (Oxygen-Vanadium) system. *Journal of Phase Equilibria* **10**, 271–277 (1989). URL http://dx.doi.org/10.1007/BF02877512. 10.1007/BF02877512. [cited at p. viii, 71]